UNDERSTANDING OF THE TRICARBOXYLIC ACID CYCLE METABOLON AS AN EFFICIENT BIOCATALYST

by

Fei Wu

A dissertation submitted to the faculty of
The University of Utah
in partial fulfillment of the requirements for the degree of

Doctor of Philosophy

Department of Chemistry

The University of Utah

August 2015

Copyright © Fei Wu 2015

All Rights Reserved

The University of Utah Graduate School

STATEMENT OF DISSERTATION APPROVAL

The dissertation of **Fei Wu**

has been approved by the following supervisory committee members:

Shelley D. Minteer	, Chair	**June 1, 2015** Date Approved
Henry S. White	, Member	**June 1, 2015** Date Approved
Joel M. Harris	, Member	**June 1, 2015** Date Approved
Haitao Ji	, Member	**June 2, 2015** Date Approved
Ling Zang	, Member	**June 2, 2015** Date Approved

and by **Cynthia J. Burrows**, Chair/Dean of

the Department/College/School of **Chemistry**

and by David B. Kieda, Dean of The Graduate School.

ABSTRACT

In mitochondria, the tricarboxylic acid (TCA) cycle integrates oxidation pathways of all major carbon sources by eight enzymes that are associated into a supramolecular complex called the metabolon. In metabolons, substrate channeling is the most remarkable feature, which is the directed or facilitated intermediate transport between active sites. Considerable studies have been done on biological implications of substrate channeling in improving coupled catalysis. Nowadays the TCA cycle metabolon attracts increasing interest from experts in the field of bioelectrocatalysis, who have been seeking highly efficient enzyme cascades enabling deep substrate oxidation and promoted mass transport. This dissertation research focuses on the fundamental understanding of the TCA cycle metabolon from mechanistic and structural perspectives.

In this work, a microfluidic system was built to study enzyme dynamics in metabolon formation and showed that intermediate generated by one enzyme induces directed transport of subsequent enzymes against the concentration gradient, and thus enhances enzyme association. Structural probing by *in vivo* cross-linking, mass spectrometry and protein docking revealed protein-protein interactions in the natural TCA cycle metabolon. Computer simulation demonstrated the formation of an electrostatic channeling upon association-induced surface charge rearrangement.

The other aspect of this dissertation is *in vitro* fabrication of the TCA cycle metabolon mimics by two strategies. Polymeric co-immobilization-induced multi-enzyme

aggregation was assessed by acceptor photobleaching FRET imaging. Structure-based design of engineered metabolons was also exploited to construct a recombinant complex featuring natural orientation and enhanced substrate channeling.

This dissertation work is gratefully dedicated to my beloved parents,
Ping Song and Jian Wu,
without whose unconditional love, support and encouragement,
none of this would be possible.
Special thanks to all my dear friends and those who strive for ideals.

TABLE OF CONTENTS

LIST OF TABLES

LIST OF FIGURES

ACKNOWLEDGEMENTS

I would like to express my endless gratitude to my supervisor and committee chair, Dr. Shelley D. Minteer, for her excellent guidance on my research and writing, patience with my mistakes, enthusiasm for teaching me, and her rigorous attitude toward science that added to my valuable graduate experiences. I could not have imagined finishing my Ph.D. dissertation without her continuous support and mentoring. I am sincerely grateful to my committee members, Dr. Henry S. White, Dr. Joel M. Harris, Dr. Haitao Ji, Dr. Ling Zang and former member, Dr. Jennifer S. Shumaker-Parry, for their helpful comments and advice. I also give my appreciation to my colleagues and collaborators for their contributions to this dissertation work: Lindsey N. Pelster for making the PDMS mold, Beyza Bulutoglu and Kristen E. Garcia from Dr. Scott A. Banta's group at Columbia University for synthesis and purification of recombinant enzymes and site-directed mutagenesis, Dr. Krishna Parsawar at Mass Spectrometry and Proteomics Core Facility for in gel digestion, mass spectrometry instrumentation and *Mascot* search, and Dr. Michelle Rasmussen and Dr. Ross D. Milton for proof reading of this thesis. The last but not the least, I am deeply indebted to my family and my best friends for their constant love, encouragement and faith in me.

CHAPTER 1

INTRODUCTION

1.1 Overview of the Tricarboxylic Acid Cycle

The tricarboxylic acid cycle (TCA cycle), also named the citric acid cycle or the Krebs cycle, is the central pathway integrating the carbon flows originated from all main classes of biomolecules and energy conversion in conjunction with oxidative phosphorylation.[1] It was first postulated by Krebs in 1937. Combining β–oxidation of fatty acids, oxidative deamination of amino acids, decarboxylation of α–ketonic acids and rearrangement of citrate to succinate, Krebs put forward a scheme of the TCA cycle for carbohydrate degradation to carbon dioxide. Although Krebs' hypothesis received severe criticism back then, numerous supporting results, such as discoveries of acetyl coenzyme A (CoA) as well as fatty acids and ketones as crucial carbon sources for citrate formation, finally led the majority to accept the TCA cycle as the common end point of oxidation pathways of most carbohydrates, fatty acids and amino acids. Along with technical advancement in biochemistry, extensive work has been conducted toward the enzymes and metabolic roles of the TCA cycle, which is widely accepted as one of the most astonishing achievements in the realm of metabolism research.[2,3]

1.1.1 Enzymatic Reactions of the TCA Cycle

Aerobically, most biomolecules (i.e. pyruvate and fatty acids) enter the TCA cycle as acetyl-CoA and are sequentially broken down into CO_2 through eight steps (Figure 1.1). The first step, also the most essential step, is the condensation of oxaloacetate (OAA) and aceyl-CoA to citrate, generating CoA as well. This reaction is catalyzed by citrate synthase (CS), which is a homodimer (98 kDa) containing two identical active sites for OAA and binding sites for acetyl-CoA. During the catalytic cycle, the reaction occurs in an ordered manner; that is, OAA binds to CS first to result in a 20-fold increase in binding constant for acetyl-CoA. As a key rate-limiting enzyme, CS maintains the cyclic flux by catalyzing the only C-C formation in the TCA cycle.[4]

$$C_2H_3OSCoA + C_4H_4O_5 + H_2O \xrightarrow{CS} CoASH + C_6H_8O_7$$

Via cis-aconitate, citrate is isomerized to isocitrate by a stereospecific dehydration-rehydration process at the active site of a monomeric enzyme called aconitase (ACO, 83 kDa). Being an iron-sulfur protein, ACO can be activated by incorporating another iron (II) to turn inactive [3Fe-4S] to active [4Fe-4S], which is then complexed with citrate. Substantial proton extraction from carboxyl group of citrate results in formation of a Cα-Cβ double bond in cis-aconitate. To proceed towards isocitrate, cis-aconitate is rotated by 180° around the double bond and rehydrated by the previously abstracted proton.[5]

$$C_6H_8O_7(\text{citrate}) \xrightleftharpoons{ACO} C_6H_8O_7(\text{isocitrate})$$

The first NAD(H)-dependent oxidoreductase in the TCA cycle, isocitrate dehydrogenase (ICDH), catalyzes the oxidative decarboxylation of isocitrate to α-ketoglutarate and CO_2 through a phosphorylation and dephosphorylation cycle of the

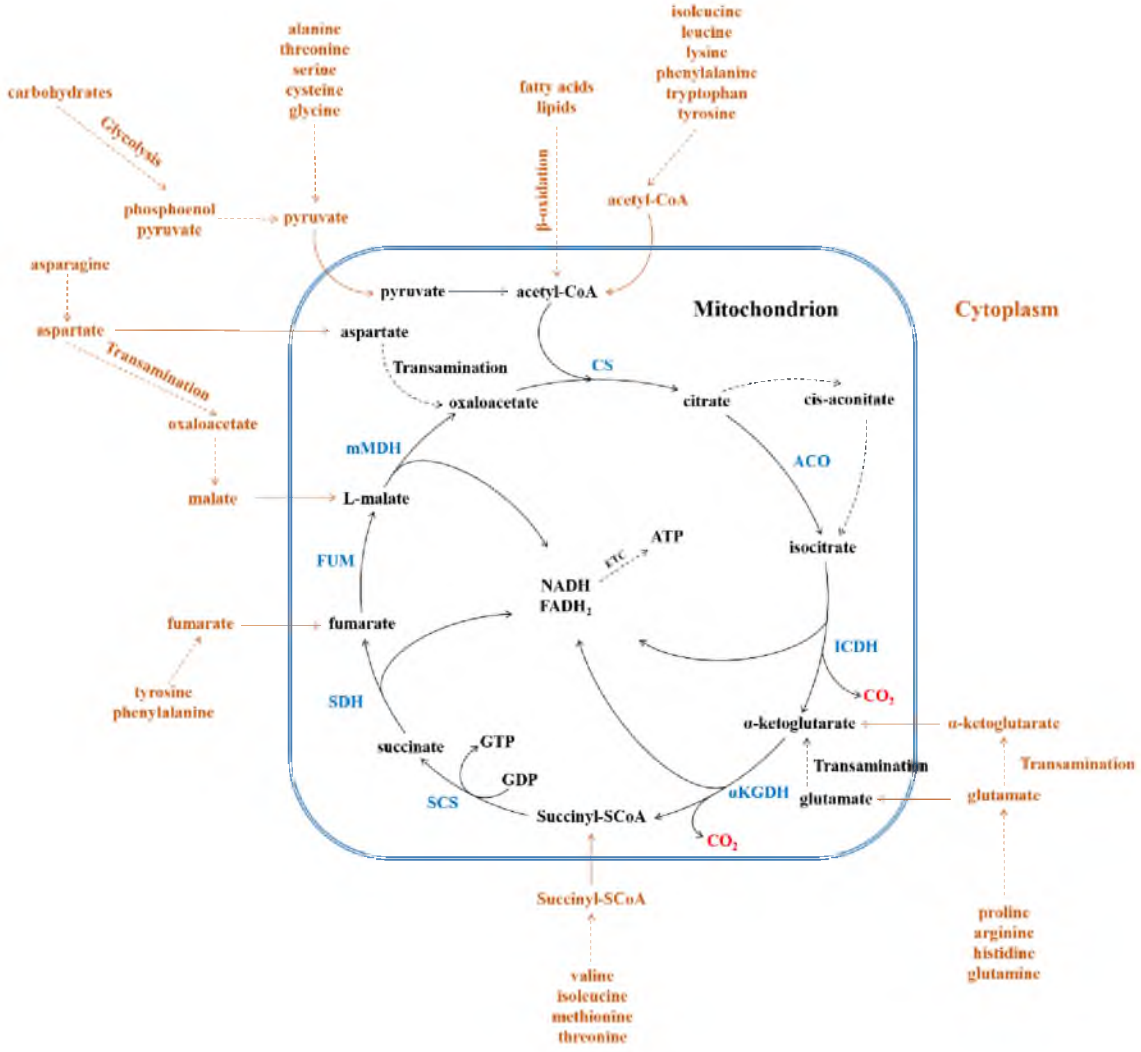

Figure 1.1 Metabolic role of the TCA cycle in anaerobic degradation (oxidation).[1]

enzyme.[1,6]

$$C_6H_8O_7(\text{isocitrate}) + NAD^+ \xrightarrow[Mg^{2+}]{ICDH} C_5H_6O_5 + NADH + CO_2$$

The following α-ketoglutarate dehydrogenase (αKGDH) is a gigantic multienzyme complex consisting of three different enzymes, 2-oxoglutarate decarboxylase (E1k), dihydrolipoamide succinyltransferase (E2k) and dihydrolipoamide dehydrogenase. Similar to ICDH, the αKGDH complex catalyzes the second oxidative decarboxylation of α-ketoglutarate to succinyl-CoA, accompanied by CO_2 generation and NAD^+ reduction.[7]

$$C_5H_6O_5 + NAD^+ + CoASH \xrightarrow[\substack{ThPP,\ LpS_2,\\ FAD,\ Mg^{2+}}]{\alpha KGDH} C_4H_5O_3SCoA + NADH + CO_2$$

The next enzyme, succinyl-CoA synthetase (SCS), or succinyl thiokinase, contains two subunits, α (33.5 kDa) and β (46.5 kDa). It catalyzes the reversible hydrolysis of succinyl-CoA to succinate and CoA, and the substrate-level phosphorylation of GDP or ADP by phosphate. It is the only step in the cycle that directly produces metabolic energy, GTP or ATP, depending on the isoforms of SCS and concentration ratios of nucleotide diphosphate to nucleotide triphosphate in mitochondria.[8,9]

$$C_4H_5O_3SCoA + G(A)DP + Pi \xrightleftharpoons{SCS} C_4H_6O_4 + CoASH + G(A)TP$$

Unlike other soluble TCA cycle enzymes in the matrix, succinate dehydrogenase (SDH) is a membrane bound enzyme as Complex II of the respiratory electron transport chain (ETC) in the inner mitochondrial membrane.[10] At the FAD-containing center of SDH, protons are extracted from succinate to form fumarate. Electrons are transferred from $FADH_2$ to the final carrier ubiquinone. Fumarate is then catalytically rehydrated by fumarase (FUM) to L-malate for the final step of the cycle.[11]

$$C_4H_6O_4 + FAD \rightleftharpoons C_4H_4O_4 + FADH_2$$

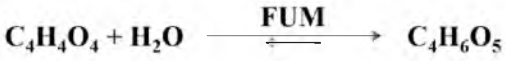

$$C_4H_4O_4 + H_2O \rightleftharpoons C_4H_6O_5$$

The last NAD-dependent oxidoreductase, malate dehydrogenase (MDH) catalyzes the final oxidation (dehydrogenation) of L-malate reversibly back to oxaloacetate (OAA). MDH is also a homodimer (70 kDa) and highly stereospecific to L-malate. D-malate can occupy the MDH active site, but will not be converted, thus working as an inhibitor of MDH. It is worth mentioning that MDH has two structural forms: mitochondrial form (mMDH) and cytoplasmic form (cMDH). The two forms play a very important part in the ATP production chain. Since NADH cannot directly pass through the mitochondrial membrane from the cytoplasm, cMDH catalyzes its oxidation to NAD^+ with reduction of OAA to L-malate, which is shuttled through the membrane into the mitochondrial matrix.[12] There mMDH catalyzes the reverse reaction, and regenerated NADH is thus used to pump up the ETC for ATP production.

$$C_4H_6O_5 + NAD^+ \rightleftharpoons C_4H_4O_5 + NADH$$

1.1.2 Metabolic Roles of the TCA Cycle

The TCA cycle occupies the central hub in the energy supply for cellular activities by connecting glycolysis in the mitochondrial matrix and ETC in the inner membrane of mitochondria. As the major carbon and energy sources for most organisms, hexoses are degraded by the glycolysis pathway to pyruvate, which is subsequently converted to acetyl-CoA under the catalysis of pyruvate dehydrogenase complex (PDH complex), or to OAA under the catalysis of pyruvate carboxylase. Both of the products are utilized by CS in the

first step of the TCA cycle and finally completely oxidized to CO_2. Meanwhile, NADH is produced for the ETC to pump a proton gradient across the mitochondrial membrane, and ultimately power ATP synthetase. For each unit of hexose, such as glucose, a total of 38 ATP and 6 CO_2 molecules are generated from glycolysis, the PDH complex, the TCA cycle and the ETC.

Besides carbohydrates, fatty acids and amino acids can also be converted into metabolic energy by aerobic oxidation. From one unit of fatty acids, such as stearic acid, 9 acetyl-CoA molecules enter the TCA cycle after β-oxidation, followed by complete oxidation to 18 CO_2 molecules and generation of 108 ATP in total together with the ETC. In the case of using amino acids as energy sources, the situation is more complex as there are several different entrances to the TCA cycle based on the types of amino acids involved. For most common amino acids, acetyl-CoA remains the linkage between transamination and CS-catalyzed decarboxylation. However, for proline, arginine, histidine and glutamine, they are primarily transferred to glutamate, which is oxidized by glutamate dehydrogenase to α-ketoglutarate, and taken up by the αKGDH complex. For valine, isoleucine, methionine and threonine, they are converted to succinyl-CoA for SCS. For tyrosine and phenyalanine, they are converted to fumarate for FUM, while asparagine enters the TCA cycle through a series of transformations catalyzed by aspartate aminotransferase (AAT) and MDH.

When pushing ATP production from biofuels, the TCA cycle runs its second role in the synthesis of a variety of biomaterials, at the expense of ATP. For example, most of the amino acids (precursors for protein synthesis) can be regenerated from intermediates (isocitrate, α-ketoglutarate, succinyl-CoA, L-malate and oxaloacetate) of the TCA cycle.

Similar schemes can be drawn for biosynthesis of lipids and carbohydrates; however, this will not be discussed in details as the dissertation focuses on the catabolic role of the TCA cycle in complete oxidation and energy production.[1,13,14]

1.1.3 Regulation of the TCA Cycle

ATP production and consumption in the TCA cycle for metabolic needs are primarily regulated by the ratio of $NADH/NAD^+$ in mitochondria. In general, high $NADH/NAD^+$ leads to phosphorylation of AMP and ADP to produce more ATP, while low $NADH/NAD^+$ initiates ATP hydrolysis in demand of energy. Within the cycle, CS-catalyzed acetyl-CoA-OAA condensation and ICDH-catalyzed isocitrate decarboxylation are two major regulatory sites. Both ATP and NADH at high concentration levels will place negative effects on the activity of CS and ICDH, decreasing the overall oxidation rate. Accumulation of ADP/AMP and NAD^+ after a burst of energy utilization will activate ICDH to speed up ATP production. It is worth noting that the situation for ICDH is more complex, since its function is linked to another bifunctional protein kinase/phosphatase, and a set of metabolites have been identified as effectors on the ICDH phosphorylation cycle.[6,15] Other dehydrogenases are also subject to $NADH/NAD^+$ regulation with various sensitivities. In addition, the TCA cycle flux is closely associated with substrate supplies from auxiliary enzymes in glycolysis, fatty acid oxidation and transamination. Pools of intermediates/products generated in each step are very important in coordinating the cycle flux, which is known as the feedback mechanism. As an example, citrate is a competitive inhibitor for CS as well as for mMDH.[13,14,16,17]

1.2 Metabolic Enzymes as Biocatalysts in Enzymatic Biofuel Cells

1.2.1 Kinetics of Enzymes as Biocatalysts

Enzyme kinetics study time-dependent enzyme-catalyzed reactions approaching the equilibrium state. In a simple second-order model as below

$$S + E \underset{k_{-1}}{\overset{k_1}{\rightleftharpoons}} ES \xrightarrow{k_2} E + P$$

Substrate (S) reversibly binds to enzyme (E) to form a transition enzyme-substrate complex (ES). ES then proceeds to the formation of product (P) and recovery of E.

Rate of product formation is described by turnover rate v, which is directly dependent on concentration of ES as below

$$\frac{d[P]}{dt} = k_2[ES] = v$$

[ES] is determined by

$$\frac{d[S]}{dt} = -k_1[S][E] + k_{-1}[ES]$$

$$\frac{d[E]}{dt} = -k_1[S][E] + (k_{-1}+k_2)[ES]$$

$$\frac{d[ES]}{dt} = -k_1[S][E] - (k_{-1}+k_2)[ES]$$

During the course of time-dependent changes of S or P illustrated in Figure 1.2, there are three phases: a short initial or pre-steady-state phase where ES is formed and v is low, a steady-state phase where [ES] is almost constant and v reaches its maximal, and a substrate depletion phase where [ES] decays with S exhausted and v decreasing to nearly zero. The lengths of the three phases are dependent on k_1, k_{-1} and k_2. Based on the assumption that the steady-state phase is relatively longer than the other two phases ($k_1 \approx k_{-1} > k_2$), the reaction can be regarded as in quasi equilibrium state for a limited period when

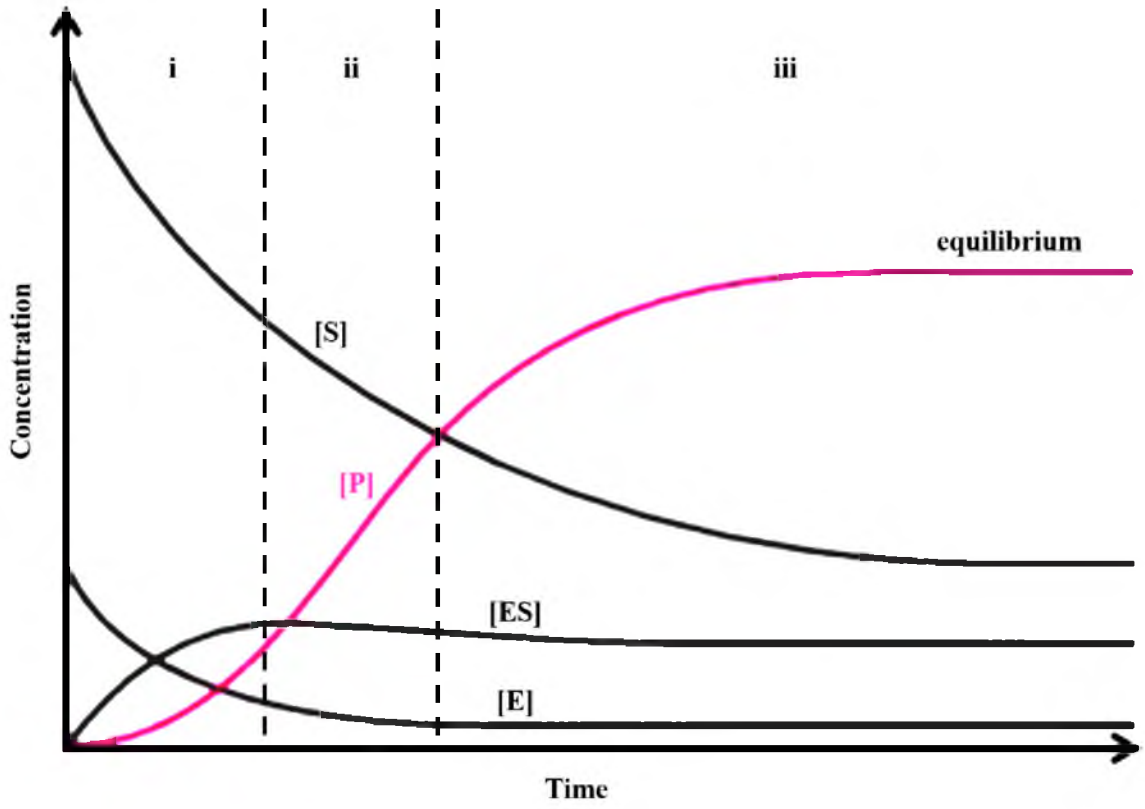

Figure 1.2 Time-dependent changes of substrate ([S]), product ([P]), free enzyme ([E]) and bound enzyme ([ES]): (i) pre-steady-state phase, (ii) steady-state phase, (iii) substrate-depletion phase.[18]

[S] and [P] change linearly to keep [ES] constant. Therefore, it is reasonable to say

$$k_1[S][E] = (k_{-1} + k_2)[ES]$$

Since $[E]_o = [E] + [ES]$, then

$$[ES] = \frac{k_1[E]_o[S]}{k_1[S]+k_{-1}+k_2}$$

and

$$v = k_2[ES] = \frac{k_2[E]_o[S]}{\frac{k_{-1}+k_2}{k_1} + [S]}$$

By defining $K_m = (k_{-1} + k_2)/k_1$ and $V_{max} = k_2[E]_o$, the Michaelis-Menten equation is achieved as below

$$v = \frac{V_{max}[S]}{K_m + [S]}$$

According to the Michaelis-Menten kinetic theory, $[E]_o$ does not change considerably during the reaction and all enzyme molecules are accessible for substrate binding to achieve the highest possible turnover. It is assumed that the system reaches the equilibrium between free enzymes and bound enzymes much faster than the catalytic reaction, so the Michaelis constant K_m is directly associated to the dissociation constant for substrate and enzyme, and indicates the affinity of a specific substrate to the enzyme (the lower K_m, the higher affinity):

$$K_m = K_d = k_{-1}/ k_1$$

V_{max} and $k_{cat} = V_{max}/[E]_o$ refer to the maximum turnover rate and the turnover number (or catalytic constant), respectively. Finally, the catalytic efficiency is defined as the ratio k_{cat}/K_m.[19]

1.2.2 Enzymatic Biofuel Cell

Enzymatic biofuel cells (BFCs) are fuel cells employing enzymes to catalyze energy conversion from different substrates/fuels to electricity. As illustrated in Figure 1.3, a typical enzymatic BFC consists of four basic parts: (1) a bioanode where oxidoreductases catalyze oxidation of fuels and extract electrons to the electrode directly or through mediators, (2) a cathode (frequently biocathode) where the oxidant (i.e. O_2) is catalytically reduced to accomplish electrical work, (3) an external circuit to transport electrons from anode to cathode, and (4) electrolyte to support ion movement between electrodes. Compared to conventional fuel cells, enzymatic BFCs do not require toxic or costly fabrication. By utilizing renewable fuel sources, they are capable of producing sustainable energy and functioning at mild conditions. Therefore, enzymatic BFCs give a promising future in micro-power sources (i.e. blood glucose sensors, pacemakers, blood pressure or hormone monitors) fueled by biomass or *in vivo* body fluid.[20-22]

1.2.3 Metabolic Enzyme Cascades in Enzymatic Biofuel Cells

Because of the high substrate selectivity of single enzymes, enzyme cascades are now under frequent investigation to catalyze deep oxidation of high energy density fuels (alcohols, glycerol, etc.). To improve the coulombic efficiency of a glucose BFC, Tasca *et al.* developed a bioanode with combined pyranose and cellobiose dehydrogenases to extract up to six electrons from one glucose molecule, compared to traditional glucose BFCs yielding only two electrons per glucose molecule.[23] Lang *et al.* designed an enzymatic BFC capable of producing a maximum power density at 8 $\mu W/cm^2$ out of starch by co-immobilizing glucoamylase and glucose oxidase on a bioanode.[24] Palmore *et al.* fabricated a methanol/O_2 BFC to achieve the complete breakdown of methanol to CO_2

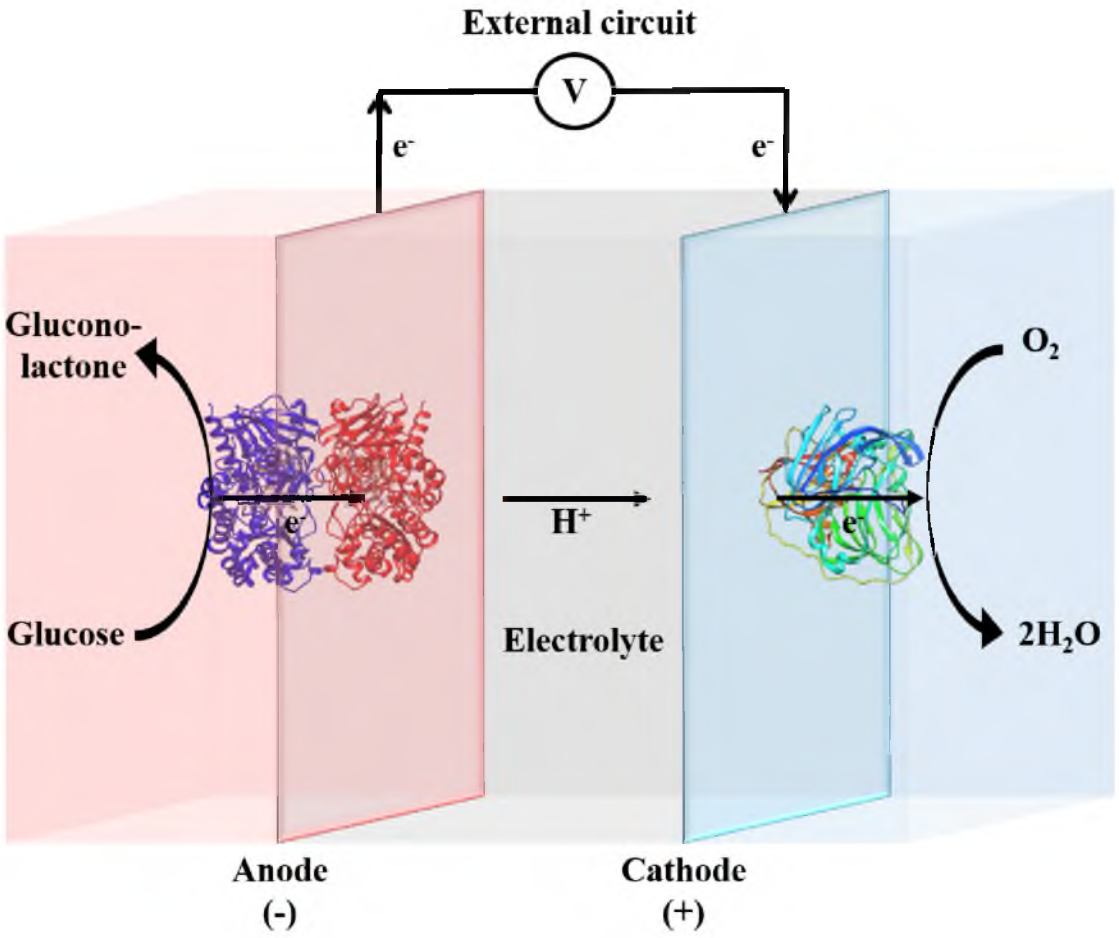

Figure 1.3 Schematic of an enzymatic glucose BFC. Glucose oxidase (PDB ID: 1GPE) catalyzes oxidation of glucose to gluconolactone at the anode and laccase (PDB ID: 2XU9) catalyzes oxidation of O_2 to H_2O at the cathode.

through an enzyme cascade consisting of NAD^+-dependent alcohol, aldehyde and formate dehydrogenases together with diapharose as the electrocatalyst for NADH oxidation. Neto *et al.* used a two-enzyme cascade of PQQ-dependent alcohol and aldehyde dehydrogenases to oxidize ethanol to acetate through direct electron transfer (higher electrode coupling efficiency than mediated electron transfer when NAD^+-dependent dehydrogenases are used) to the anode.[25] Arechederra *et al.* developed a three-enzyme cascade combining PQQ-dependent alcohol dehydrogenase, PQQ-dependent aldehyde dehydrogenase and an additional oxalate oxidase to completely oxidize glycerol.[26,27] Furthermore, Xu *et al.* designed a six-enzyme cascade immobilized bioanode to sequentially oxidize glucose to CO_2 in an artificial, minimal metabolic pathway.[28]

1.2.4 Application of the TCA Cycle in Enzymatic Biofuel Cells

Due to its central place in the network of metabolism of sugars, lipids and amino acids, the TCA cycle has been extensively studied to understand mitochondrion-related signaling pathways, metabolic disorders and tumorigenesis under physiological and pathological conditions.[2] In recent years, researchers came to recognize its potential application in enzymatic BFCs.[29] Sokic-Lazic *et al.* reconstituted the TCA cycle from commercially purified enzymes and coupled it to lactate dehydrogenase or pyruvate dehydrogenase to oxidize lactate or pyruvate. This proved to be dramatically more efficient than single enzyme BFCs as both current and power densities were increased by at least 20 folds .[30,31] Fukuda *et al.* incorporated the TCA cycle into a microenzymatic electrolysis cell and electrochemically characterized the metabolic regulation on an electrode. Their fundamental study further confirmed the capability of TCA-cycle-based systems for harnessing electric energy out of organic acids.[32] Reconstruction of the coupled cycle *in*

vitro will definitely expand its application in the new-generation devices powered by a wide range of fuels.

1.3 Metabolon and Substrate Channeling Formation

Bringing multiple enzymes together also raises new challenges. Mass transport issue remains one of the main hurdles that limit the performance of enzymatic BFCs. For a two-enzyme-cascade-modified bioanode which extracts *n* electrons at the second enzyme, current (i) is in direct proportion to turnover rates of the two reactions (k_{cat1} and k_{cat2}) and inverse proportion to time (t) for intermediate diffusing.[33]

$$i \propto \frac{n}{\frac{1}{k_{cat1}} + t + \frac{1}{k_{cat2}}}$$

Normally, intermediates tend to equilibrate with the bulk solution before they reach the next active site. Increased diffusion time lowers the coupled energy conversion rate and the current density, but this problem is intelligently solved *in vivo*. Nature has found its way to boost mass transport between enzymes within cells, where the environment is technically harsher for efficient transport of small molecules through highly crowded pathways full of obstacles like polysaccharides, proteins and nucleic acids. Rather than diffusing freely and randomly in the cytoplasm, sequential metabolic enzymes are spatially organized into three-dimensional supramolecular complexes, which were first named metabolons by Paul. A. Srere 30 years ago. This definitely changed people's view of the cell as "a bag of enzymes" in early times, because metabolons were found to exist in almost all metabolic pathways and cells. [34-36]

1.3.1 Metabolon Formation

Metabolons are multienzyme complexes formed through various interactions including covalent linkages, electrostatic forces, hydrophobic interactions, hydrogen bonding and Van der Waals interactions. Based on their robustness, metabolons can be generally classified into static and dynamic complexes.[35,37] Static complexes are tightly associated through stronger interactions and more resistant to environmental alterations. Therefore, they are isolatable. For example, the PDH complex and the αKGDH complex are static complexes. On the contrary, dynamic complexes are held together by much weaker forces. This type of metabolons are usually observed in highly progressive pathways with numerous metabolic crossroads, such as the glycolytic pathway and the TCA cycle. Transient association allows their quick reorganization in response to any external stimuli. In these complexes, intermediates are not always strongly bound as in static complexes but locally accumulated around metabolons to form discrete "pools", which is in fact a wise strategy to overcome limited solvation in cells. It also facilitates the preferential delivery of intermediates for specific products and control of metabolic flux.[35,38,39] Although the mechanism for metabolon formation is not fully understood, it is believed that the unique cellular community supported by structural scaffolds (filament and microtubule) is essential in stabilizing dynamic complexes. In the living cells, proteins are highly concentrated. The aqueous phase is highly viscous as half of water molecules are in the bound state, and 30% of space is occupied by macromolecules. This so-called volume-excluding effect promotes not only protein-protein interactions but also protein-scaffold interactions, resulting in compartmentalization of metabolic pathways.[35,40,41] In the meantime, small metabolites may also place a nonnegligible effect on the stability of these

loosely associated complexes.[42] Therefore, membrane disruption and protein dilution during isolation and purification often lead to instant dissociation of dynamic metabolons.

1.3.2 Isolation of Dynamic Metabolons

Compared to stable multifunctional proteins or multienzyme complexes, dynamic metabolons always require special attention to minimize or overcome adverse effects during isolation. First of all, relatively gentle cell disruption is needed to recover enzyme associations. Second, dilution factors can be compensated by adding in volume-excluding agents like polyethylene glycol (PEG) or accumulating proteins in ammonium sulfate-induced precipitation. Third, metabolic enzymes should be co-fractionated during each isolation step. Finally, protein-protein interactions (not random aggregation) are conserved after isolation.[42] Despite the technical difficulties, a number of metabolons have been isolated from nucleic acid biosynthesis, protein biosynthesis, glycogen biosynthesis, purine and pyrimidine biosynthesis, amino acid metabolism, lipid and steroid biosynthesis, glycolysis, the TCA cycle, fatty acid oxidation, electron transport chain, antibiotic biosynthesis, the urea cycle and cyclic AMP degradation.[38]

1.3.3 Substrate Channeling in Metabolons

The most remarkable feature of metabolons is substrate channeling, which refers to directed or facilitated mass transport between active sites of two functionally connected subunits in a multifunctional protein or a multienzyme complex[38,43]. Based on previous studies, substrate channeling can be realized by two distinct mechanisms: direct transfer through a physical tunnel in the complex or an electrostatically favored highway at the complex surface. The former is more likely found in static metabolons or multifunctional proteins through allosteric interactions between active sites.[43-45] To restrict water molecule

accessibility, physical channels are hydrophobic and embedded inside proteins where intermediates are usually covalently bound to specific residues. During a single turnover, intermediates are transferred quickly and irreversibly to the next active site without accumulation.[46,47] In the latter situation, surface charges are rearranged to form continuous patches linking the active sites. As a result, oppositely charged intermediates are still held close to the surface and guided to desired sites through electrostatic interactions.[48-51] Compared to physical channeling, electrostatic channeling is less efficient in avoiding escape of intermediates into aqueous phase (leaky channeling), but it enables more flexible regulation on metabolic flux in metabolons.

When studying the TCA cycle metabolon in mitochondria permeabilized by toluene, Robinson *et al.* observed a 3-fold acceleration in coupled reaction rate between mMDH and CS, compared to that of equivalent free enzymes[52]. This kinetic improvement was attributed to a combination of several benefits brought by channeling compared to free diffusion of intermediates. (1) Spatial distance between active sites and time for mass transport are both reduced. (2) Loss of intermediates during diffusion is prevented. (3) Kinetic parameters are optimized to improve cascade coupling efficiency. (3) Thermodynamically unfavorable equilibria are circumvented by fast depletion of products. (4) Labile intermediates are protected from reactive species and competing pathways. (5) Transfer of metabolites on metabolon surface is less affected by the crowded bulk environment.[43,44]

1.3.4 Methods of Demonstrating Substrate Channeling

Substrate channeling had been under debate on its actual existence and kinetic significance due to the lack of direct evidence. According to the hypothesis, substrate

channeling is a fast transient process (more than 1000 s^{-1})[46] occurring within a very short distance (probably less than 10 nm).[50] In other words, it is almost impossible to directly monitor channeling of small metabolites (mostly not detectable) *in situ* using traditional steady-state or microscopic methods. By X-ray crystallography, Davies *et al.* showed the first direct physical evidence for an indole tunnel between α– and β-subunits in tryptophan synthase.[43,44,53,54] There is more supporting structural evidence on intermediate tunnels in carbomoyl phosphate synthetase[45], the family of glutamine amidotransferases[55], thymidylate synthase-dihydrofolate reductase[49], αKGDH complex[56] and lumazine synthase/riboflavin synthase complex.[57] However, for dynamic metabolons, X-ray crystallography is not feasible. In these cases, indirect approaches are utilized to characterize the channeling.

1.3.4.1 Isotope dilution. Isotope-labeled precursors are used to track radioactivity changes in multistep reactions. An excessive amounts of nonradioactive intermediates (I) in bulk solution will compete with endogenous radioactive intermediates (I*) and lower the ratio of radioactivity of labeled product (P*) to that of labeled substrate (S*). In the case of substrate channeling, I* will not be diluted by I and the radioactivity ratio (P*/S*) should be near unity.[44,58]

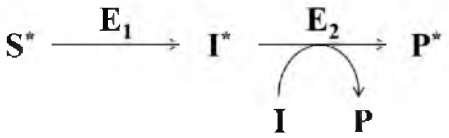

1.3.4.2 Transient-time analysis. Transient time is a key parameter for analyzing coupled enzymatic reactions. It refers to the intermediate lifetime during a catalytic cycle, which is the sum of time required for release of intermediate from the active site of the first

enzyme (E_1), diffusional transit to the second enzyme (E_2) and binding to the active site of E_2. In a coupled reaction model,

$$\mathbf{S} \xrightarrow[v_1]{\mathbf{E_1}} \mathbf{I} \xrightarrow[k]{\mathbf{E_2}} \mathbf{P}$$

The first reaction proceeds constantly within the sampling period at rate of v_1, and the rate constant k of the transient process can be taken as the apparent first order rate constant of the second reaction. Then the following relationships can be obtained:

$$[\mathbf{P}] = v_1 t - \frac{v_1}{k}\left(1\text{-}e^{-kt}\right)$$

$$[\mathbf{I}] = \frac{v_1}{k}\left(1\text{-}e^{-kt}\right)$$

$$k \equiv \frac{1}{\tau} = \frac{k_{cat2}[\mathbf{E_2}]}{K_{m2}} = V_{max2}/K_{m2}$$

In coupled enzyme activity assays, transient time, τ, is derived from the interval between the starting of sequential reactions upon mixing enzymes with substrate and the time when final product formation reaches its maximal rate (Figure 1.4).[42,58,59]

1.3.4.3 Competing reactions. *In vivo* intermediates are always subject to more than one metabolic pathway. In a free-diffusing system, escaped intermediates will be captured by an additional competing enzyme (E_c), generating another product (P_c) that can be monitored by a spectrophotometer. As a result, formation of its original product will be reduced, but in the direct transfer system, intermediates are not trapped by E_c and product formation is not affected. However, this method is only practical when E_c does not interact with examined enzymes.[44,58]

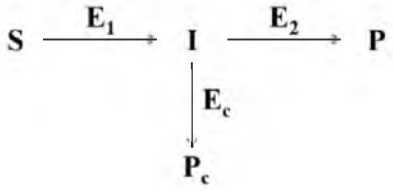

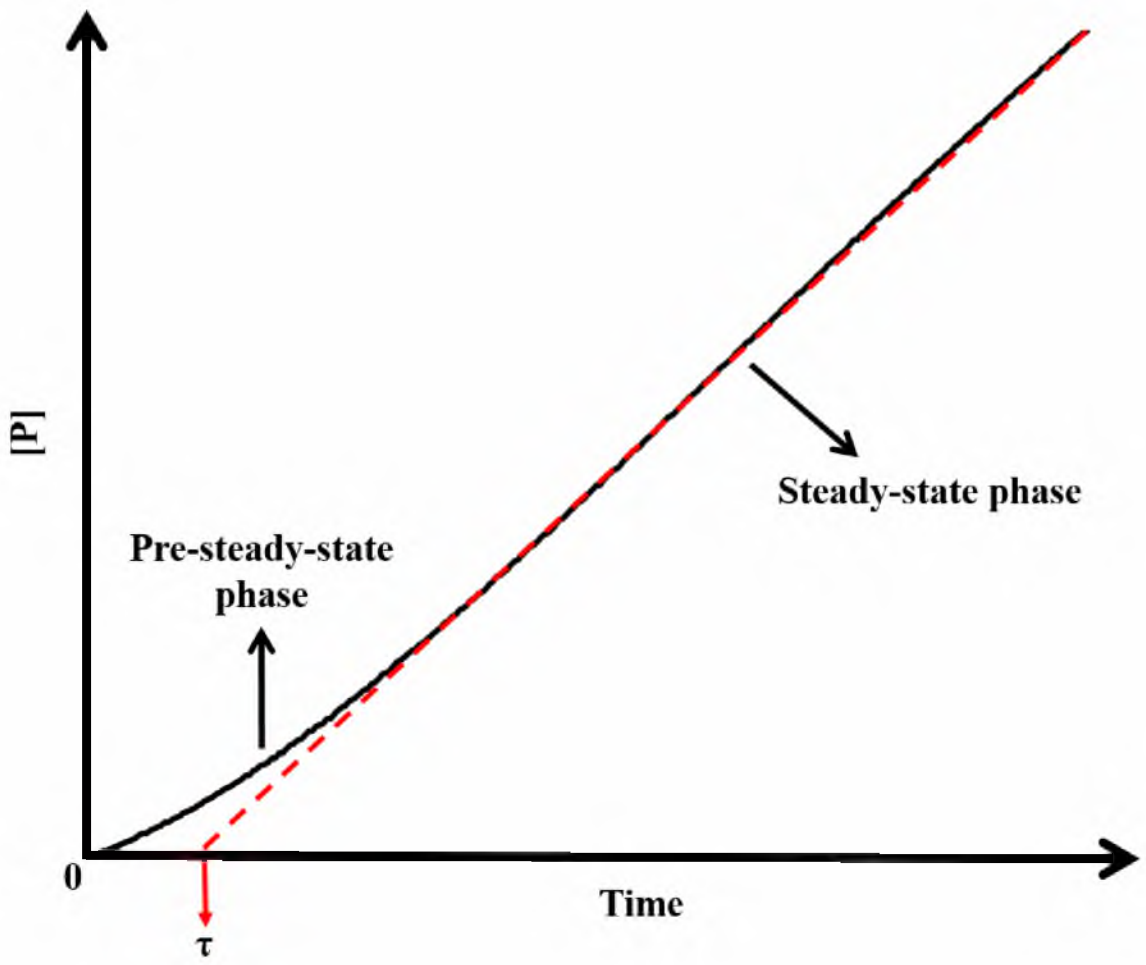

Figure 1.4 Transient time in an enzymatic coupled reaction. Red dashed line is drawn from the linear steady-state phase in the product concentration curve versus time and extrapolated to the time axis.

1.3.4.4 Transient-state or fast kinetics. Transient-state kinetic measurements are designed to monitor a single turnover at sufficiently short time increments with enough enzyme amount (from several to hundreds of micromolar). Thus it can, in principle, probe intermediate and enzyme forms as well as their transitions at molecular level. A commonly used technique is the chemical quench-flow method. Generally, it mixes enzyme and substrate very rapidly with controllable syringes, followed by quick termination of reaction by another quenching agent at a certain point of time. With this method, any detectable spectral changes associated with transitions of enzymes, intermediates and products can be quantified.[58,60]

1.3.4.5 Computer simulation. Brownian dynamics (BD) simulation combined with experimental results has been used in studying intermediate motion under the influence of random collision with solvent molecules and interactions with the electrostatic field of the enzyme. Using this approach, Elcock *et al.* demonstrated an over 80% efficiency of transferring 7,8-dihydrofolate in thymidylate synthase-dihydrofolate reductase, which is highly consistent with the experimentally observed decrease in transient time.[61]

1.3.5 Significance of Metabolons to Enzymatic Biofuel Cells

The current generated at an enzyme cascade-modified bioanode is mainly affected by catalyst loading, local substrate concentration and the length for intermediate diffusion between sequential enzymes. Applying metabolons as the bioelectrocatalysts in a BFC, the current will in principle be enhanced as a consequence of (1) increased loading capacity on electrode surface with dense packing (confined spatial organization) of enzymes, (2) increased local substrate/intermediate concentration and (3) decreased transit time due to close proximity and substrate channeling within metabolons.[33] However, there are few

examples of using natural metabolons directly in enzymatic BFCs. This is because of the hindrance in isolation of intact dynamic complexes. In one pyruvate/air BFC, Moehlenbrock *et al.* provided a relatively simple method. They chemically cross-linked the TCA cycle metabolon *in situ* before rupturing the mitochondria membrane. The crude lysate containing fixed intact metabolons was directly co-immobilized with modified Nafion® polymer onto the anode. The resultant maximum current density increased by nearly 50% as compared to native lysate. Although the power density was low (around 24 $\mu W/cm^2$), which was probably due to the presence of unwanted materials and cross-linker deactivation, this system is still a plausible proof of the potential advantage of metabolons as bioelectrocatalysts for enzymatic BFCs.[62]

1.4 Designing Artificial Metabolons

In the realm of *in vitro* multienzyme biocatalysts, the bottleneck is the fragility and difficulty in isolation of intact natural metabolons. Therefore, considerable efforts have been put into making artificial metabolons with enhanced stability and substrate channeling. However, making a metabolon biomimic does not mean just bringing enzymes together. The three-dimensional orientation of enzymes is crucial for the formation of substrate channeling across the interface. Different fixation and immobilization strategies have been exploited to achieve this goal.[63]

1.4.1 Cross-Linked Enzyme Crystals or Aggregates

Cross-linking can be simply done by conjugating two interacting enzymes in solution. This often requires a bifunctional reagent (cross-linker) that can react with two distinct residues (mostly lysine and cysteine) on proteins, thus creating cross-linked enzyme crystals (CLECs) or precipitated aggregates (CLEAs) when crystallization is not

feasible. A common issue with cross-linking is the enzyme deactivation by small cross-linkers. Larger or even polymeric cross-linkers can avoid this problem, but they may also lead to overaggregation or formation of unwanted complexes.[64,65]

1.4.2 Encapsulation of Enzyme Cascade

The whole metabolic pathway may be encapsulated into a nanocontainer, which can be micelles, liposomes, polymersomes or even virus capsids. Ideally, the container should have the right size for holding all sequential enzymes in close proximity and allowing them to adopt the appropriate conformation. In practice, this method has been extensively employed for single to three enzymes, but encapsulation of the entire pathway is technically difficult. Moreover, materials used for fabricating nanocontainers may interact with enzymes and interfere with desired protein-protein interactions. Encapsulation will also bring additional barriers for mass transport and electrode-enzyme communication.[66-69]

1.4.3 Oriented Co-localization to a Scaffold

Using genetic modification, a number of affinity tags can now be fused to proteins at specific sites. To a particularly selected or designed scaffold, multiple enzymes can be positioned at desired location with restricted orientation. Polyhistidine-tagged (usually at C- or N-terminus) enzymes can be chelated to Ni^{2+}-plated surface.[63] Enzymes bearing cellulose binding domain (CBD) can be co-immobilized onto one cellulose support. For example, a macromolecular complex named cellulosome from anaerobic cellulolytic bacteria has multiple CBD-affinitive domains, allowing co-localization of an enzyme cascade.[70,71] Protein and nucleic acid scaffolds are attracting increasing interest because of their flexibility in shape and dimension. Proliferating cell nuclear antigen (PCNA), a ring-

shaped protein scaffold, was used to establish a three-enzyme complex that gained significantly higher electron transfer efficiency than a free-enzyme system.[72] An artificial protein scaffold was also investigated by combining specific protein-protein interaction domains for enzymes of interest and proved to achieve optimized metabolic flux.[73] DNA and RNA scaffolds are examined to assemble enzyme cascades into different shapes, from one-dimensional strands to two-dimensional triangles. These strategies can facilitate ordered organization of enzymes on restricted locations; however, they actually cannot control the relative orientation of enzymes as natural metabolons do.[74-76]

1.4.4 Genetically Fused Multienzyme Complex

Enzyme cascades can be expressed as a multifunctional protein by fusing respective genes into one encoding all the active sites. Translated polypeptide chains will fold *in vivo* with the original tertiary structures of individual enzymes retained. The resultant fusion protein is then subject to regular isolation/purification procedures for further *in vitro* application. Shatalin *et al.* coupled two TCA cycle enzymes, mMDH to CS, by gene fusion and showed the evidence of channeling of oxaloacetate in the presence of a competing enzyme.[51] Another example is a three-enzyme protein consisting of β–galactosidase, galactokinase and galactose dehydrogenase, which also demonstrated substrate channeling with decreased transient time and increased steady-state reaction rate.[77] Even though gene fusion has the advantage in making robust artificial metabolons in the absence of any additional scaffolds, it may cause failure in folding of higher ordered (more than three enzymes) fusion proteins.[63]

1.4.5 Site-Specifically Conjugated Enzyme Complex

Another elegant establishment of artificial metabolons is site-specifically conjugated multienzyme complexes. Rather than being folded as a whole protein *in vivo*, intact enzymes can be hybridized *in vitro* through linkages at specific modified residues, such as lysines, cysteines, tyrosines, tryptophans and even nonnatural amino acids. Site-directed mutation will turn amino acids of interest into either specifically tagged or reactive residues. Specifically tagged residues can be directed to a particular spot on the other enzyme and bridged by the attached linker. Reactive residues will directly target its interacting partner in very close proximity without additional linkers. Both protocols are highly selective and avoid potential activity loss caused by traditional chemical cross-linking. The resultant conjugated complexes often regain their native orientations *in vivo* and exhibit substrate channeling.[77-79] One example is the bioconjugation of monooxygenase cytochrome P450, putidaredoxin (Pdx) and Pdx reductase done by Hirakawa *et al.* This synthetic complex achieved a drastic enhancement in electron transfer rate between active centers.[80] As a prerequisite for this strategy, structural information on protein-protein interactions should be provided in order to choose the candidate residues for site-specific mutation.

In summary, covalent or noncovalent, solution-based or scaffold-based, chemical or genetical strategies have been exploited for metabolon mimics. Each of the methods discussed above has its own advantages and drawbacks, but the ultimate goal of all is to mimic efficient substrate/intermediate channeling. So far, most of these trials have been made for synthetic purposes, except that encapsulation and scaffold-mediated co-immobilization are under frequent investigation for improving bioelectrocatalytic

efficiency. Genetic manipulation opens a new gate into rational design of synthetic metabolons.

1.5 Aims of Dissertation Research

This dissertation work is aimed at understanding the fundamental nature of the TCA cycle metabolon from mechanistic and structural perspectives. By exploring the basic driving force for protein-protein interactions in mitochondrion, this research focuses on connecting studies of natural metabolons and artificial metabolons including engineered complexes for further catalytic application in enzymatic BFCs.

Uneven distribution of metabolites (metabolite pools) is a phenomena characteristic of metabolons *in vivo*. According to recent progress on enzymatic nanomotors, chemical concentration gradients may play a nonnegligible role in localization and compartmentation of metabolic pathways. Chapter 2 describes the mechanism study of the transport of mMDH and CS in response to substrate concentration gradient in a microfluidic channel.

As the first enzyme, CS links glycolysis and the TCA cycle, which makes it a good starting point for investigation of the whole metabolon. In Chapter 3, a structural study focused on interactions between CS and its two functionally connected partners, mMDH and ACO, is described. *In vivo* cross-linking and mass spectrometry was utilized to screen interacting residues, and computer-aided protein docking was involved to solve the structure of the natural mMDH-CS-ACO association.

Chapters 4 and 5 discuss two strategies of making metabolon mimics *in vitro*. In Chapter 4, different polymeric platforms were evaluated by FRET imaging to characterize their respective confinement effect on the organization of mMDH, CS and ACO. Work

described in Chapter 5 was done in collaboration with Dr. Scott A. Banta at Columbia University on an artificial metabolon using engineered mMDH and CS. This dissertation will discuss the structural analysis of cross-linked recombinant complexes by mass spectrometry and protein docking, and spectrophotometric characterization of substrate channeling.

1.6 References

(1) Bohinski, R. C. In *Modern Concepts in Biochemistry*; 5th ed.; Allyn and Bacon, Inc.: Newton, **1987**, p 540.

(2) Raimundo, N.; Baysal, B. E.; Shadel, G. S. *Trends. Mol. Med.* **2011**, *17*, 641.

(3) Scheffler, I. E. In *Mitochondria*; John Wiley & Sons, Inc: New York, **1999**, p 246.

(4) Wiegand, G.; Remington, S. J. *Ann. Rev. Biophys. Chem.* **1986**, *15*, 97.

(5) Lloyd, S. J.; Lauble, H.; Prasad, G. S.; Stout, C. D. *Protein Sci.* **1999**, *8*, 2655.

(6) LaPorte, D. C. *J. Cell. Biochem.* **1993**, *51*, 14.

(7) Sheu, K. F.; Blass, J. P. *Ann. NY. Acad. Sci.* **1999**, *893*, 61.

(8) Hsueh, S.-C.; Pan, L.-Y.; Lee, M.-C.; Lee, A.-C. *J. Mar. Sci. Technol.* **2013**, *21*, 493.

(9) Fraser, M. E.; Hayakawa, K.; Hume, M. S.; Ryan, D. G.; Brownie, E. R. *J. Biol. Chem.* **2006**, *281*, 11058.

(10) Sun, F.; Huo, X.; Zhai, Y.; Wang, A.; Xu, J.; Su, D.; Bartlam, M.; Rao, Z. *Cell* **2005**, *121*, 1043.

(11) Yogev, O.; Naamati, A.; Pines, O. *FEBS J.* **2011**, *278*, 4230.

(12) Minarik, P.; Tomaskova, N.; Kollarova, M.; Antalik, M. *Gen. Physiol. Biophys.* **2002**, *21*, 257.

(13) Nunes-Nesi, A.; Araujo, W. L.; Obata, T.; Fernie, A. R. *Curr. Opin. Plant. Biol.* **2013**, *16*, 335.

(14) Williamson, J. R.; Cooper, R. H. *FEBS Lett.* **1980**, *117*, K73.

(15) Keys, D. A.; McAlister-Henn, L. *J. Bacteriol.* **1990**, *172*, 4280.

(16) Gelpi, J. L.; Dordal, A.; Monsterrat, J.; Mazo, A.; Cortes, A. *Biochem. J.* **1992**, *283*, 289.

(17) Araujo, W. L.; Nunes-Nesi, A.; Nikoloski, Z.; Sweetlove, L. J.; Fernie, A. R. *Plant Cell Environ.* **2012**, *35*, 1.

(18) Berg, J. M.; Tymoczko, J. L.; Stryer, L. *Biochemistry*; W. H. Freeman and Company: New York, **2002**.

(19) Bisswanger, H. In *Enzyme Kinetics: Principles and Methods*; 2nd ed.; Verlag GmbH & Co. KGaA: Weinheim, **2002**, p 63.

(20) Aquino Neto, S.; Andrade, A. R. D. *J. Braz. Chem. Soc.* **2013**, *24*, 1891.

(21) Bullen, R. A.; Arnot, T. C.; Lakeman, J. B.; Walsh, F. C. *Biosens. Bioelectron.* **2006**, *21*, 2015.

(22) Davis, F.; Higson, S. P. *Biosens. Bioelectron.* **2007**, *22*, 1224.

(23) Tasca, F.; Gorton, L.; Kujawa, M.; Patel, I.; Harreither, W.; Peterbauer, C. K.; Ludwig, R.; Noll, G. *Biosens. Bioelectron.* **2010**, *25*, 1710.

(24) Lang, Q.; Yin, L.; Shi, J.; Li, L.; Xia, L.; Liu, A. *Biosens. Bioelectron.* **2014**, *51*, 158.

(25) Aquino Neto, S.; Suda, E. L.; Xu, S.; Meredith, M. T.; De Andrade, A. R.; Minteer, S. D. *Electrochim. Acta* **2013**, *87*, 323.

(26) Arechederra, R. L.; Minteer, S. D. *Fuel Cells* **2009**, *9*, 63.

(27) Arechederra, R. L.; Treu, B. L.; Minteer, S. D. *J. Power Sources* **2007**, *173*, 156.

(28) Xu, S.; Minteer, S. D. *ACS Catal.* **2012**, *2*, 91.

(29) Zhou, M.; Zhou, N.; Kuralay, F.; Windmiller, J. R.; Parkhomovsky, S.; Waldes-Ramirez, G.; Kartz, E.; Wang, J. *Angew. Chem. Int. Ed.* **2012**, *51*, 2686.

(30) Sokic-Lazic, D.; de Andrade, A. R.; Minteer, S. D. *Electrochim. Acta* **2011**, *56*, 10772.

(31) Sokic-Lazic, D.; Minteer, S. D. *Electrochem. Solid St.* **2009**, *12*, F26.

(32) Tsujimura, S.; Fukuda, J.; Shirai, O.; Kano, K.; Sakai, H.; Tokita, Y.; Hatazawa, T. *Biosens. Bioelectron.* **2012**, *34*, 244.

(33) Moehlenbrock, M. J.; Toby, T. K.; Pelster, L. N.; Minteer, S. D. *ChemCatChem* **2011**, *3*, 561.

(34) Srere, P. A. *TIBS* **2000**, *25*, 150.

(35) Ovadi, J.; Srere, P. A. *Cell Biochem. Funct.* **1996**, *14*, 249.

(36) Mathews, C. K. *J. Bacteriol.* **1993**, *175*, 6377.

(37) Ovadi, J.; Srere, P. A. *Int. Rev. Cytol.* **2000**, *192*, 255.

(38) Srere, P. A. *Ann. Rev. Biochem.* **1987**, *56*, 89.

(39) Oaks, A.; Bidwell, R. G. S. *Annue. Rev. Plant. Physiol.* **1970**, *21*, 43.

(40) Araiza-Olivera, D. In *Cell Metabolism: Cell Homestasis and Stress Response*; Bubulya, P., Ed.; InTech: Rijeka, **2012**, p 101.

(41) Srere, P. A.; Knull, H. R. *TIBS* **1998**, *23*, 319.

(42) Srere, P. A.; Mathews, C. K. *Method. Enzymol.* **1990**, *182*, 539.

(43) Miles, E. W.; Rhee, S.; Davies, D. R. *J. Biol. Chem.* **1999**, *274*, 12193.

(44) Huang, X.; Holden, H. M.; Raushel, F. M. *Annu. Rev. Biochem.* **2001**, *70*, 149.

(45) Thoden, J. B.; Holden, H. M.; Wesenberg, G.; Raushel, F. M.; Rayment, I. *Biochemistry* **1997**, *36*, 6305.

(46) Anderson, K. S.; Miles, E. W.; Johnson, K. A. *J. Biol. Chem.* **1991**, *266*, 8020.

(47) Kim, J. H.; Krahn, J. M.; Tomchick, D. R.; Smith, J. L.; Zalkin, H. *J. Biol. Chem.* **1996**, *271*, 15549.

(48) Atreya, C. E.; Johnson, E. F.; Williamson, J.; Chang, S. Y.; Liang, P. H.; Anderson, K. S. *J. Biol. Chem.* **2003**, *278*, 28901.

(49) Knighton, D. R.; Kan, C.; Howland, E.; Janson, C. A.; Hostomska, Z.; Welsh, K. M.; Mathews, D. A. *Nat. Struct. Biol.* **1994**, *1*, 186.

(50) Elcock, A. H.; McCammon, J. A. *Biochemistry* **1996**, *35*, 12652.

(51) Shatalin, K.; Lebreton, S.; Rault-Leonardon, M.; Velot, C.; Srere, P. A. *Biochemistry* **1999**, *38*, 881.

(52) Robinson, J. B. J.; Inman, L.; Sumegi, B.; Srere, P. A. *J. Biol. Chem.* **1986**, *262*, 1786.

(53) Hyde, C. C.; Ahmed, S. A.; Padlan, E. A.; Miles, E. W.; Davies, D. R. *J. Biol. Chem.* **1988**, *263*, 17857.

(54) Rhee, S.; Parris, K. D.; Ahmed, S. A.; Miles, E. W.; Davies, D. R. *Biochemistry* **1996**, *35*, 4211.

(55) Krahn, J. M.; Kim, J. H.; Burns, M. R.; Parry, R. J.; Zalkin, H.; Smith, J. L. *Biochemistry* **1997**, *36*, 11061.

(56) Ævarsson, A.; Seger, K.; Turley, S.; Sokatch, J. R.; Hol, W. G. J. *Nat. Struct. Biol.* **1999**, *6*, 785.

(57) Ladenstein, R.; Ritsert, K.; Huber, R.; Richter, G.; Bacher, A. *Eur. J. Biochem.* **1994**, *223*, 1007.

(58) Spivey, H. O.; Ovadi, J. *Methods* **1999**, *19*, 306.

(59) Ovadi, J.; Tompa, P.; Vertessy, B.; Orosz, F.; Keleti, T.; Welch, G. R. *Biochem. J.* **1989**, *257*, 187.

(60) Johnson, K. A. *Method. Enzymol.* **1995**, *249*, 38.

(61) Elcock, A. H.; Huber, G.; McCammon, J. A. *Biochemistry* **1997**, *36*, 16049.

(62) Moehlenbrock, M. J.; Toby, T. K.; Waheed, A.; Minteer, S. D. *J. Am. Chem. Soc.* **2010**, *132*, 6288.

(63) Schoffelen, S.; van Hest, J. C. M. *Soft Matter* **2012**, *8*, 1736.

(64) Quiocho, F. A.; Richards, F. M. *Proc. Natl. Acad. Sci. U. S. A.* **1964**, *52*, 833.

(65) Sheldon, R. A. *Biochem. Soc. Trans.* **2007**, *35*, 1583.

(66) Klyachko, N. L.; Levashov, A. V. *Curr. Opin. Colloid Interface Sci.* **2003**, *8*, 179.

(67) Walde, P.; Sosaku, I. *Biomol. Eng.* **2001**, *18*, 143.

(68) de Hoog, H. M.; Nallani, M.; Cornelissen, J. J. L. M.; Rowan, A. E.; Nolte, R. J. M.; Arends, I. W. C. E. *Org. Biomol. Chem.* **2009**, *7*, 4604.

(69) de la Escosura, A.; Nolte, R. J. M.; Cornelissen, J. J. L. M. *J. Mater. Chem.* **2009**, *19*, 2274.

(70) Mingardon, F.; A., C.; Tardif, C.; Bayer, E. A.; Fierobe, H.-P. *Appl. Environ. Microbiol.* **2007**, *73*, 7138.

(71) Bayer, E. A.; Belaich, J.-P.; Shoham, Y.; Lamed, R. *Annu. Rev. Microbiol.* **2004**, *58*, 521.

(72) Hirakawa, H.; Nagamune, T. *ChemBioChem* **2010**, *11*, 1517.

(73) Dueber, J. E.; Wu, G. C.; Malmirchegini, G. R.; Moon, T. S.; Petzold, C. J.; Ullal, A. V.; Prather, K. L. J.; Keasling, J. D. *Nat. Biotechnol.* **2009**, *27*, 753.

(74) Muller, J.; Niemeyer, C. M. *Biochem. Biophys. Res. Commun.* **2008**, *377*, 62.

(75) Vong, T.; Schoffelen, S.; van Dongen, S. F. M.; van Beek, T. A.; Zuilhof, H.; van Hest, J. C. M. *Chem. Sci.* **2011**, *2*, 1278.

(76) Delebecque, C. J.; Lindner, A. B.; Silver, P. A.; Aldaye, F. A. *Science* **2011**, *333*, 470.

(77) Basle, E.; Joubert, N.; Pucheault, M. *Chem. Biol.* **2010**, *17*, 213.

(78) Foley, T.; Burkart, M. D. *Curr. Opin. Chem. Biol.* **2007**, *11*, 12.

(79) Lin, Y. A.; Chalker, J. M.; Davis, B. G. *ChemBioChem* **2009**, *10*, 959.

(80) Hirakawa, H.; Kamiya, N.; Tanaka, T.; Nagamune, T. *Protein Eng., Des. Sel.* **2007**, *20*, 453.

CHAPTER 2

INTERMEDIATE CONCENTRATION GRADIENT MEDIATED TCA CYCLE METABOLON FORMATION

2.1 Background Introduction

2.1.1 Mass Transport in Solution

Three types of mass transport can occur in an aqueous phase: diffusion, migration and convection. Diffusion is the random motion of a molecule (*i*) with the tendency to move down the gradient of chemical potential, such as a concentration gradient, $\partial C_i(x)/\partial x$. Migration is the movement of an ion driven by an electric field, such as an electric potential gradient, $\partial \phi(x)/\partial x$. Convection occurs when a density gradient, a temperature gradient or an external force, such as stirring, drives the flow at a rate of $v(x)$.

The diffusive motion of *i* in the x direction is a result of one-dimensional random walks that can be described by

$$\Delta x^2 = 2D_i t$$

Where the diffusion coefficient, D_i, is defined as the ratio of the mean-square displacement over time.

$$D_i = \Delta x^2/2t$$

The expansion of one-dimensional diffusion to two- and three-dimensional diffusion yields the following relationships:

Reprinted from "Wu, F., Pelster, L. N., Minteer, S. D. *Chem. Commun.* **2015**, *55*, 1244" with permission from the Royal Society of Chemistry

$$\Delta x^2 = 4D_i t, \qquad D_i = \Delta x^2/4t$$

$$\Delta x^2 = 6D_i t, \qquad D_i = \Delta x^2/6t$$

The diffusion coefficient is a characteristic value used to quantitate the diffusivity of a species in a specific medium at a certain temperature. Physical studies on Brownian motion gives the following equation:

$$D_i = \mu_i k_B T$$

The diffusion of a spherical object in solution, however, results in a diffusion coefficient that is a function of its radius (r) and the dynamic viscosity (η) of the medium, as described by the Stokes-Einstein equation:

$$D_i = \frac{k_B T}{6\pi\eta r}$$

In the absence of migration and convection, the one-dimensional diffusive flux in solution is in direct proportion to the concentration gradient, as described by Fick's first law:

$$J_i(x) = -D_i \frac{\partial C_i(x)}{\partial x}$$

When migration and convection are also present, the flux of *i* in the x direction is then determined by the Nernst-Planck equation.[1]

$$J_i(x) = -D_i \frac{\partial C_i(x)}{\partial x} - \frac{z_i F}{RT} D_i C_i \frac{\partial \phi(x)}{\partial x} + C_i v(x)$$

2.1.2 Compartmentalization of Metabolites and Metabolon Formation

Early evidence of metabolons was provided by the observation of the cellular organization of metabolites. It was discovered that precursors for different metabolic pathways are stored in discrete pools. Using the isotope-labeling technique, researchers

were able to follow the partitioning of intermediary metabolites and estimate their pool sizes.[2,3] As discussed in Chapter 1, restricted metabolite diffusion is attributed to macromolecular crowding and electrostatic channeling. Although in-depth research is ongoing, another question has been raised: would the intermediary metabolite pools induce formation of dynamic metabolons? Work on chemoreceptors and chemoattractants in motile bacteria indicated that the degree of receptor protein clustering during cell cycles might be regulated by its binding to the ligand.[4] Norris *et al.* further suggested that the processing of a substrate through the metabolic pathway may promote the co-localization and reversible assembly of membrane transport proteins and downstream enzymes. Additionally, such dynamic organization would dissociate upon the depletion of substrate, making cellular metabolism more efficient and adaptable.[5] They also proposed a conformation-driven sequential affinity enhancement mechanism to explain substrate-activated enzyme complexes. As suggested by their research, the affinity of a substrate-bound enzyme (in its active form) to its functional partner could be increased by conformation alteration, that is, enhanced protein-protein interactions by feedforward substrate activation. The activation would propagate along the metabolic pathway, resulting in a higher degree of protein clustering or aggregation. It has been pointed out that the accumulation of products, on the contrary, would introduce inhibition feedback on enzyme association. Although this hypothesis has not yet been validated with additional experiments, it is in agreement with the generally accepted theory that metabolon formation is closely related to metabolic regulation in terms of the change of metabolite concentrations. Interestingly, Bartholomae *et al.* observed a very weak but specific interaction between mMDH and ICDH in *Bacillus subtilis*, which was stimulated by a

cocktail of their substrates and cofactors including isocitrate, $NADP^+$ and Mg^{2+}, even though the two enzymes are not directly functionally connected in the TCA cycle.[6]

In the hypothesis proposed by Norris *et al.*, apparent diffusion coefficient alteration upon substrate binding was specifically noted for its potential role in driving the formation of a static large proteolipid and complexed metabolon in the membrane.[5] Recent progress on chemotaxic behavior of nanoparticles demonstrated that, with an increased diffusion coefficient in the presence of substrates, some single enzymes can move against a substrate concentration gradient in a similar fashion to a nanomotor.[7-9] Knowing the heterogeneity of metabolite distribution in cells, the early question may be addressed based on the idea of metabolite-linked dynamic complexes and gradient-directed enzyme diffusion. It could be possible that the substrate/intermediate concentration gradient exerts a nonnegligible effect on "dragging" metabolic enzymes together. For instance, microcompartmentalization of intermediates might reversibly hold the dynamic association of the TCA cycle metabolon. To gain further understanding, additional clarity surrounding how model enzymes from the TCA cycle would physically react in response to a metabolite gradient is required.

2.1.3 Structure and Catalytic Mechanism of mMDH

As introduced in Chapter 1, mMDH catalyzes the last reaction of the TCA cycle, in which L-malate is oxidized to OAA. This reaction involves NAD^+ as the cofactor of mMDH and is highly reversible. In solution, mMDH is at the equilibrium between its monomeric, dimeric, and tetrameric forms. Interestingly, the homodimer was previously determined to be the most stable form as it does not undergo dissociation even at 1 nM.[10] Tetramer formation is enhanced at enzyme concentrations higher than 0.67 μM. However,

under physiological conditions, ATP shifts the equilibrium towards the mMDH tetramer with a greatly decreased dissociation constant.[11] It is widely accepted that the dimeric form is more critical for mMDH activity. For pig heart mMDH, each subunit (composed of 314 amino acids) contains one binding site for NAD^+/NADH and one active site for L-malate/oxaloacetate in its C-terminal domain (Figure 2.1A). Dimerization constructs two clefs with other catalytically necessary residues for accommodating substrates into the active site.[12] Previous kinetic studies have shown that mMDH-catalyzed malate dehydrogenation is an ordered mechanism. Substrate binding follows the prebinding of the NAD^+ cofactor to mMDH. Formation of the NAD^+-mMDH-L-malate complex induces a conformational change in mMDH, where the hydrophobic active site vacuole is closed by an external loop to terminate solvent access. A histidine-aspartate pair in the vacuole establishes a charge relay system that allows proton transfer from L-malate to NAD^+.[13-17]

Catalytic performance of mMDH is allosterically regulated. Considering the fact that the conversion of L-malate to OAA is thermodynamically unfavorable (+6.69 kcal)[18], it is expected that excessive quantities of L-malate will facilitate OAA production, while accumulated OAA will inhibit mMDH. In addition, citrate (a product of its subsequent reaction) regulates mMDH activity in a complex manner. It competitively inhibits L-malate dehydrogenation at low [L-malate] or [NAD^+], but activates mMDH at high [L-malate] or [OAA].[19,20]

2.1.4 Structure and Catalytic Mechanism of CS

CS is the first enzyme of the TCA cycle and the subsequent enzyme of mMDH by catalyzing a Claisen condensation of OAA and acetyl-CoA to citrate. In a similar fashion to mMDH, pig heart CS is stable in its dimeric form, where each subunit consists of 437

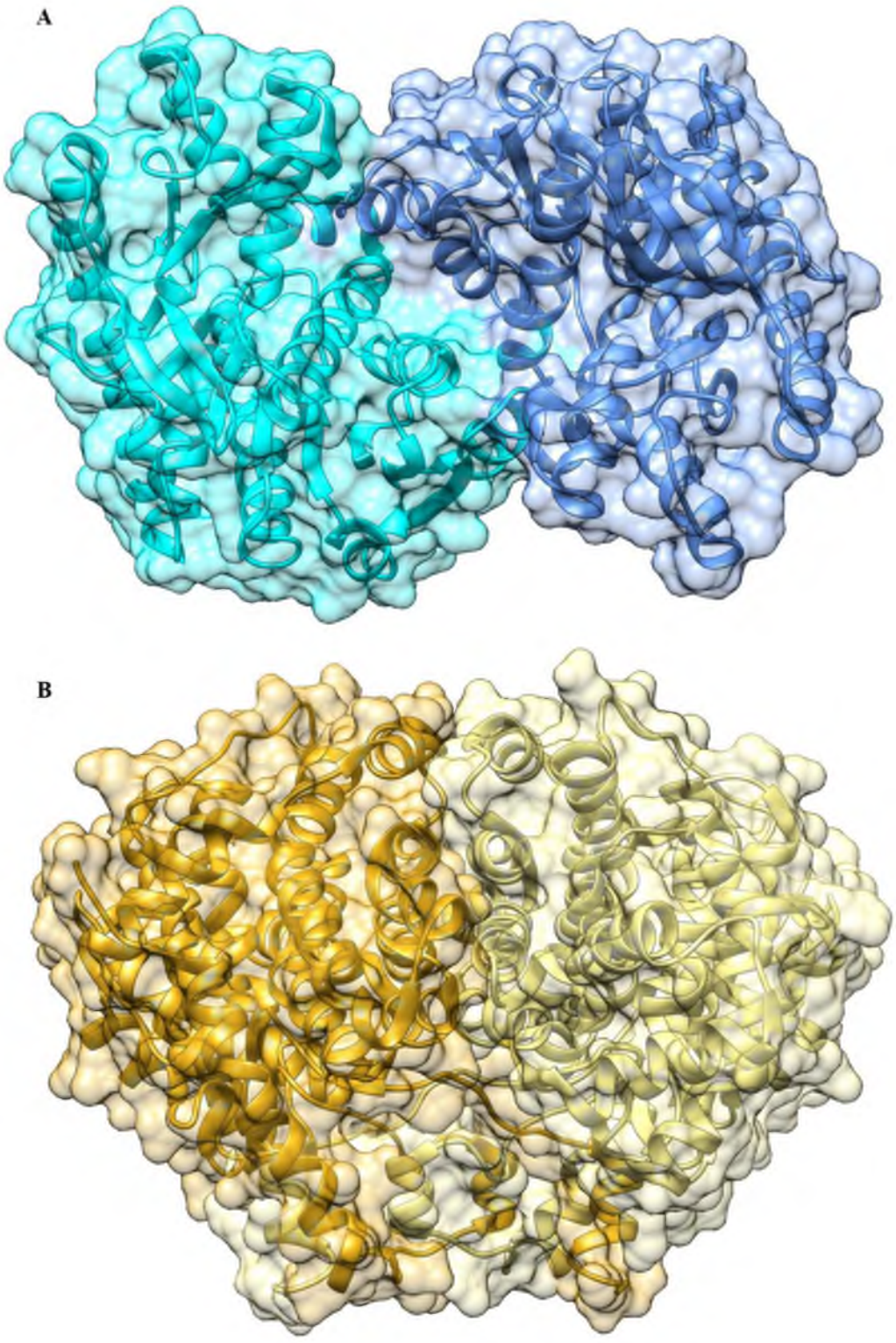

Figure 2.1 Structures of pig heart mMDH (**A**, PDB ID: 1MLD) and CS (**B**, PDB ID: 1CTS).

amino acids and two separate binding sites for OAA/citrate and acetyl-CoA/CoA (Figure 2.1B).[21] The overall reaction is an ordered progress in three steps: (1) a proton abstraction from acetyl-CoA to form an enolized thioester group, (2) condensation of the enolate anion and carboxyl group of OAA to form a citryl-thioester, and (3) citryl-thioester hydrolysis to form citrate and CoA. OAA binding increases the binding constant of CS to acetyl-CoA by at least 20 folds, however, the binding constant of CS to OAA decreases if acetyl-CoA binds first.[22-24] Crystallographic studies have demonstrated that CS undergoes significant shift/rotation of its helices and domain movement upon binding to different ligands. It exhibits a transition between the "open" and "closed" forms of conformation. In its open form, key residues for OAA/citrate accommodation are too far from each other and only 28% of enzyme surface is accessible to solvent molecules. If acetyl-CoA binds first, CS switches to one of the closed forms. The active site for OAA/citrate, however, is deeply buried and completely inaccessible to solvent. It is suggested that prebinding of OAA induces a favorable alteration from the open form to another closed form that bears a well-defined binding site for acetyl-CoA. In this conformation, proton abstraction and condensation occur to form citryl-CoA, which consequently induces the completely closed form for hydrolysis by bound water. Once citrate and CoA are formed, CS must open to release the products.[24-26]

2.1.5 *In Vitro* System for Enzyme Transport Study

Sengupta *et al.* designed a microfluidic device enabling direct characterization of enzyme transport in the presence of a substrate gradient *in vitro*.[8,9] As illustrated in Figure 2.2A, a Y-shaped polydimethylsiloxane (PDMS) microfluidic channel was utilized to generate a chemical concentration gradient across the interface of two laminar flows with

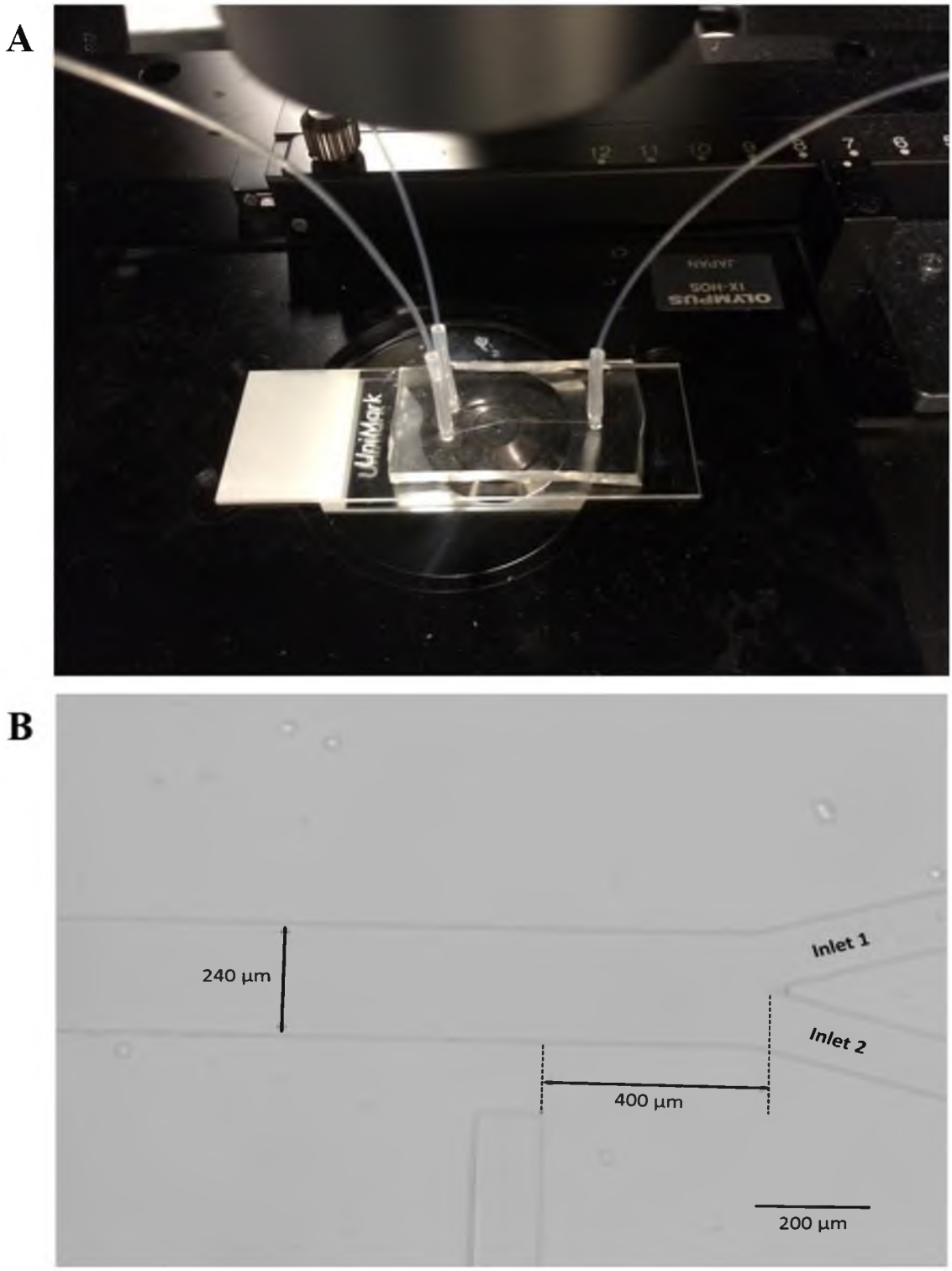

Figure 2.2 Experimental setup of the PDMS microfluidic channel.

different chemical components, infused by a dual syringe pump through separate inlets into the channel. To avoid turbulent flow, injection was conducted very slowly to maintain a low Reynold's number in the fluid. According to Fick's first law, there would be a cross-channel flux of solute from the higher concentration regime to the lower concentration regime. This can be considered as a simulation of the metabolite concentration gradient inside cells or mitochondria. If the gradient can direct single enzyme diffusion from the opposite side, enhanced lateral flux of enzymes toward the concentrated metabolite regione should be observed. When two sequential enzymes are both applied, production of an additional intermediate gradient around the first enzyme might attract the second enzyme to its vicinity, leading to enhanced lateral co-diffusion (Figure 2.3).

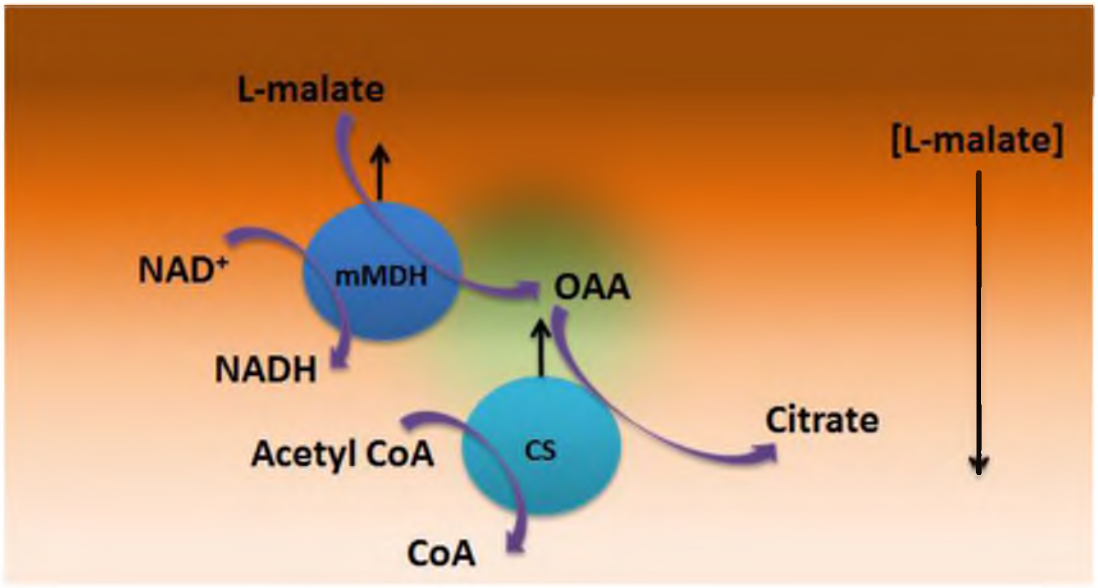

Figure 2.3 Schematic illustration of enhanced diffusion of mMDH and CS in the presence of a concentration gradient of substrate (L-malate) and intermediate (OAA).

2.1.6 Fluorescent Characterization of Enzyme Transport

Fluorescent imaging is a powerful technique in visualizing protein localization and partitioning. By tagging certain amino acids on a protein's surface by small fluorescent probes, one can measure the emissive intensity of fluorophore-labeled proteins in an area of interest under a microscope. In this chapter, two commercial probes (AlexaFluor® 488 and AlexaFluor® 555) were used to modify two model enzymes, mMDH and CS. These probes belong to the family of succinimidyl ester fluorophores, which can selectively react with the primary amine in the side chain of lysine residues and conjugate the fluorescent moiety onto the protein's surface. Since AlexaFluor® 488 and AlexaFluor® 555 have distinct excitation and emission wavelength ranges, fluorescence of two tagged enzymes were monitored independently. Lateral enzyme transport was observed by cross-sectional emission intensity profiles. In the case of enhanced lateral enzyme transport induced by substrate/intermediate gradient, the intensity profile would shift by some extent to the other side of channel. To quantify enzyme transport, lateral shift (l) was defined as the linear distance from the middle point of the channel to where the normalized intensity is 0.5 at the same plane (Figure 2.4). Enhanced lateral enzyme transport resulted in an increase of l. Taking l as how far the enzyme can move during a limited period of time (t), one can use the one-dimensional random walk rule to calculate its apparent diffusion coefficient, D_{app}:

$$D_{app} = \frac{l^2}{2t}$$

2.1.7 Aims

To figure out the mechanism for metabolon formation in a heterogeneous environment, it was hypothesized that the dynamic organization of the TCA cycle enzymes

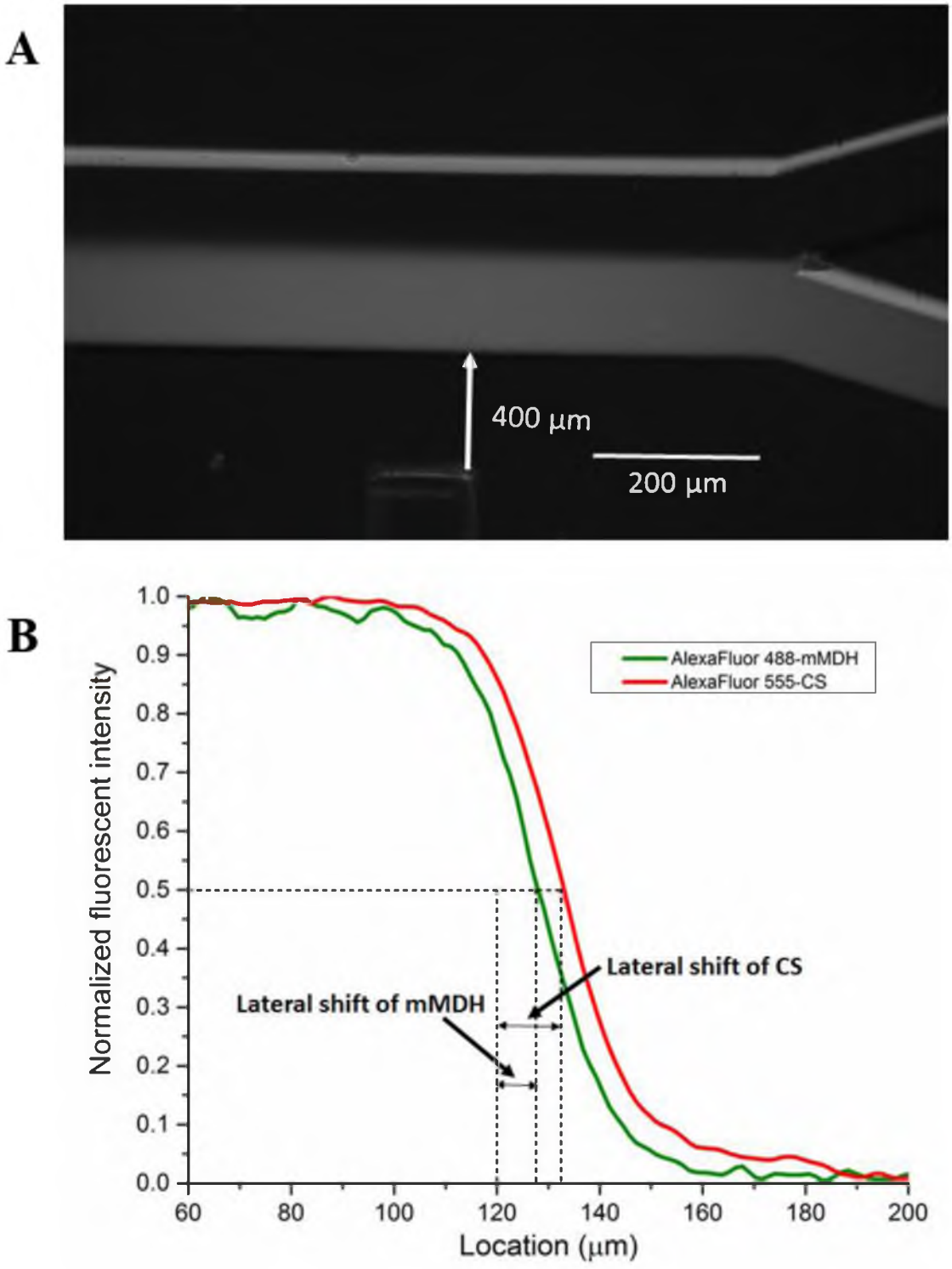

Figure 2.4 Flow containing fluorophore-labeled enzymes in the channel under microscope (**A**) and lateral shift of emission intensity (**B**).

might be favored by the collective directional diffusion of subsequent enzymes induced by an intermediary metabolite concentration gradient between them. To validate this hypothesis, diffusive motion of two TCA cycle enzymes in response to different *in vitro* substrate/intermediate gradients will be investigated.

2.2 Experimental

2.2.1 Materials

Pig heart mMDH, CS, and all chemicals used in this work were purchased from Sigma-Aldrich unless otherwise noted. AlexaFluor® 488 and AlexaFluor® 555 for enzyme labeling were obtained from Invitrogen (Life Technologies). PDMS was purchased as part of the "Silicone Elastomer Kit" from Corning.

2.2.2 Labeling of Enzymes

AlexaFluor® 488 and AlexaFluor® 555 were used to label mMDH and CS, respectively. Approximately 1 mg of mMDH or CS were purified over a prepacked Sephadex™ G-25M column (GE Healthcare) to remove ammonium sulfate and other salts. After being concentrated to approximately 2 mg/mL, the enzymes were mixed with a single vial of dye (as purchased) predissolved in 50 μL of dry DMSO in 1 mL of 50 mM sodium phosphate buffer (pH 8.3). Mixtures of enzymes and fluorophores were incubated in the dark at room temperature for at least 1 h under shaking. Following labeling, excessive fluorophores were removed by overnight dialysis in a dialysis cassette with a molecular mass cutoff of 10 kDa (Thermo Scientific) against 2 L of Tris-HCl buffer (50 mM, pH 7.4) at 4 °C. Additionally, the enzymes were purified through a prepacked Sephadex™ G-25M column followed by multiple centrifugations in Amicon® centrifugal filters (10 kDa molecular weight cutoff, Merck Millipore) at 5000 × g for 15 min until polarization of

labeled enzymes was stabilized at about 0.3. Final fluorophore:enzyme molar ratios were determined by a UV-Vis spectrophotometer (Evolution 260 Bio, Thermo Scientific) to be approximately 1:1.

2.2.3 Enzymatic Assays for Kinetic Measurements and Inhibition Studies

Reaction rates of mMDH-catalyzed L-malate conversion were measured in 100 mM potassium phosphate buffer (pH 7.4) containing 100 nM mMDH, 5 mM NAD^+, and L-malate at 0, 0.5, 1.0, 2.5, 5.0, 10.0, 25, 50 and 100 mM. NADH absorbance at 340 nm (millimolar extinction coefficient is 6.22 mM^{-1} cm^{-1}) was monitored for 100 s in the UV-Vis spectrophotometer. Reaction rates of mMDH-catalyzed OAA conversion were measured in potassium phosphate buffer containing 2.5 nM mMDH, 0.15 mM NADH and OAA at 0.005, 0.01, 0.025, 0.05, 0.075, 0.1, 0.2 and 0.3 mM. NADH absorbance at 340 nm was monitored for 100 s. Reaction rates of CS-catalyzed OAA conversion were measured in potassium phosphate buffer containing 100 nM CS, 0.2 mM acetyl-CoA, 0.4 mM DTNB and OAA at 0, 0.2, 0.4, 0.6, 0.8. 1.0, 2.5, 5.0, 10, 25, 50, 75 and 100 mM. The absorbance increase of DTNB at 412 nm (milimolar extinction coefficient of 13.6 $mM^{-1}cm^{-1}$) was monitored for 100 s. K_m values were determined by fitting reaction rate *versus* substrate concentration to the Michaelis-Menten model, by nonlinear regression. K_i values for the inhibition of mMDH by ATP were determined by fitting multiple plots of reaction rates *versus* L-malate concentrations with 1 mM NAD^+ and ATP at 0, 1, 5, 10 25 and 50 mM.

2.2.4 Coupled Enzyme Activity Assays

Reaction rates of citrate production from L-malate were measured in 100 mM potassium phosphate buffer (pH 7.4) containing 100 nM mMDH, 100 nM CS, 5 mM NAD,

0.2 mM acetyl-CoA, 0.4 mM DTNB and L-malate at 0, 0.5, 1.0, 2.5, 5.0, 10, 25, and 100 mM. The absorbance increase of DTNB at 412 nm was monitored for 2 min. K_m values were determined by fitting the reaction rates *versus* L-malate concentrations to the Michaelis-Menten model by nonlinear regression. The citrate inhibition effect was evaluated in the same assay cocktail by adding in 10 mM citrate. ATP inhibition of mMDH was performed in the same assay cocktail by adding in 25 mM ATP, and the absorbance increase of NADH at 340 nm was monitored for 2 min.

2.2.5 Microfluidic Channel Fabrication

The silicon master pattern for the microfluidic channel was fabricated with SU-8 Negative Photoresist (Microchem) to a height of 100 μm and a width of 240 μm (Figure 2.2B) according to the soft lithography protocol described by Xia *et al.*[27] An additional pattern was introduced close to the channel pattern at 400 μm from the start of channel to mark the position at which fluorescence would be measured. PDMS (premixed with curing agent and degased) was poured onto the master and cured at 75°C for 2 hours. PDMS was then cut and sealed by a microscopic glass slide after being cleaned in a plasma cleaner (PDC-32G, Harrick Plasma). All chips were equilibrated overnight after sealing.

2.2.6 Fluorescent Imaging Setup

Microdialysis tubing (Intech Laboratories) were used to connect the inlets of the PDMS chip to a dual syringe pump (Harvard Apparatus) and the outlet to a beaker for solution waste (Figure 2.2A). All solutions were filtered through syringe filters (0.2 μm, Corning) to remove particles and degassed for at least 15 min immediately prior to the experiment. The PDMS channel was filled with 30% isopropanol and then buffer to avoid bubble generation. Flow in the chip at pumping rate of 500 nL/min was monitored with an

inverted microscope (Olympus IX71). Using a FITC filter cube (excitation: 467-498 nm; emission: 513-556 nm) and a TRITC filter cube (excitation: 532-554 nm; emission: 570-613 nm), fluorescence of AlexaFluor® 488-labeled mMDH and AlexaFluor® 555-labeled CS was recorded simultaneously. Buffered solutions containing substrates and cofactors were injected through Inlet 1. Buffered solutions containing 100 nM AlexaFluor® 488-labeled mMDH or CS were injected through Inlet 2. The observed plane was adjusted to the middle height of the channel between the glass and PDMS plate to avoid any possible wall effects.

2.2.7 Calculation of Apparent Diffusion Coefficients of Enzymes

Since the dual syringe pump infusing rate was set at 0.5 μL/min, the total volumetric flow rate in the channel was 1 μL/min. Knowing that the channel is 240 μm in width and 100 μm in height, we calculated the cross-sectional area to be 2.4×10^4 μm^2. By dividing the total volumetric flow rate by the cross-sectional area, the flow velocity was determined to be 694.4 μm/s. By defining $t_0 = 0$ s at the junction at which the two flows met, the total diffusion time (t) for enzyme molecules at 400 μm from the start of channel was calculated by t = 400 μm ÷ 694 μm/s = 0.58 s. Finally, the value of apparent diffusion coefficient was given by

$$D_{app} = \frac{l^2}{1.16\ \mathrm{sec}}$$

2.3 Results and Discussion

2.3.1 Single and Coupled Enzyme Kinetics

When cofactors are in excess and do not change significantly during the specified time course, Michaelis-Menten parameters can be estimated by treating the enzymatic

reactions as the simple second-order model, as discussed in Chapter 1. For mMDH, although it undergoes an ordered binding mechanism, the change of reaction rate with [L-malate] fits the Michaelis-Menten kinetic model well (Figure 2.5A). K_m for L-malate was determined to be 4.45 mM, and the maximum turnover rate was determined to be 2.12×10^{-3} μmole/min (or 3.53×10^{-7} M/s), so the turnover number of L-malate per mMDH (dimer) was 3.53 s^{-1}. For CS, K_m for OAA was calculated to be 2.81 mM, and the maximum turnover rate was calculated to be 2.32×10^{-2} μmole/min (or 3.87×10^{-6} M/s), with a turnover number of 38.67 s^{-1}. The measured K_m constants for both enzymes are one order of magnitude higher than previously reported values[28,29]. A decrease in substrate affinity and catalytic efficiency may be caused by deactivation during long term storage at -20°C and fluorophore modification at active sites or catalytically necessary lysine residues. When the two reactions were coupled, the apparent K_m to L-malate was reduced to 0.76 mM while the turnover number was 36 s^{-1}. Thus, the final coupled catalytic efficiency (28%) was greatly improved as compared to the catalytic efficiency of single mMDH (0.5%) for L-malate conversion.

2.3.2 Lateral Diffusion of Single Enzymes against a Substrate Gradient

Unlike previously examined enzymes, such as catalase and urease, mMDH and CS require additional cofactors to perform catalysis and the enzymatic reactions are not as simple as the decomposition of hydrogen peroxide or the hydrolysis of urea, making the system more complex (albeit tunable) for a mechanistic study. To examine enzyme transport stimulated by the substrate concentration, the D_{app} values of mMDH and CS without additional cofactors were initially measured, where catalysis did not occur. As

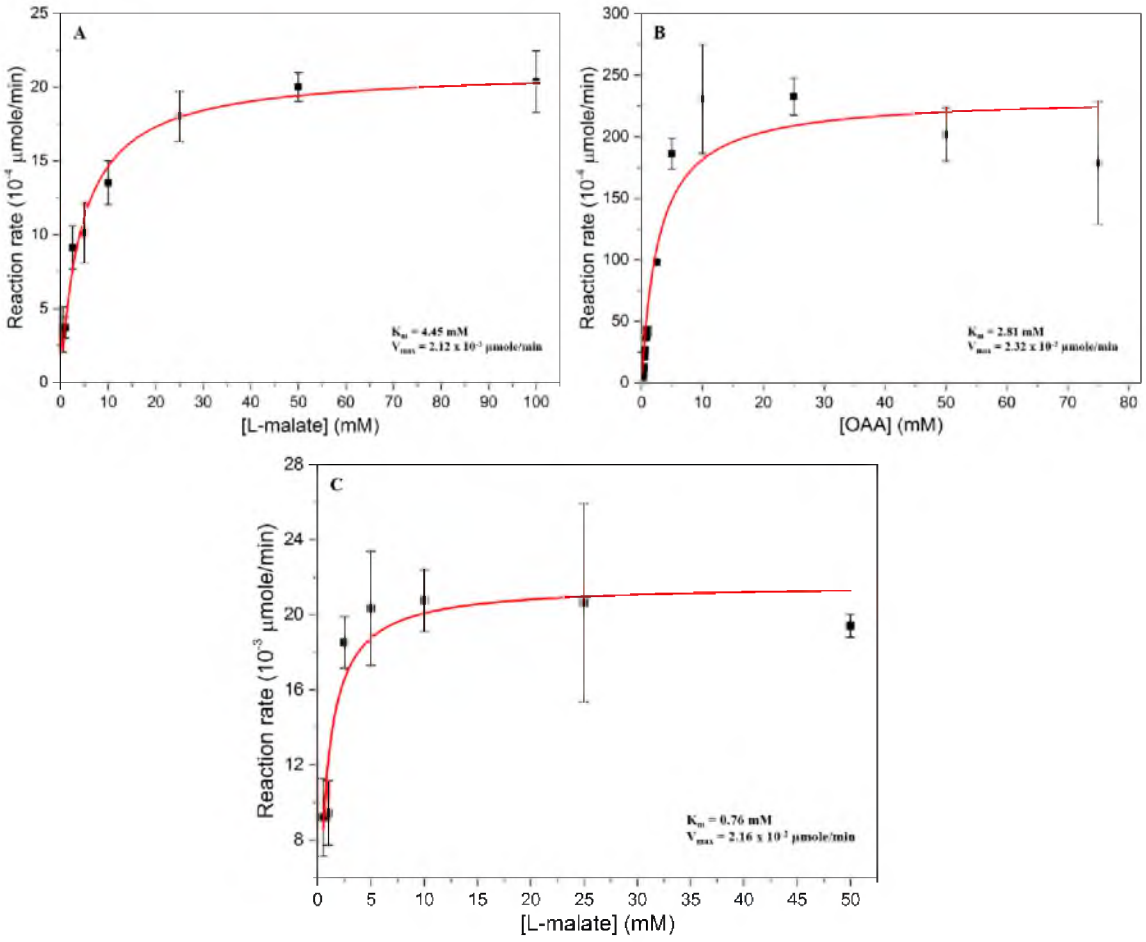

Figure 2.5 Change of reaction rate with substrate concentration: (**A**) mMDH-catalyzed L-malate conversion to OAA, (**B**) CS-catalyzed OAA conversion to citrate, (**C**) mMDH/CS-catalyzed L-malate conversion to citrate.

shown in Figure 2.6, in the absence of catalysis the D_{app} increased as more substrate was introduced and reached a maximum when the enzyme active sites were saturated. For mMDH, increasing the L-malate concentration from 0 mM to 50 mM resulted in an increase of D_{app} from 3.88×10^{-7} cm^2/s (l = 6.65 μm) against buffer to a maximum of 1.03×10^{-6} cm^2/s (l = 10.81 μm) against 50 mM L-malate. For CS, increasing the OAA concentration from 0 mM to 10 mM also increased the D_{app} from 7.25×10^{-7} cm^2/s (l = 10.66 μm) against buffer to a maximum of 2.07×10^{-6} cm^2/s (l = 15.36 μm) against 10 mM OAA. Interestingly, the enhancement of the lateral shift of mMDH or CS did not require catalysis to occur, which subsequently ruled out self-electrophoresis induced by charged products or self-propulsion driven by environmental changes, including the alteration of local pH, ionic strength, and temperature associated with enzymatic reactions as potential driving forces. In this case, electrophoresis of enzymes has been considered. The external electric field created by the pool of charged species on the other side of channel could induce the electrophoresis of enzymes across the interface, which might be possible for enhance lateral flux of mMDH as L-malate and enzyme molecules (pI of 10)[30] were oppositely charged under experimental conditions. However, electrostatic attraction is not convincing for OAA and CS molecules (pI of 6.1-6.6)[31], both of which were negatively charged.

2.3.3 Lateral Diffusion of Single Enzymes Enhanced by Catalysis

After the addition of cofactors (5 mM NAD^+ for mMDH and 0.2 mM acetyl CoA for CS), the change of D_{app} with a substrate concentration gradient was quite different. In the presence of NAD^+, the D_{app} of mMDH showed a significantly larger increase (224%) from 4.82×10^{-7} cm^2/s (l=7.41 μm) against 0 mM L-malate to 1.56×10^{-6} cm^2/s (l = 13.45

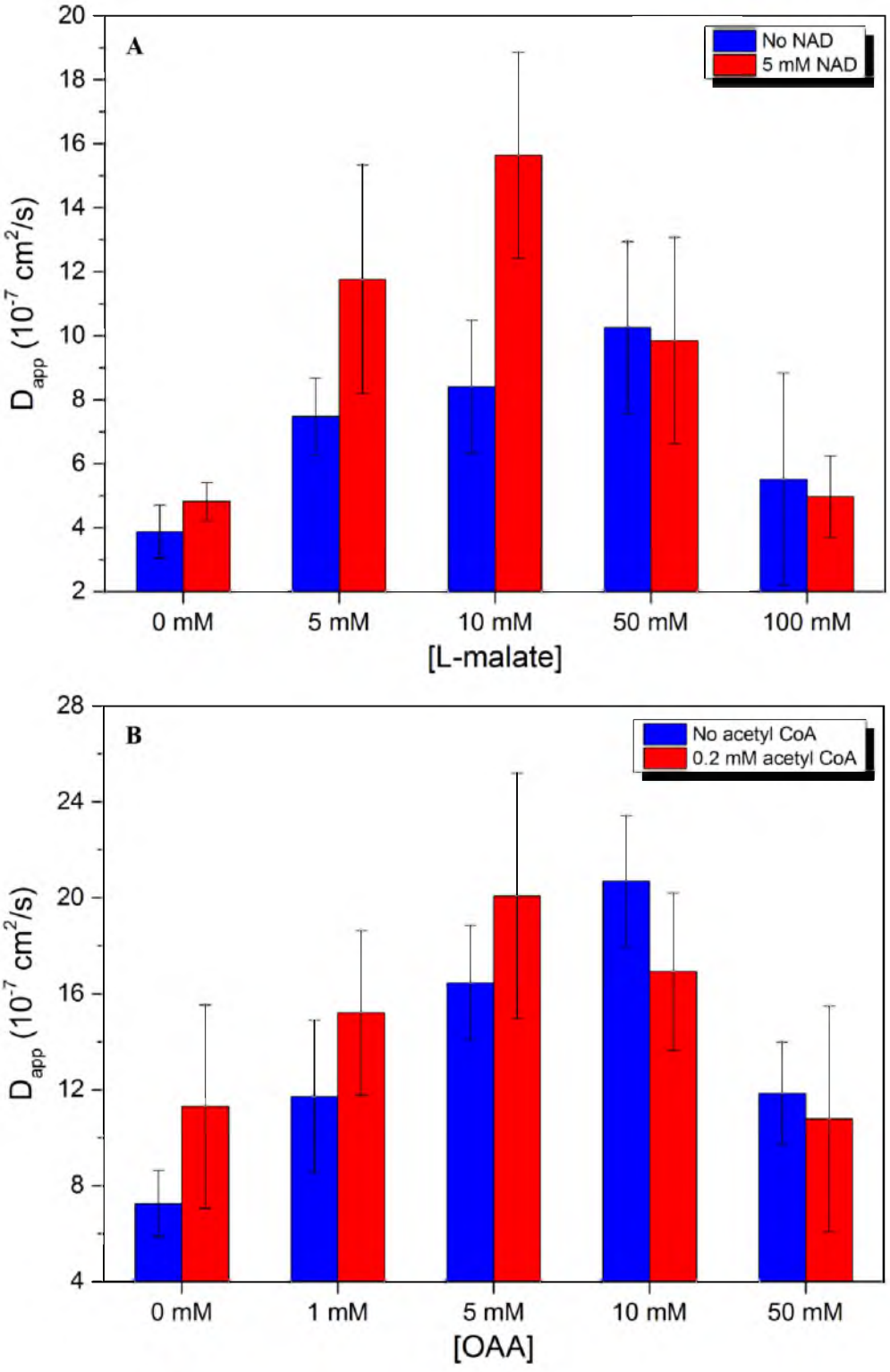

Figure 2.6 Apparent diffusion coefficient of single mMDH (**A**) or CS (**B**) in the presence of increasing substrate concentration with and without cofactors.

μm) against 10 mM L-malate, as compared to a 116% increase in the absence of NAD^+. This significant enhancement was consistent with previously reported related experimental results which concluded that catalysis enhances diffusion coefficient of single enzymes.[7] For CS in the presence of acetyl-CoA, the D_{app} increased by 78% from 1.13×10^{-6} cm^2/s (l = 11.45 μm) against 0 mM OAA to 2.01×10^{-6} cm^2/s (l = 15.27 μm) against 5 mM OAA. As compared to the 127% increase in the absence of acetyl-CoA, however, the enhancement of D_{app} was reduced. This unexpected change may be caused by "prebinding competition to CS" between OAA and acetyl-CoA. As discussed earlier in this chapter, if OAA binds first, a favorable closed form of CS is induced for acetyl-CoA recognition and catalysis ensues. If acetyl-CoA binds first, however, the active sites in CS are completely blocked from further binding to OAA.

Another interesting finding was the lowering of substrate concentration for maximum D_{app} (10 mM L-malate for mMDH and 5 mM OAA for CS) in the presence of cofactors. The reduction of directional enzyme diffusion at high substrate concentration could be explained by competitive binding between substrate and product to the same active site during the catalytic cycle. If the V_{max} is reached quickly, generating a local pool of products, an inhibitory feedback effect might prevent the active sites from binding more substrates. To test whether product concentration would also affect enzyme movement, we studied mMDH diffusion directly against an OAA concentration gradient. As shown in Figure 2.7, the D_{app} of mMDH was again in direct proportion to the concentration of OAA. Its value is comparable to that measured with L-malate, albeit achieved at a much lower OAA concentration. This is likely because the binding affinity of OAA to mMDH and the turnover number of the backward reaction were two orders of magnitude higher (Km was

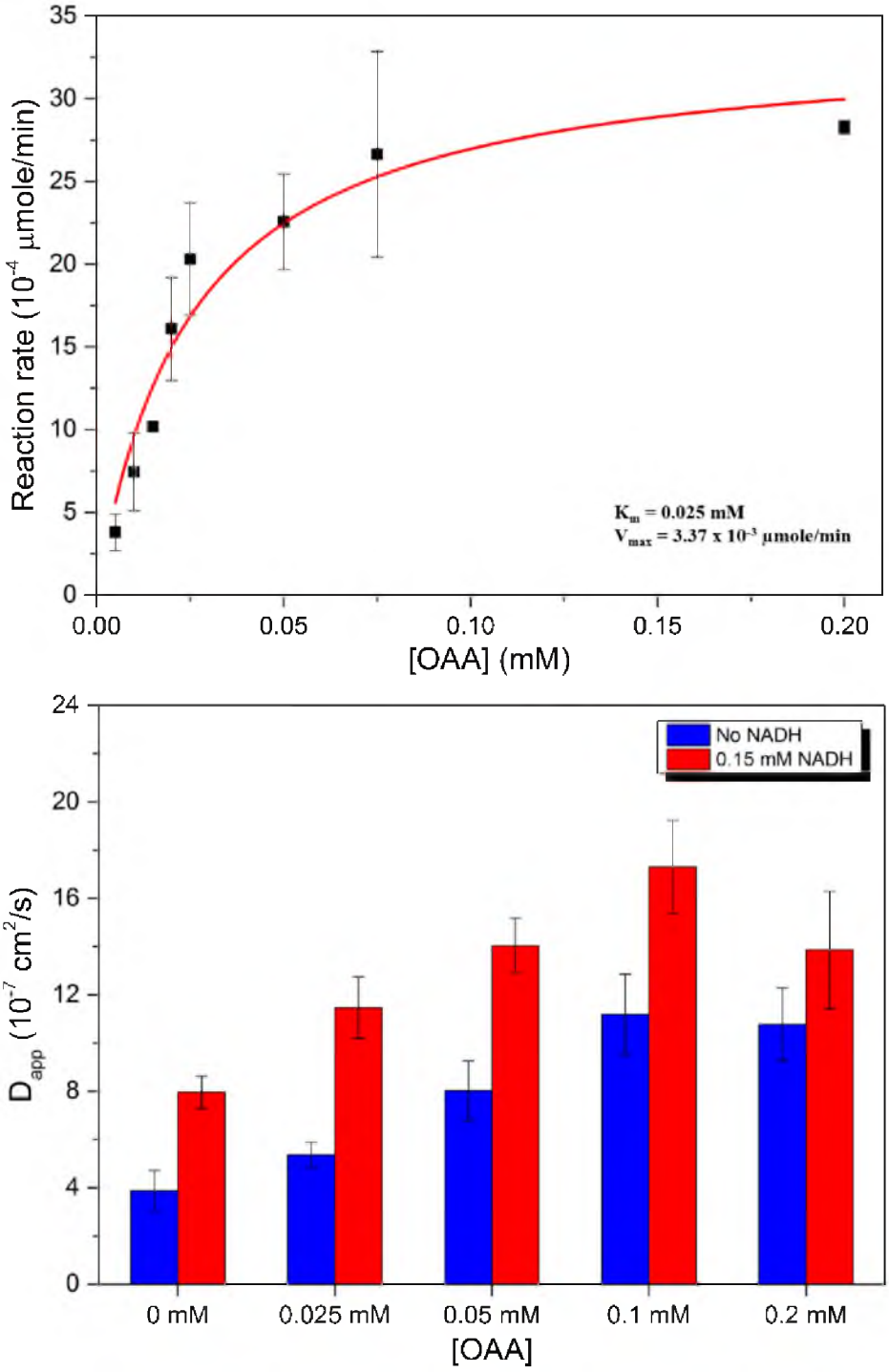

Figure 2.7 Kinetics of mMDH-catalyzed OAA conversion to L-malate (Top) and apparent diffusion coefficient in the presence of increasing [OAA] with and without NADH (Bottom).

0.025 mM and turnover number was 562 s^{-1}).

2.3.4 Co-diffusion of mMDH and CS Enhanced by Intermediate Production

Results on the dynamics of the single enzymes demonstrated the collective directional transport of mMDH or CS stimulated by a metabolite concentration gradient, which encouraged us to continue exploring the potential role of the intermediate in driving co-diffusion of mMDH and CS. As shown in Figure 2.8, when the two enzymes were infused together against L-malate and cofactors, coupled production of citrate from L-malate began at the flow interface. The D_{app} of mMDH increased from 4.9×10^{-7} cm^2/s (l = 7.54 μm) against 0 mM L-malate to a maximum of 1.5×10^{-6} cm^2/s (l = 13.19 μm) against 5 mM L-malate. Meanwhile, an enhancement in CS lateral diffusion occurred with the D_{app} increasing from 8.8×10^{-7} cm^2/s (l = 10.10 μm) to a maximum of 1.9×10^{-6} cm^2/s (l = 14.85 μm). A reduction of D_{app} when [L-malate] was greater than 10 mM could be attributed to allosteric inhibition of mMDH by locally accumulated citrate.

As a control, the same measurement in the absence of cofactors was performed to test if coupled catalysis is necessary for enhanced co-diffusion. As shown in Figure 2.9, however, even without the generation of the intermediate (OAA) the D_{app} of both enzymes increased until mMDH was saturated by 10 mM L-malate. By removing mMDH, the D_{app} of CS gradually decreased as [L-malate] increased, suggesting that the observed co-diffusion might be due to another contribution. The most plausible explanation is the intrinsic "linkage" between mMDH and CS. This was supported by blue Native gel electrophoresis, which is a general tool used to detect protein-protein interactions by estimating their molecular weight. In Figure 2.10, an additional band appeared around 248 kDa, which related to the interaction between one mMDH tetramer and one CS dimer (35.9

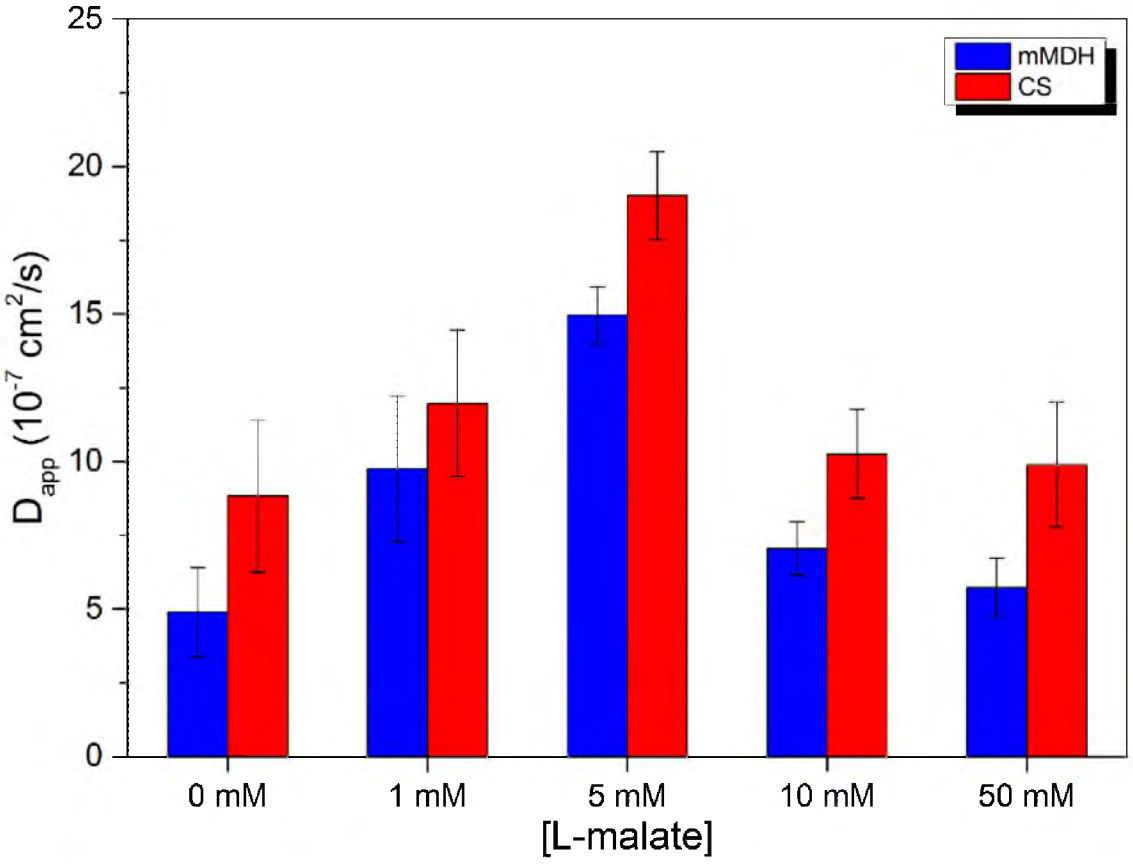

Figure 2.8 Apparent diffusion coefficients of mMDH and CS measured against increasing [L-malate] and 5 mM NAD^+ and 0.2 mM acetyl CoA.

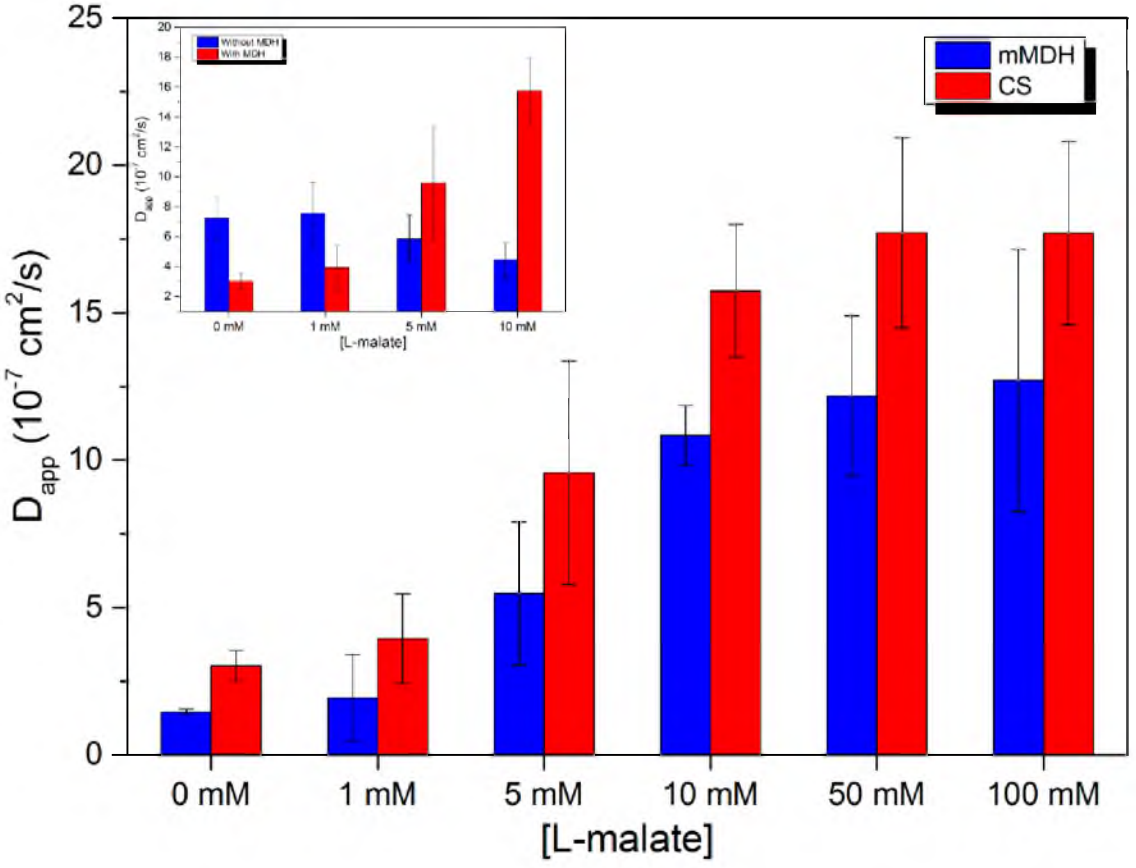

Figre 2.9 Apparent diffusion coefficients of mMDH and CS measured against increasing [L-malate] without cofactors. Inset is the apparent diffusion coefficient of single CS measured against L-malate without cofactors.

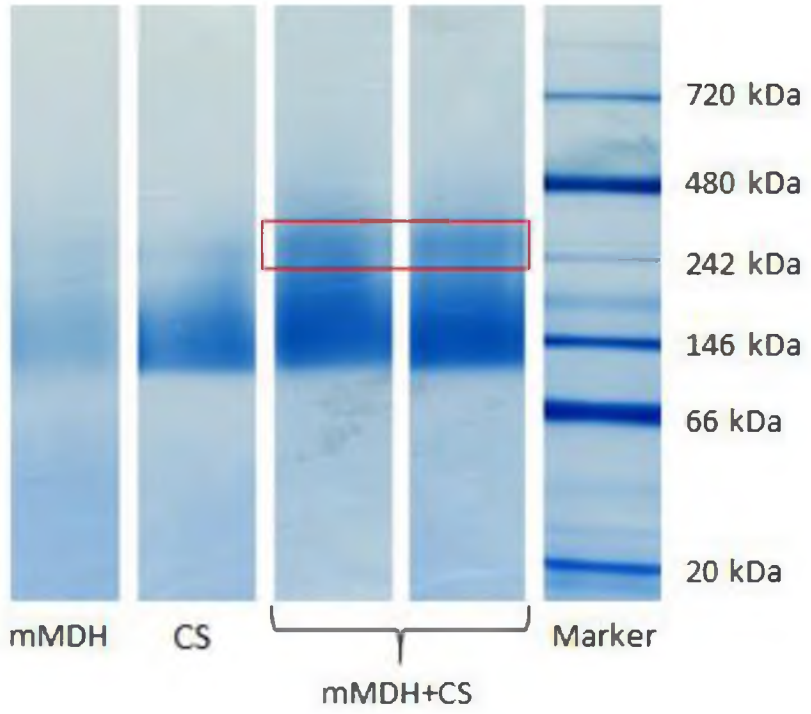

Figure 2.10 Blue Native gel electrophoresis of individual mMDH, CS and mixture of mMDH and CS. Enzyme concentration was kept at 100 nm.

kDa × 4 + 52 kDa × 2 = 247.6 kDa). This seemed contradictory towards the common idea that protein-protein interactions or metabolon formation is favored under very concentrated states (hundreds of micromolar concentrations), while the protein concentration in our experiment was kept at only 100 nM. Additionally, these results also surprisingly revealed mMDH to be in its tetrameric form (band at around 146 kDa). As a result, the D_{app} of mMDH measured throughout the experiments was always smaller than the D_{app} of CS. This can only be explained by tetramerization of mMDH in solution, otherwise the D_{app} of the mMDH dimer should be larger based on their relative sizes (Stokes-Einstein equation).

Herein we hypothesized that it was not a strong physical interaction but rather a dynamic (probably electrostatic) association that facilitated the co-diffusion of CS with mMDH. To verify this theory, we infused mMDH and CS separately in two flows. As shown in Figure 2.11, CS exhibited a weak affinity to mMDH, which gave a slight increase (16%) in D_{app} from 7.2×10^{-7} cm^2/s (l = 9.14 μm) to 8.4×10^{-7} cm^2/s (l = 9.88 μm). Following the addition of L-malate and cofactors to initiate OAA production, CS diffused toward mMDH faster with its D_{app} increasing by 33% (10 mM), 55% (50 mM) and 75% (100 mM). Therefore, this indicates that intrinsic mMDH-CS attraction had a minor effect on co-diffusion. Generation of intermediate between separated mMDH and CS would significantly decrease their proximity, even though the resultant association is dynamic and reversible.

2.3.5 Mechanism for Intermediate Gradient-Induced Co-diffusion

Studies on self-propulsion at the nanoscale indicated several mechanisms that could potentially drive the chemotaxis-like behavior of enzymes. A gradient created across the interfacial region of an enzyme (treated as a nanosphere) can cause displacement of the

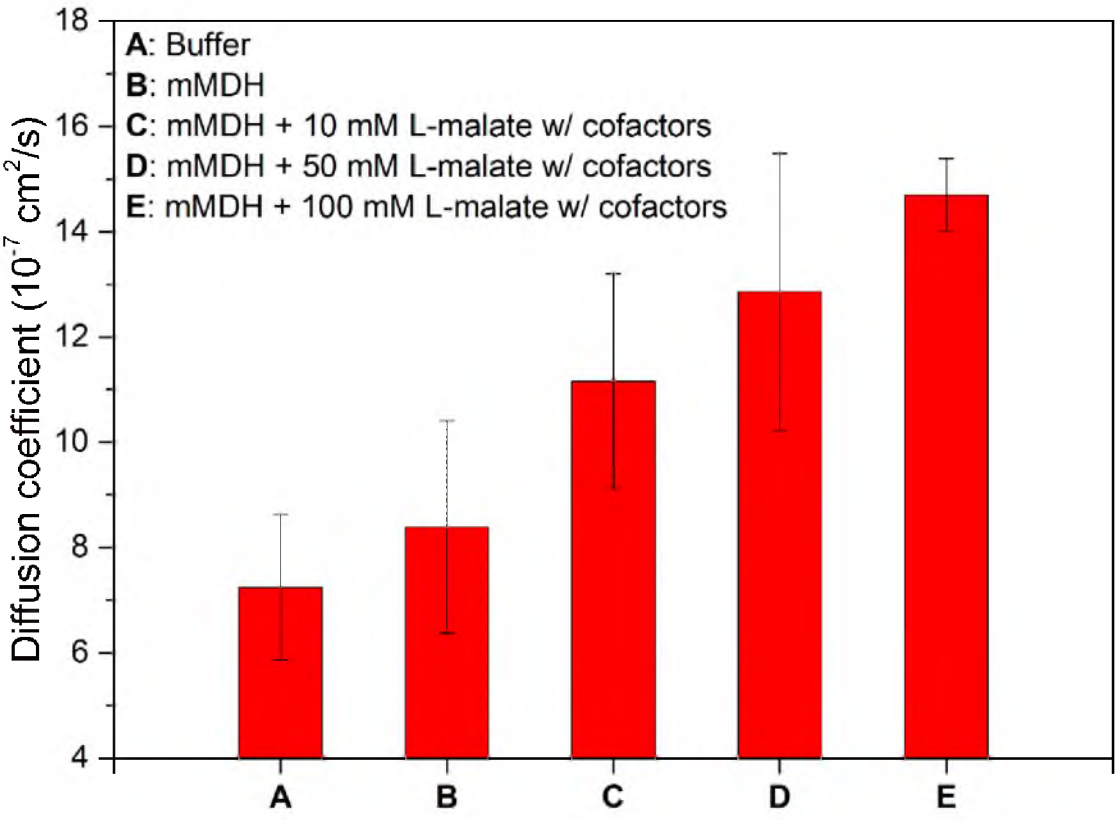

Figure 2.11 Apparent diffusion coefficient of CS measured against mMDH and L-malate with cofactors on the other side of channel.

enzyme in the opposite direction to the molecular flux down the gradient. Depending on whether it is a concentration gradient or an electric field, this phoretic flow is termed diffusiophoresis or electrophoresis. If the gradient is generated locally by the enzyme itself, *i.e.* a pool of charged product near its surface, the enzyme sphere may "swim" against the local gradient like a Brownian ratchet. According to Brownian simulation, self-diffusiophoresis or self-electrophoresis can increase the diffusion rate by up to fifty times.[32] This theory appears to explain observed augmentation in the D_{app} of mMDH and CS. However, it does not explain the plateau in diffusion rate following saturation of the substrate. One possible reason is the decreased diffusion coefficient in high viscosity associated with high sugar content. This has been proven by control experiments. By using unrelated enzymes (α-ketoglutarate dehydrogenase (αKGDH) and alcohol dehydrogenase (ADH)) or substrate (fumarate, another TCA cycle metabolite that is structurally similar to L-malate), we demonstrated that the D_{app} decreased with increasing metabolite concentration (Figure 2.12).

Although the physics for directed enzyme transport induced by a substrate concentration gradient remains to be fully established, conformational transition upon ligand binding is accepted as playing an important role in altering the enzyme motion. Therefore, as we observed, the change of D_{app} tended to follow specific substrate-active site binding equilibria and enzyme kinetics. Binding of NAD^+ and L-malate to mMDH occurs in an ordered manner with a conformational change around active sites upon the formation of the mMDH-NAD+-L-malate complex. For CS, binding of OAA can directly induce domain movement and internal rearrangement of amino acid side chains. "Conformation oscillation" between free and bound states would at least enhance the

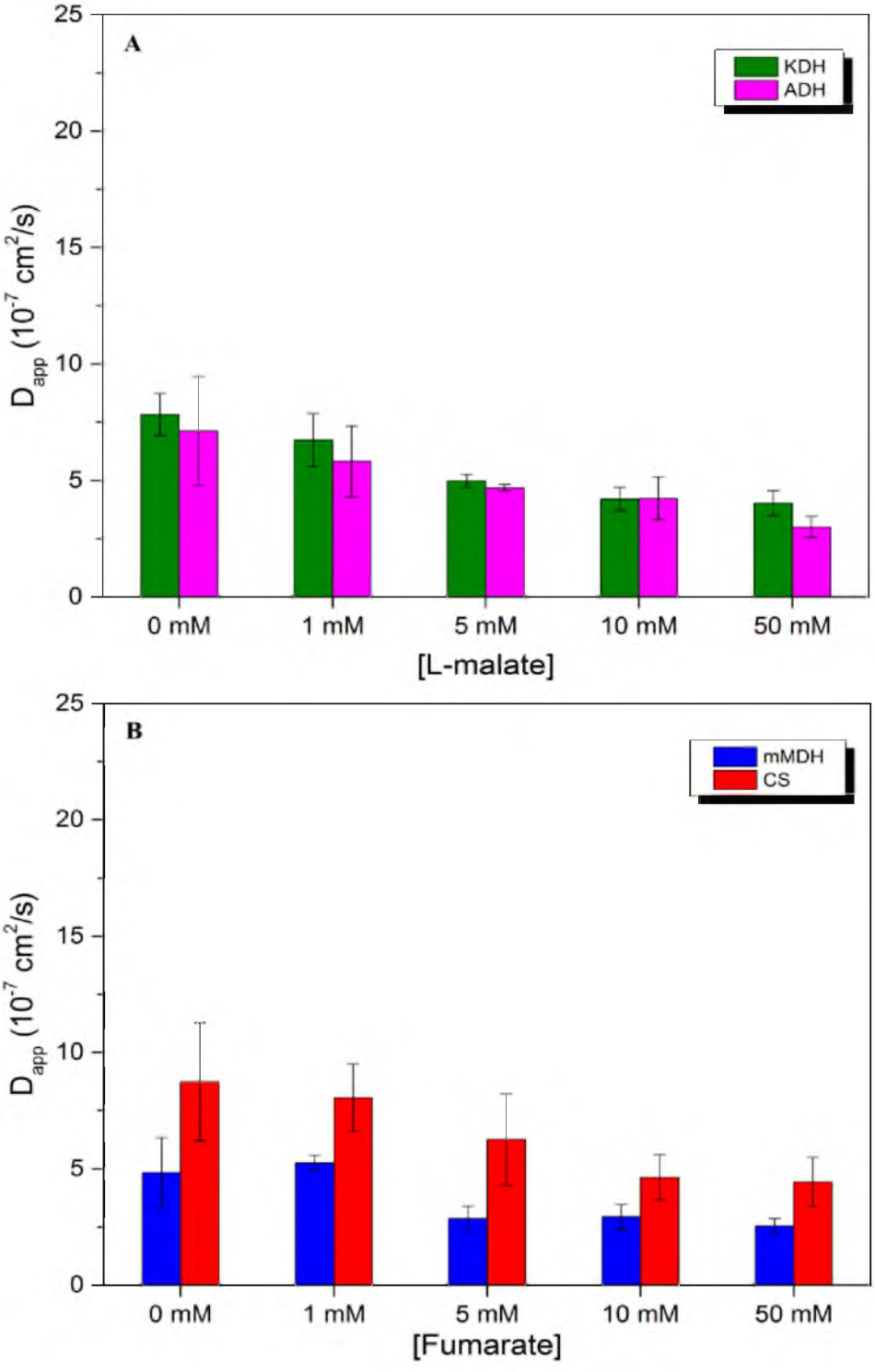

Figure 2.12 Apparent diffusion coefficient of (**A**) αKGDH and ADH measured against L-malate with 5 mM NAD^+, and (**B**) mMDH and CS measured against fumarate with 5 mM NAD^+ and 0.2 mM acetyl CoA.

rotational diffusion of enzyme molecules, particularly when enzymes are relatively large (over 100 kDa). Hence, with more ligands present, more binding events would occur to enhance the enzyme flux into an even higher concentration region, similarly as the Brownian ratchet driven by self-phoresis, until all available binding sites are occupied.

Work on DNA polymerase complexes performed by Sengupta *et al.* showed that cycles of non-reciprocal conformational alterations can increase its diffusion coefficient by almost 40%. In this work, individual lateral diffusion and co-diffusion were both significantly accelerated by catalysis.[9] Through the complete catalytic cycle, conformation transition is accelerated by substrate turnover and product release, resulting in a greater acceleration factor on enzyme diffusion against a concentration gradient. It worth mentioning that the energy conversion during a catalytic turnover is not negligible in changing the enzyme diffusivity. As suggested by the latest work done by Riedel *et al.*, heat released by enzymatic reactions may place a chemoacoustic effect that results in a center-of-mass acceleration of the enzymes.[33]

By interrupting the catalytic cycle with a competitive inhibitor (ATP), we were able to observe a consequent reduction in lateral diffusion. As shown in Figure 2.13, the D_{app} of mMDH decreased consistently with the reaction rate as [ATP] increased. Such attenuation became less significant after 50% of mMDH molecules were inhibited. Similar results were obtained in the case of coupled reactions (Figure 2.14). Adding ATP into the channel led to a reduction of directional transport for both enzymes. It should be noted that the D_{app} of mMDH measured with cofactors and ATP (7.83×10^{-7} cm^2/s) against 0 mM L-malate was 0.5% larger than that measured with just cofactors (4.90×10^{-7} cm^2/s), and four times higher than that measured against buffer (1.46×10^{-7} cm^2/s), indicating that not only

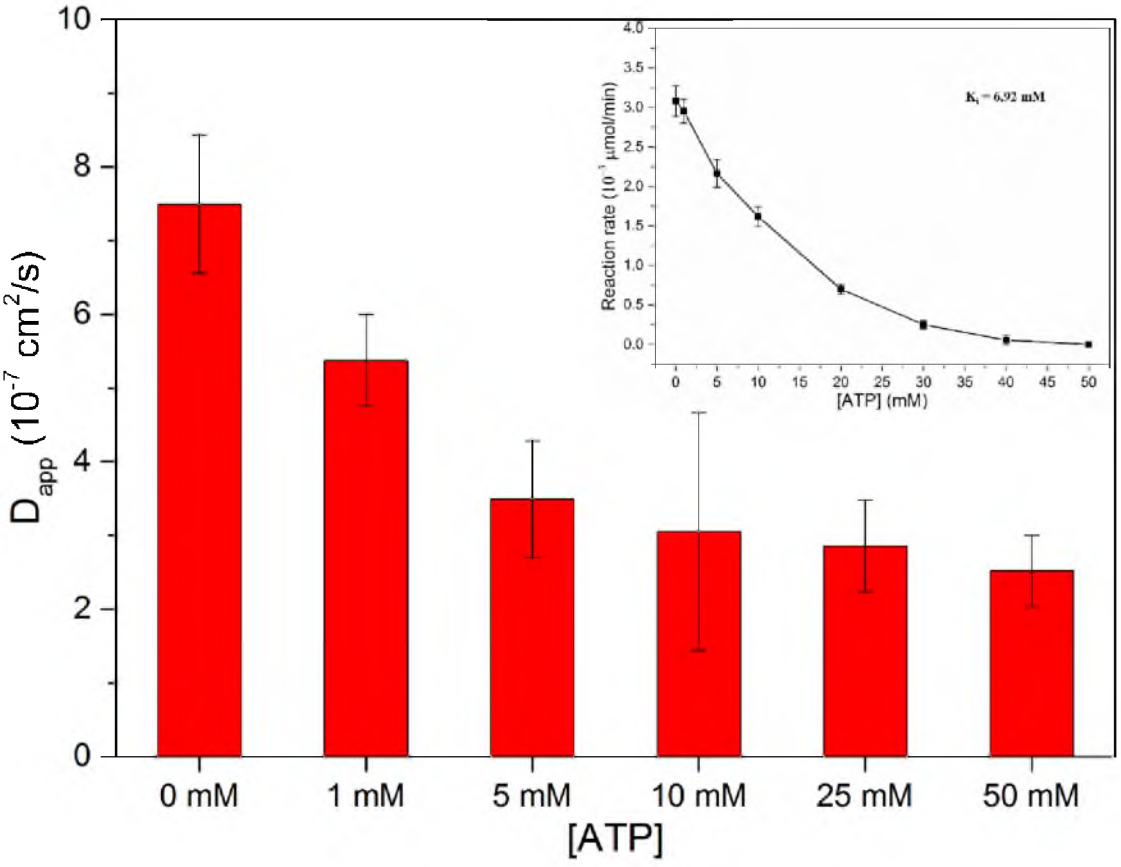

Figure 2.13 Apparent diffusion coefficient of single mMDH measured with 5 mM L-malate and 1 mM NAD^+ in the presence of increasing [ATP] equalized on both sides of channel. Inset is the reaction rate of mMDH-catalyzed L-malate conversion under same condition.

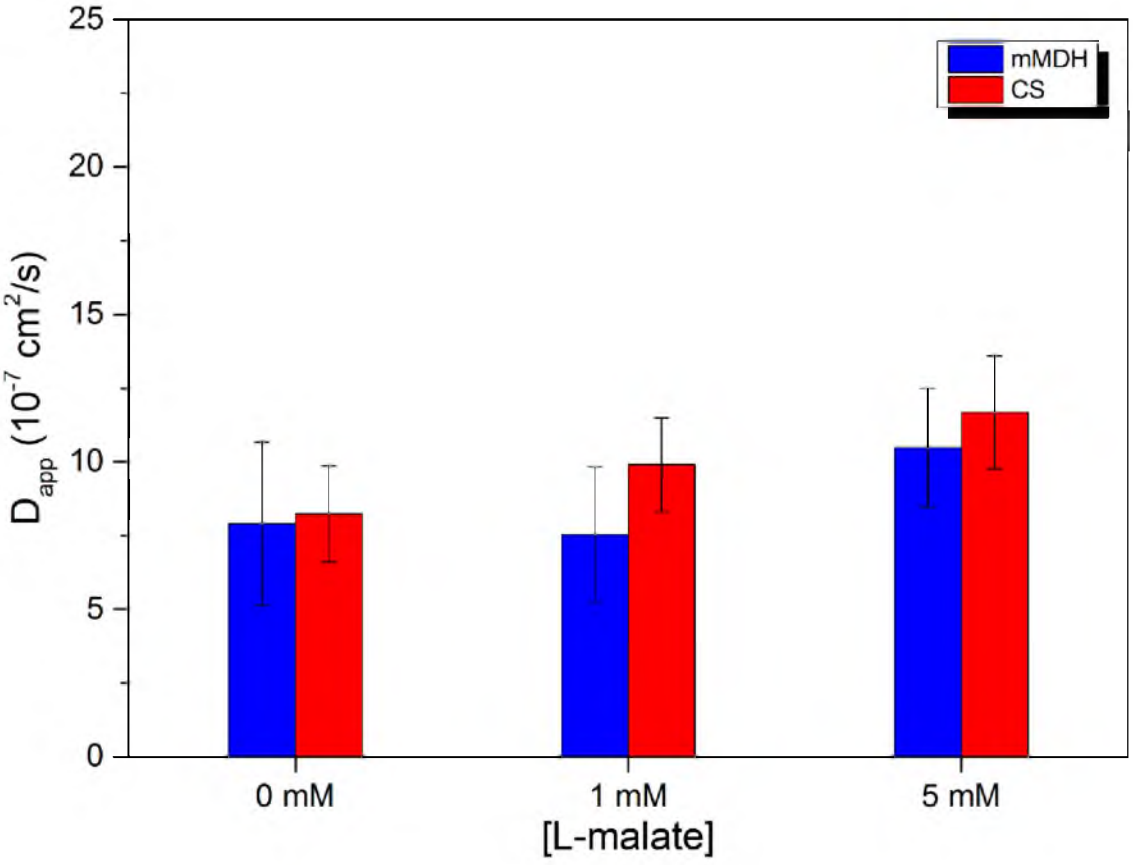

Figure 2.14 Apparent diffusion coefficients of mMDH and CS measured with L-malate, 1 mM NAD^+ and 0.2 mM acetyl CoA in the presence of 25 mM ATP equalized on both sides of channel.

substrate but also other ligands can alter enzyme diffusivity. Continued additions of L-malate in the presence of 25 mM ATP, however, did not further enhance D_{app}, since competitive binding of ATP to the nicotinamide binding site cannot induce favorable conformational changes for L-malate accommodation. Within mitochondria, where many metabolites are present, the concentration-mediated regulatory effect on enzyme motion and dynamic association will be more complex.

2.4 Conclusions

In this study, the directional transport of mMDH and CS against the concentration gradient in a microfluidic channel has been observed. Such chemotaxis-like motion can be promoted by catalysis and suppressed by inhibitors. Upon extension to a coupled enzyme system, the directional co-diffusion of both enzymes can be accelerated by sequential catalysis, demonstrating that local intermediate concentration gradients will enhance the dynamic association between mMDH and CS at very low protein concentrations. In the realm of bioelectrocatalysis, metabolons have become a hot spot for researchers seeking improved mass transport. Work described in this chapter is aimed at gaining physical insight into enzyme behavior affected by metabolite concentration and will help understand the dynamics of metabolon formation. This will also provide a new perspective toward artificial metabolons, since sequential enzymes may be functionally associated by their intermediates.

2.5 References

(1) Bard, A. J.; Faulkner, L. R. *Electrochemical Methods: Fundamentals and Applications*; 2nd ed.; John Wiley & Sons, Inc.: New York, **2001**.

(2) Oaks, A.; Bidwell, R. G. S. *Annue. Rev. Plant. Physiol.* **1970**, *21*, 43.

(3) Saks, V.; Beraud, N.; Wallimann, T. *Int. J. Mol. Sci.* **2008**, *9*, 751.

(4) Bray, D.; Levin, M. D.; Morton-Fifth, C. J. *Nature* **1998**, *393*, 85.

(5) Norris, V.; Gascuel, P.; Guespin-Michel, J.; Ripoll, C.; Saier Jr, M. H. *Mol. Microbiol.* **1999**, *31*, 1592.

(6) Bartholomae, M.; Meyer, F. M.; Commichau, F. M.; Burkovski, A.; Hillen, W.; Seidel, G. *FEBS J.* **2014**, *281*, 1132.

(7) Muddana, H. S.; Sengupta, S.; Mallouk, T. E.; Sen, A.; Butler, P. J. *J. Am. Chem. Soc.* **2010**, *132*, 2110.

(8) Sengupta, S.; Dey, K. K.; Muddana, H. S.; Tabouillot, T.; Ibele, M. E.; Butler, P. J.; Sen, A. *J. Am. Chem. Soc.* **2013**, *135*, 1406.

(9) Sengupta, S.; Spiering, M. M.; Dey, K. K.; Duan, W.; Patra, D.; Butler, P. J.; Astumian, R. D.; Benkovic, S. J.; Sen, A. *ACS Nano* **2014**, *8*, 2410.

(10) Frieden, C.; Honnegger, J.; Gilbert, H. R. *J. Biol. Chem.* **1978**, *253*, 816.

(11) Hsu, W.-C.; Hung, H.-C.; Tong, L.; Chang, G.-G. *Biochemistry* **2004**, *43*, 7382.

(12) Hall, M. D.; Levitt, D. G.; Banaszak, L. J. *J. Mol. Biol.* **1992**, *226*, 867.

(13) Minarik, P.; Tomaskova, N.; Kollarova, M.; Antalik, M. *Gen. Physiol. Biophys.* **2002**, *21*, 257.

(14) Silverstein, E.; Sulebele, G. *Biochemistry* **1969**, *8*, 2543.

(15) Goward, C. R.; Nicholls, D. J. *Protein Sci.* **1994**, *3*, 1883.

(16) Lamzin, V. S.; Dauter, Z.; Wilson, K. S. *Nat. Struct. Biol.* **1994**, *1*, 281.

(17) Nicholls, D. J.; Miller, J.; Scawen, M. D.; Clarke, A. R.; Holbrook, J. J.; Atkinson, T.; Goward, C. R. *Biochem. Biophys. Res. Commun.* **1992**, *189*, 1057.

(18) Bohinski, R. C. In *Modern Concepts in Biochemistry*; 5th ed.; Allyn and Bacon, Inc.: Newton, **1987**, p 540.

(19) Bernstein, L. H.; Grisham, M. B.; Cole, K. D.; Everse, J. *J. Biol. Chem.* **1978**, *253*, 8697.

(20) Gelpi, J. L.; Dordal, A.; Monsterrat, J.; Mazo, A.; Cortes, A. *Biochem. J.* **1992**, *283*, 289.

(21) Bloxham, D. P.; Parmelee, D. C.; Kumar, S.; Wade, R. D.; Ericsson, L. H.; Neurath, H.; Walsh, K. A.; Titani, K. *Proc. Natl. Acad. Sci. U. S. A.* **1981**, *78*, 5381.

(22) Johansson, C.-J.; Petterson, G. *Eur. J. Biochem.* **1974**, *42*, 383.

(23) Johansson, C.-J.; Petterson, G. *Biochim. Biophys. Acta* **1977**, *484*, 208.

(24) Wiegand, G.; Remington, S. J. *Ann. Rev. Biophys. Chem.* **1986**, *15*, 97.

(25) Remington, S.; Wiegand, G.; Huber, R. *J. Mol. Biol.* **1982**, *158*, 111.

(26) Lesk, A. M.; Chothia, C. *J. Mol. Biol.* **1984**, *174*, 175.

(27) Xia, Y.; Whitesides, G. M. *Annu. Rev. Mater. Sci.* **1998**, *28*, 153.

(28) Mukherjee, A.; Smitherman, T. C.; Robinson, J. B. J.; Butsch, R. W.; Richards, E. G.; Srere, P. A. *Adv. Myocardiol.* **1980**, *1*, 329.

(29) Bergmyer, H. U. *Methods of Enzymatic Analysis*; 2nd ed.; Academic Press: New York, **1974**.

(30) Eanes, R. Z.; Kun, E. *Biochim. Biophys. Acta* **1971**, *227*, 204.

(31) Kurz, L. C.; Shah, S.; Crane, B. R.; Donald, L. J.; Duckworth, H. W.; Drysdale, G. R. *Biochemistry* **1992**, *31*, 7899.

(32) Ebbens, S. J.; Howse, J. R. *Soft Matter* **2010**, *6*, 726.

(33) Riedel, C., Gabizon, R., Wilson, C. A. M., Hamadani, K., Tsekouras, K., Marqusee, S., Pressé, S., Bustamante, C. *Nature* **2015**, *517*, 227.

CHAPTER 3

STRUCTURAL PROBING OF PROTEIN-PROTEIN INTERACTIONS AND SUBSTRATE CHANNELING IN THE TCA CYCLE METABOLON BY CROSS-LINKING AND MASS SPECTROMETRY

3.1 Background Introduction

3.1.1 Principles of Protein-Protein Interactions

Protein-protein interactions (PPIs) have important implications in elucidating intracellular organization of metabolic functions on the molecular point of view. In dilute solutions, PPIs undergo a diffusion-controlled process. It may require a long time for protein molecules diffusing translationally before they collide. Once encountered, they explore each other's surface and rotate locally to adopt an optimal conformation orientation. In the translational step, diffusion rate can be greatly affected by external factors including medium viscosity, pH, temperature and ionic strength.[1] Adding crowding agents, such as PEG, which simulates the crowded intracellular environment, can enhance protein-protein association rate by volume-excluding effect.[2] In the rotational step, geometric constraints and specific residue interactions dominate the conformation adoption.[1]

Proteins interact through recognition between surface hot spots, which are highly conserved residues during evolution. Site-directed mutation of these sites will cause an

Reprinted from "Wu, F., Minteer, S. D. *Angew. Chem. Int. Ed.* **2015**, *54*, 1851" with permission from John Wiley & Sons, Inc.

increase of binding free energy by at least 2.0 kcal/mol and thus dissociation of protein complexes. Interfaces between binding partners have been shown to possess good surface shape and electrostatic complementarity, and typically have an area of 1200 ~ 2000 Å.[2,3-5] Hydrophobic interactions turn out to be the major driving force as a large extent of nonpolar regions are buried in interfaces. This in fact thermodynamically stabilizes associated proteins due to water molecule expulsion and entropy increase.[6,7] Meanwhile, the population of charged and polar residues are also found significant at interfaces, indicating a central role of electrostatic interactions in PPIs. Electric fields generated at the protein surface enhances the rotational diffusion at binding sites until the interfacial electrostatic complementarity is attained. Another noteworthy consequence is the surface charge rearrangement at non-buried areas that ultimately facilitates electrostatic channeling of substrate between enzyme active sites.[8] In addition to hydrophobic and electrostatic interactions, amino acid side chains at interfaces form hydrogen bonds that also stabilize protein-protein association.[3]

3.1.2 Chemical Cross-Linking of Protein-Protein Interactions

Chemical cross-linking can be classified into *in vivo* and *in vitro* cross-linking. When applied *in vivo*, cross-linking reagents (cross-linkers) quickly capture obligatory or transient interactions, and stabilize protein complexes in native state. This method requires lipophilic cross-linkers that can penetrate the membrane. *In vitro* chemical cross-linking is usually done in solution by simply mixing cross-linkers with isolated/purified interacting proteins. Most cross-linkers are small bifunctional molecules with a spacer arm of several Angstroms. The distinct advantage is the capability of probing interfacial amino acids

within a restricted distance in combination with other follow-up detection techniques, i.e. mass spectrometry.

The principle of chemical cross-linking is covalent conjugation of the functional groups of a cross-linker to specific surface amino acids on interacting domains. Lysines are the most frequently targeted residues because of their relatively high prevalence (6%) and reactivity (primary amine). Lysine-specific cross-linking is beneficial for producing stable native complexes at relatively high yields as long as the reaction conditions are carefully controlled, although it sometimes cannot distinguish desired PPIs from random artifacts. Other residues like cysteines and arginines can be targeted, however, they often suffer from low abundance, inefficient cross-linking, or unfavorable reaction conditions for native proteins.[9]

In this work, disuccinimidyl glutarate (DSG, structure shown below) is utilized to cross-link lysines on two interacting domains. DSG belongs to the family of amine-reactive N-hydroxysuccinimidyl esters. It can form two amide bonds with the primary amines of lysines and link them through a three-carbon spacer, which is 7.7 Å in length. Since it is membrane-permeable, DSG is used for *in vivo* cross-linking of the TCA cycle metabolon.

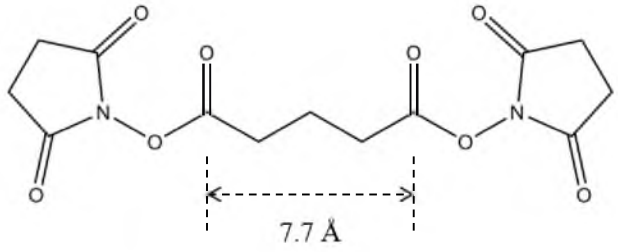

DSG

3.1.3 Separation of Cross-linked Protein Complexes

Containing nearly 10% of the cell protein amount, mitochondria can be isolated from bulk cytoplasm by differential centrifugation with their intact matrix organization protected by two double-layer membranes (outer mitochondrial membrane and inner mitochondrial membrane).[10] *In vivo* cross-linking will generate a complex pool of fixed protein complexes of different sizes (molecular weight) packed tightly by the membranes. Before any further proteomic analysis, membrane disruption is needed. To break the membrane boundary, two common tools have been adopted: detergents and ultrasonication. Detergents are amphiphilic molecules bearing a polar head and a nonpolar tail, meaning that they can intervene between lipid molecules and membrane proteins. Beyond the critical micelle concentration (CMC), detergents start forming micelles that rupture the bilayer structure. Ultrasonication uses high-energy sound waves to break the bilayer or large lipid fractions into small pieces.

Once the membrane and matrix proteins are released, sodium dodecyl sulfate polyacrylamide gel electrophoresis (SDS-PAGE) isolates the protein complex of interest (the TCA cycle metabolon in this work) by sizes. SDS is also a surfactant whose hydrophobic tail can interact strongly with the protein backbone and destroy the tertiary structure (denaturing). Since that the binding occurs at a constant ratio of one SDS molecule to two amino acids, proteins acquire predictable number of negative charges on a peptide length or weight basis. In an external electric field, these negatively charged proteins will migrate through the chemically inert polyacrylamide mesh. For proteins with shorter chains and higher mass-to-charge ratios (m/z), they migrate faster than those with longer chains and lower m/z. When the migration is conducted in a gradient

polyacrylamide gel which contains pores of decreasing sizes, small proteins with high mobility can migrate over a longer distance, whereas large protein complexes with reduced mobility will get stuck somewhere near the starting line. After electrophoresis, trapped proteins are visualized by various dyes (i.e. Coomassie, silver, fluorophores, etc.) and compared to standard markers of known molecular masses.[11]

3.1.4 Protein Digestion

In studying PPIs, researchers often intend to know the particular interacting residues or peptides. For this purpose, intact protein complexes are digested by trypsin into small fragments to distinguish conjugated peptides from native peptides. Trypsin is an endopeptidase that only cuts peptide bonds at C-terminal of arginine (R) or lysine (K). Typsin digestion is very specific and efficient in generating peptide fragments from denatured or native proteins for mass spectrometric analysis. There are several scenarios in which trypsin may fail: (1) two cleavable peptide bonds in consecutive positions (RR, RK, KR, or KK) which only lets trypsin cut one of them, (2) posttranslationally or manually modified R or K, and (3) R or K with a proline (P) on its C-terminal side. As a result, proteins are degraded into peptides bearing at least one R or K at C-terminus. In principle, they are 10 amino acids long on average, but in practice, the length spans a wide range. Nonetheless, peptides of 4~40 amino acids are usually taken for analysis.[11,12]

3.1.5 Mass Spectrometric Analysis of Peptides

Mass spectrometry is aimed at identifying charged species by their m/z and abundance. A bottom-up approach for mass spectrometric studies of PPIs includes separation of a mixture of tryptic peptides by high-performance liquid chromatography (commonly reversed-phase chromatography), ionization of tryptic peptides by energy

sudden ion generation or rapid desorption, analyzing of charged peptides passing through an electric or magnetic field, and detection of ion beams which are converted into readable spectra with m/z (unit: Th) peaks.[13] Identification of a peptide-generated peak on a high-resolution mass spectrum is accomplished with its characteristic isotopic pattern, which is the separation of isotopic peaks by charge. In spectra of small ions or short peptide fragments, the strongest peak is always monoisotopic (first peak of an isotopic pattern), which refers to a composition of only most abundant natural isotopes (^{12}C, ^{1}H, ^{16}O, ^{14}N, ^{32}S, etc.), but as carbon number increases in longer peptides or proteins, chances of having one or more ^{13}C also increases, indicated by rising of the subsequent isotopic peaks. For tryptic peptides of 1500 ~ 2000 Da, the isotope containing one ^{13}C becomes the strongest. For peptides of 2000 ~ 3000 Da, the isotope containing two ^{13}C is the highest, and so forth. The isotopic pattern will eventually become bell-shaped as peptide mass increases.[14]

To determine the accurate molecular mass (M) of a peptide carrying *n* charges from mass spectrometric data, one may first identify the monoisotopic peak at m_1, even though it is challenging when mass is huge. In the positive mode (peptide in form of $[M + nH]^{n+}$), *n* is easily judged by the separation of the monoisotopic peak and second isotopic peak at m_2 (or of any two neighboring peaks in the isotopic pattern):

$$n = 1/(m_2\text{-}m_1)$$

Then M is derived by

$$M = n(m_1\text{-}1.0078)$$

The mass error is defined as the difference between experimentally measured mass (M_{expt}) and calculated exact mass (M_{calc}) in parts per million (ppm)[11]

$$\frac{M_{expt}\text{-}M_{calc}}{M_{calc}} \times 10^6 \text{ ppm}$$

3.1.6 Aims

Although extensive efforts have been made in assembling enzyme cascades (including the TCA cycle) into metabolon biomimics[15], there is limited knowledge of how these enzymes interact with each other in natural metabolons. Combining protein engineering and computer modeling, Srere *et al.* proposed a symmetric model for the mMDH-CS-ACO complex as a part of the TCA cycle metabolon. To construct this model, they set the homodimer, CS as the core of the complex, whose C-terminus were fused to N-terminus of mMDH (also a homodimer), and N-terminus were respectively fused to C-terminus of two ACO monomers. With this intelligent structure, they managed to illustrate a continuous surface region of positive potential that may direct efficient substrate channeling by numerical simulation.[16,17] However, organization of wild-type TCA cycle enzymes inside mitochondria is still in need of experimental proof. As claimed in Chapter 1, acquiring native structural information will undoubtedly promote rational design of artificial metabolons. Taking great advantage of mass spectrometry in proteomic studies, researchers now can probe the native structure of *in vivo* protein-protein networks, for which high-resolution techniques like X-ray crystallography are not feasible.[12,18,19] In this work, *in-vivo* chemical cross-linking and mass spectrometry (XL-MS) were combined to identify interfacial residues in mMDH-CS-ACO complex. With distance constraints from XL-MS experiments, a low-resolution structure for mMDH-CS-ACO complex has been re-established using a hybrid protein docking method.

3.2 Experimental

3.2.1 Materials

All chemicals were purchased from Sigma-Aldrich unless otherwise specified. Fresh beef heart was purchased from a local slaughter house.

3.2.2 Preparation of Intact Beef Heart Mitochondria

Mitochondria were isolated from fresh beef heart cells according to Pallotti's procedure[20] with slight modifications. Beef heart cut into small cubes was blended by a Waring laboratory blender in chilled isolation buffer (0.01 M Tris-HCl buffer, 0.25 M sucrose, 0.2 mM EDTA and 1 μM PMSF, pH 7.8). Meat suspension was centrifuged at 1200 × g for 20 min, and the supernatant (filtered through two layers of cheesecloth) was centrifuged at 26000 × g for 15 min. The pellet was homogenized in isolation buffer using a glass-Teflon homogenizer and centrifuged again at 26000 × g for 15 min. Supernatant was discarded and pellet resuspended in isolation buffer was centrifuged at 12000 × g for 30 min. Mitochondrial pellet was homogenized in 20 mL of 0.01 M phosphate buffer containing 0.25 M sucrose (pH 7.8) and stored in small aliquots at -80 °C before use.

3.2.3 *In Vivo* Cross-linking of the TCA Cycle Metabolon

A mitochondrial aliquot was diluted in 10 mM PBS (pH 7.4) to a final protein concentration of 2 mg/mL. Fresh solution of DSG (Life Technologies), 3.26 mg dissolved in 50 μL of dry DMF, was added to the mitochondrial suspension to a final concentration of 1 mM. The approximate DSG/protein molar ratio was 50:1. As a native control, 50 μL of DMF containing no DSG was also added to a separate mitochondria suspension. Cross-linking was incubated at room temperature for 30 min under gentle shaking and quenched by adding 100 μL of 2 M Tris buffer (pH 8.3).

3.2.4 Isolation of Cross-linked Matrix Protein Complexes

Cross-linked mitochondria were collected from suspensions centrifuged at 26000 × g for 30 min and resuspended in 10 mL of lysis buffer (50 mM Tris, 150 mM NaCl, 2 mM EDTA, 1 mM PMSF, and 0.5% sodium cholate, pH 7.4). Membrane disruption was done by homogenizing mitochondria suspension in a glass-glass homogenizer on ice and incubated at 4 °C for 30 min under gentle shaking. Lysed mitochondria were further sonicated by an ultrasonication probe (FB505, Fisher Scientific) in ice bath for 2 min (5 sec on pulses and 15 sec off pulses). Membrane fractions were centrifuged down at 5000 × g for 30 min. Unwanted large fractions and preaggregated proteins were removed by precipitating with 35% ammonium sulfate at 4 °C for at least 1 h under gentle stirring and centrifugation at 5000 × g for 15 min. Yellowish supernatant was then dialyzed in cellulose ester dialysis membrane (Spectro Por® Biotech) with a molecular mass cutoff at 100 kDa against 2 L of 50 mM Tris-HCl buffer (pH 7.4) at 4 °C overnight, and applied to a prepacked Sephadex™ G-25M column (GE Healthcare) to remove excessive salts and detergents. To separate proteins in dialyzed supernatant, reducing SDS-PAGE was performed on a 4-20% gradient gel (Thermo Scientific) according to the protocol provided by manufacturer.

3.2.5 In Gel Digestion of Protein Complexes

Gel bands of interest were excised and destained twice in 1 mL of 50% methanol with 50 mM ammonium bicarbonate at room temperature under gentle vortexing for 1 h. The gel slices were rehydrated in 1 mL of 50 mM ammonium bicarbonate at room temperature for 30 min, and the gel bands/spots of interest were cut into several pieces. These gel pieces were rehydrated in 1 mL of 100% acetonitrile at room temperature under

gentle shaking for 30 min. Acetonitrile was carefully removed from the gel pieces with a pipette tip prior to trypsin digestion. Ten to twenty microliters of sequence-grade modified trypsin (20 ng/μL, Promega) in 50 mM ammonium bicarbonate was added and incubated with the gel pieces overnight at 37 °C. Digestion was quenched by adding 20 μL of 1% formic acid. Then the solution was allowed to stand, and peptides that dissolved in the 1% formic solution were extracted and collected. Further extraction of peptides from the gel material was performed twice by adding 50% acetonitrile with 1% formic acid and sonicating at 37 °C for 20 min. All these solutions were collected and combined. A final complete dehydration of the gel pieces was accomplished by adding 20 μL of 100% acetonitrile and incubation at 37 °C for 20 min. The combined supernatant solutions of extracted peptides were dried in a vacuum centrifuge (Speed-Vac). The peptides were reconstituted in 100 μL of 5% acetonitrile with 0.1% formic acid for mass spectrometric analysis.

3.2.6 Mass Spectrometric Instrumentation

Peptides were analyzed using a nano-liquid chromatography-tandem mass spectrometry (LC-MS/MS) system comprised of a nano-LC pump (Eksigent) and a LTQ-FT mass spectrometer (ThermoElectron Corporation). The LTQ-FT is a hybrid mass spectrometer with a linear ion trap used typically for MS/MS fragmentation (i.e. peptide sequence) and a Fourier transform ion-cyclotron resonance (FT-ICR) mass spectrometer used for primary accurate mass measurement of peptide ions. The LTQ-FT is equipped with a nanospray ion source (ThermoElectron Corporation). Approximately 5 to 20 femtomoles of tryptic-digested or phosphopeptide-enriched samples were dissolved in 5% acetonitrile with 0.1% formic acid and injected onto a homemade C18 nanobore LC

column for nano-LC-MS/MS. A linear gradient LC profile was used to separate and elute peptides, consisting of 5 to 70% solvent B in 78 min with a flow rate of 350 nL/min (solvent B: 80% acetonitrile with 0.1% formic acid; solvent A: 5% acetonitrile with 0.1% formic acid). The LTQ-FT mass spectrometer was operated in the data-dependent acquisition mode controlled by *Xcalibur 1.4* software, in which the "top 10" most intense peaks observed in an FT primary scan (i.e. MS survey spectrum) were determined by the computer on-the-fly and each peak was subsequently trapped for MS/MS analysis and peptide fragmentation (sequencing by collision-induced dissociation). Spectra in the FT-ICR were acquired from m/z 400 to 1700 at 50000 resolving power with about 3 ppm mass accuracy. The LTQ linear ion trap was operated with the following parameters: (1) precursor activation time was 30 ms and activation Q was 0.25; (2) collision energy was set at 35%; (3) dynamic exclusion width was set at low mass of 0.1 Da with one repeat count and duration of 10 s.

3.2.7 Mascot Database Searches

LTQ-FT MS raw data files were processed to peak lists with *BioworksBrowser 3.2* software (ThermoElectron Corporation). Processing parameters used to generate peak lists were as followed: (1) precursor mass was between 401 ~ 5500 Da; (2) grouping was enabled to allow five intermediate MS/MS scans; (3) precursor mass tolerance was set at 5 ppm; (4) minimum ion count in MS/MS was set to 15, and minimum group count was set to 1. Resulting DTA files from each data acquisition were merged and searched against the NCBI or custom databases for identified proteins, using *MASCOT* search engine (Matrix Science Ltd; version 2.2.1; in-house licensed). Searches were done with tryptic specificity, allowing two missed cleavages or "nonspecific cleavage" and a mass error

tolerance of 5 ppm in MS spectra (i.e. FT-ICR data) and 0.5 Da for MS/MS ions (i.e. LTQ Linear ion trap). Identified peptides were generally accepted only when the *MASCOT* ion score value exceeded 20.

3.2.8 Identification of Cross-linked Peptides

Mass spectrometric raw files were analyzed in *Thermo Xcalibur* software and peptide peaks of interest were picked manually. Mass lists were screened using *FindPept* tool (http://web.expasy.org/findpept/) against enzyme sequences obtained from UniProtKB/Swiss-Prot (mMDH: Q32LG3; CS: Q29RK1; ACO: P20004) to identify non-cross-linked peptides (mass error = 6 ppm). A theoretical mass database of potential inter-protein cross-links was built up using a spreadsheet by combining two peptides, which were identified in native individual enzymes but missed in the cross-linked enzyme complex. Additional peptide peaks only found in cross-linked spectra were screened against the mass database. Cross-link candidates were selected by the following rules: (1) trypsin did not cut at the C-terminus of modified lysines or lysines with proline on the C-terminus; (2) up to two missed cleavages were allowed, but nonspecific cuttings were not considered; (3) peptide length was 3 ~ 30 amino acids; (4) each cross-linked peptide had at least two lysines (one for cross-linking and one at C-terminal); (5) peaks showed up in at least duplicate experiments; (6) mass error = 20 ppm. Throughout the whole search process, custom-specified modifications were applied and the respective mass variations (to residues) were summarized in Table 3.1.

3.2.9 Hybrid Protein Docking

As illustrated in Figure 3.1, global docking and local docking were carried out to solve the structure of the mMDH-CS-ACO complex. In global docking, an automated

Table 3.1 Custom-specific modifications for cross-link identification.

Modification	**Residue**	**Mass variation (Da)**
Acetylation	Lysine	+ 42.011
Oxidation	Methionine Tryptophan	+ 15.995
Trimethylation	Lysine	+ 42.047
Phosphorylation	Proline	+ 79.966
Carboxyamidomethylation	Cysteine	+ 57.02
Propioamide	Cysteine	+ 71.037
Mono-link (DSG)	Lysine	+ 114.032

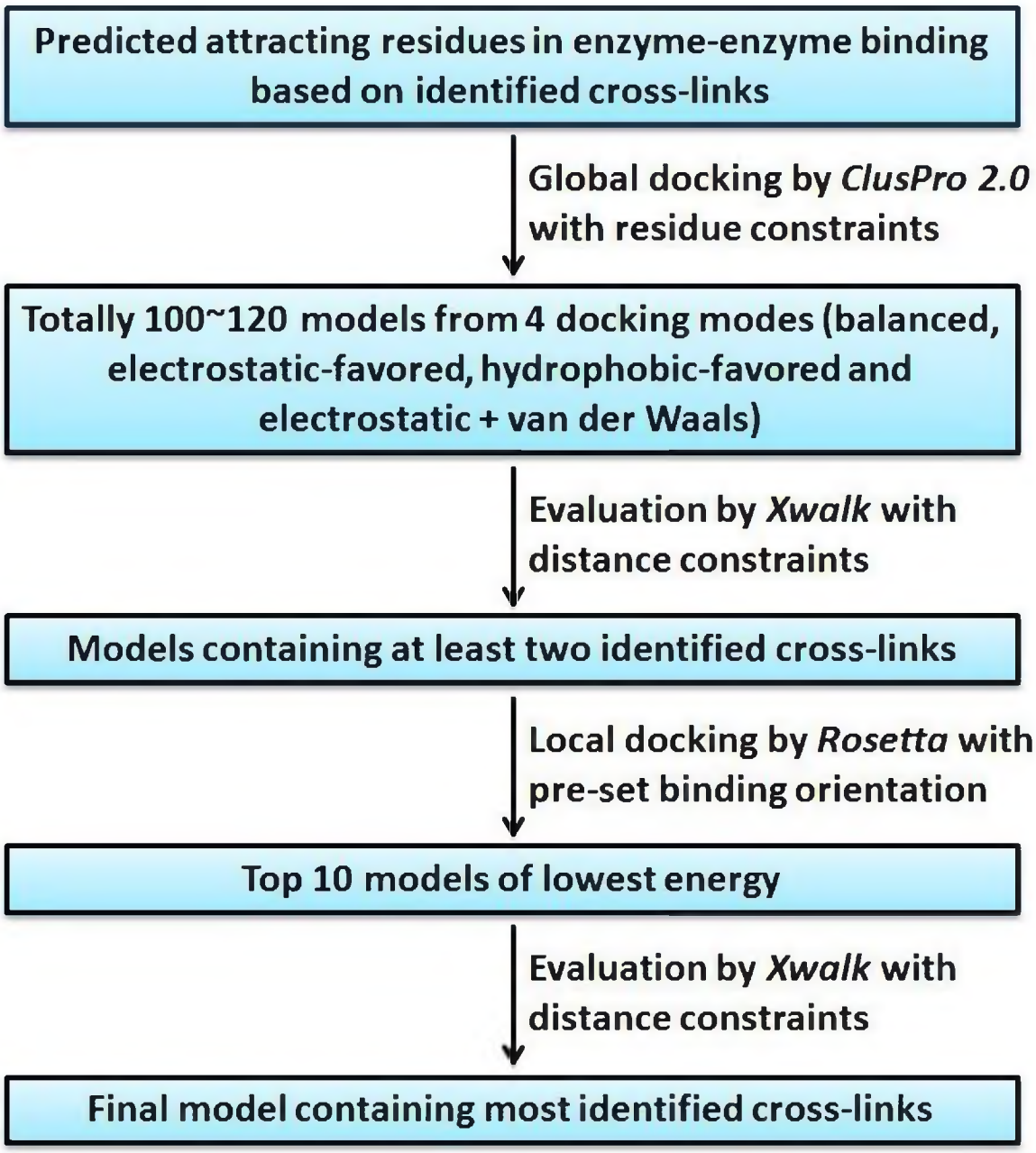

Figure 3.1 Schematic of the Hybrid Protein Docking.

protein docking web server, *Cluspro* (http://cluspro.bu.edu/), was utilized. Cross-linked lysines identified from manual search were set as attracting residues. All proteins were treated as rigid bodies with their "open" conformations obtained from crystal structures. Initial approximation based on surface shape complementarity gives 10^{10} putative complex structures, top scoring 20000 of them being filtered by desolvation and electrostatic energetics to give 500 structures of lowest desolvation free energy and 1500 structures of lowest electrostatic energy. In a landscape of free energy versus root-mean-square deviation of atomic positions (RMSD), native structures always have the highest number of "neighbors" (probably of structural similarity) clustering around. Therefore, the 2000 candidate structures were valued by moving one of the two proteins around binding sites to achieve a free energy map of all subsequent structures. Most promising global candidates were selected as their cluster radius was no more than 9 Å by default.[21-24]

Prior to local docking, all model candidates were screened by *Xwalk* software suite[25] to filter out false positives of global candidates by distance constraints. Maximum Euclidean distance limit was set to 25 Å, which is a combination of DSG spacer arm length (7.7 Å), lysine side chain length (6 Å × 2) and backbone flexibility. In addition to Euclidean distance limit, solvent accessible surface (SAS) distance was also set to 30 Å, to mimic molecular flexibility of DSG when cross-linking two residues without penetrating protein surface. Solvent radius was 1.4 Å by default and set to 2 Å for SAS distance calculation. Rotamers were removed and only the distance of Cβ-Cβ between two lysines was calculated.[26] A pair of lysines on two proteins in global candidates with their *Xwalk*-calculated separation no more than the limits were considered as a potential cross-link.

After distance filtering, global candidates bearing at least two potential cross-links were subject to local docking accomplished by another protein docking web server, *Rosetta* (http://rosie.rosettacommons.org/). Starting with the given globally docked structure, the program calculated interface energies (versus RMSD) of 1000 possible relative conformations at binding sites.[27-29] Derived from each starting global structure, 10 local candidates of lowest interface energy were screened again by *Xwalk*. Final complex structures were chosen based on two criteria: (1) local candidates of lowest interface energy were clustered around a single position on the energy landscape and (2) the structure had most potential cross-linkers in agreement with experimental results. Interfacial residues in final structures were determined when the measured Euclidean distance was less than 20 Å.

3.2.10 Simulation of Surface Electrostatic Potential

Prior to simulation, .docked structures were modified by *PDB2PQR* web server (http://nbcr-222.ucsd.edu/pdb2pqr_2.0.0/) to add missing hydrogens and/or heavy atoms and estimate their titration states. Protein complexes were protonated with favorable hydrogen bonds. Charges and radius were assigned from Amber force field.[30,31] *PROPKA* was used to predict pK_a shifts in complexes at pH 7.8, which is the pH of mitochondrial matrix[32,33]. Calculation of surface ESP by Possion-Boltzmann equation was done by *APBS* web server (http://www.poissonboltzmann.org/docs/apbs-installation/) with the following parameter settings: (1) water molecules were not removed; (2) no additional ions were added; (3) biomolecular dielectric constant was set at 2; and (4) solvent dielectric constant was set at 78.54.[34]

3.2.11 Graphic Preparation

All figures of protein structures and visualization of surface ESP were made in *Chimera* obtained from www.cgl.ucsf.edu/chimera/.

3.3 Results and Discussion

3.3.1 Separation of the Cross-Linked TCA Cycle Metabolon

Treatment of intact mitochondria with a membrane-permeable cross-linker fixes matrix proteins to membrane proteins. As a result, an increased amount of matrix proteins would sediment with broken membrane fractions in large aggregates during differential centrifugation and hydrophobicity-mediated precipitation. After centrifugation, much lighter yellowish color and lower protein amount were observed in the supernatant of cross-linked sample than non-cross-linked one, implying significant loss of soluble proteins. In order to enrich the TCA cycle enzymes still soluble in the supernatant, gel-based separation was chosen instead of chromatographic separation to avoid further protein loss and dilution. Since all of the samples were treated with a reducing agent, dithiothreitol (DTT), protein oligomers or complexes dissociated upon cleavage of intrinsic disulfide bonds unless they were cross-linked. As shown in Figure 3.2, in the lane where non-cross-linked sample was applied, a set of discrete subunit/small protein bands formed below 100 kDa. In the cross-linked lane, these bands were faint or disappeared whereas the region above 100 kDa became darker and bands smeared, indicating formation of large protein complexes. Previously D'Souza *et al.* had detected specific activities of mMDH, CS and FUM in the starting well after *in vivo* cross-linking, suggesting that the resultant TCA cycle complex was too huge to migrate through the gel pores.[35] In our experiment, we also found that additional intense protein bands appeared at the top of the gel just near the well. Based

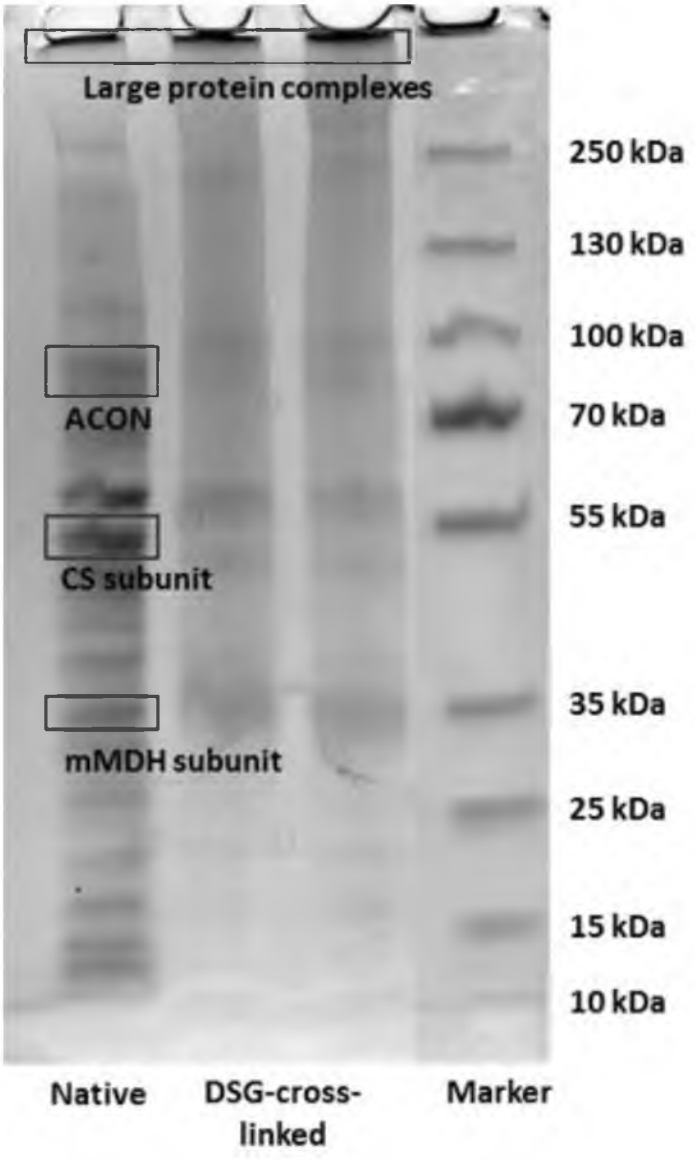

Figure 3.2 Reducing SDS-PAGE of cross-linked and native (non-cross-linked) mitochondrial supernatant. Bands in black squares were cut for digestion and mass spectrometric analysis.

on the assumption that the TCA cycle metabolon is over 8000 kDa[36], those top bands were cut for in gel digestion and LC-MS/MS analysis. The top region of the same location in the non-cross-linked lane as well as individual subunit bands were also analyzed as the native control.

3.3.2 Identification of the Cross-Linked TCA Cycle Metabolon

As listed in Table 3.2, only mMDH and CS were present in the non-cross-linked band, indicating dissociation of the metabolon but a relatively stronger interaction between these two enzymes. After cross-linking, all of the TCA cycle enzyme components were identified with at least one tryptic peptide matching the database, which confirms again the existence of the metabolon. As mentioned in Chapter 1, SDH is also the complex II of the ETC in the inner mitochondrial membrane and anchors the rest of the TCA cycle to the membrane surface. Cross-linking of SDH to its neighbors in the TCA cycle and ETC, led to their co-precipitation during centrifugation and ammonium sulfate precipitation. According to the supramolecular model of the TCA cycle metabolon proposed by Lyubarev and Kurganov, the αKGDH complex acts as the nucleus surrounded by SCS and FUM, followed by assembly of mMDH, CS, ACO and ICDH at the outer shell.[36] Trypsin digestion might be less efficient in the core of the giant complex, causing missed detection of enzyme peptides. In consequence, much fewer tryptic peptides of SDH, FUM, SCS and KDH were found matching the database.

3.3.3 Structural Modeling of the mMDH-CS-ACO Complex

In search of potentially conjugated lysines, cross-linking induced additional peptide peaks were compared to a manually generated theoretical mass library for all possible combinations between available mMDH, CS and ACO peptide fragments. As shown in

Table 3.2 Identified TCA cycle enzymes in SDS-PAGE bands.

Sample	Enzyme name	Mass (Da)	Peptides matched
Non-cross-linked	mMDH	33061	4
	CS	51673	2
DSG-cross-linked	mMDH	33061	33
	ACO	85304	14
	CS	51673	13
	ICDH	50792	11
	SCS	46774	3
	KDH	48554	2
	FUM	49978	1
	SDH	72280	1

Figure 3.3, there is a complex cross-linking network after the initial search. However, it should be kept in mind that the majority of these peaks actually came from other proteins, and cross-linking would not likely occur at some lysine residues inaccessible to solvent. Despite inter-protein cross-linker, there could be DSG "loops" in the same chain or "dead ends" with one end simply hydrolyzed.

With the distance constraints on noted lysine residues in Figure 3.3, docking of PPIs in the mMDH-CS-ACO complex was conducted in a rational manner. CS homodimer, the biggest of the three enzymes, was set as the receptor during modeling. Prior to docking, mMDH was allowed to explore the entire surface of CS in the absence of ACO until a model was found to satisfy the distance requirement. As shown in Figure 3.4C, mMDH-CS complex turns out to be asymmetric, which is quite different from the symmetric quinary model proposed by Srere *et al.*[17]. In this complex, both subunits of mMDH bind to one side of CS. A long α–helix in CS from Ser2 to His28 is buried in the interface that lies across the intersubunit domain of mMDH. N- and C-terminus in one of CS subunits and one C-terminal of mMDH are found located next to binding interface, but they are still in the open space and accessible to solvent and cross-linkers. Three cross-links were identified between mMDH Lys300, Lys304 and CS Lys432, Lys437. The two N-terminus of mMDH are far from the binding interface and faces the opposite direction. Distance measurements revealed the following interfacial residues: mMDH Ile34-Pro38, Tyr56-60, Gly77-Thr95, Lys215-Ala220 and CS Ser2-His28, Ser424-Lys437.

Docking ACO to CS was performed in the presence of mMDH. As indicated by protein identification, CS has stronger affinity for mMDH than for ACO. Therefore, the presence of mMDH may affect ACO's exploring the surface of CS. Assuming that the

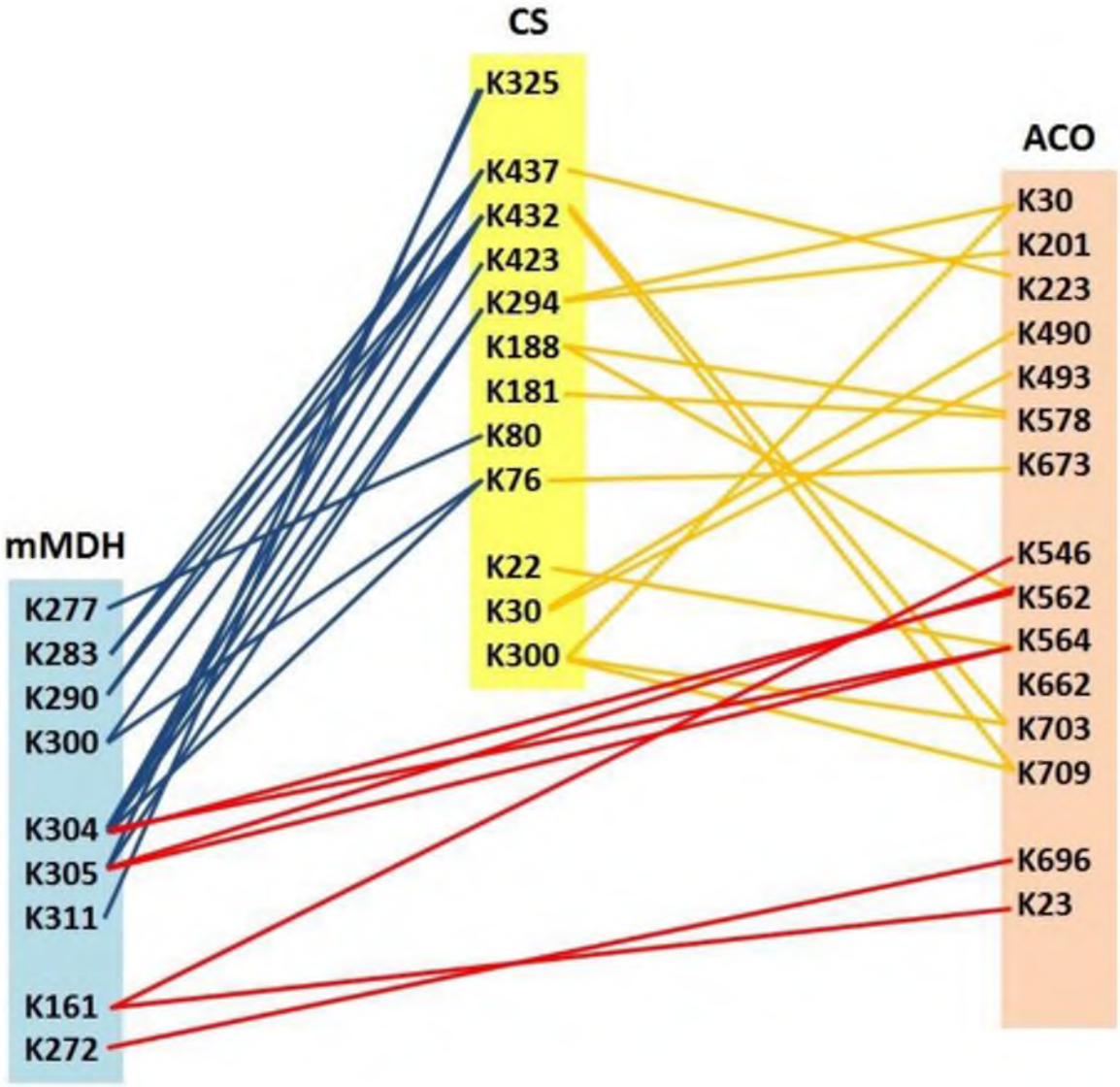

Figure 3.3 Network of cross-link candidates in mMDH-CS-ACO complex.

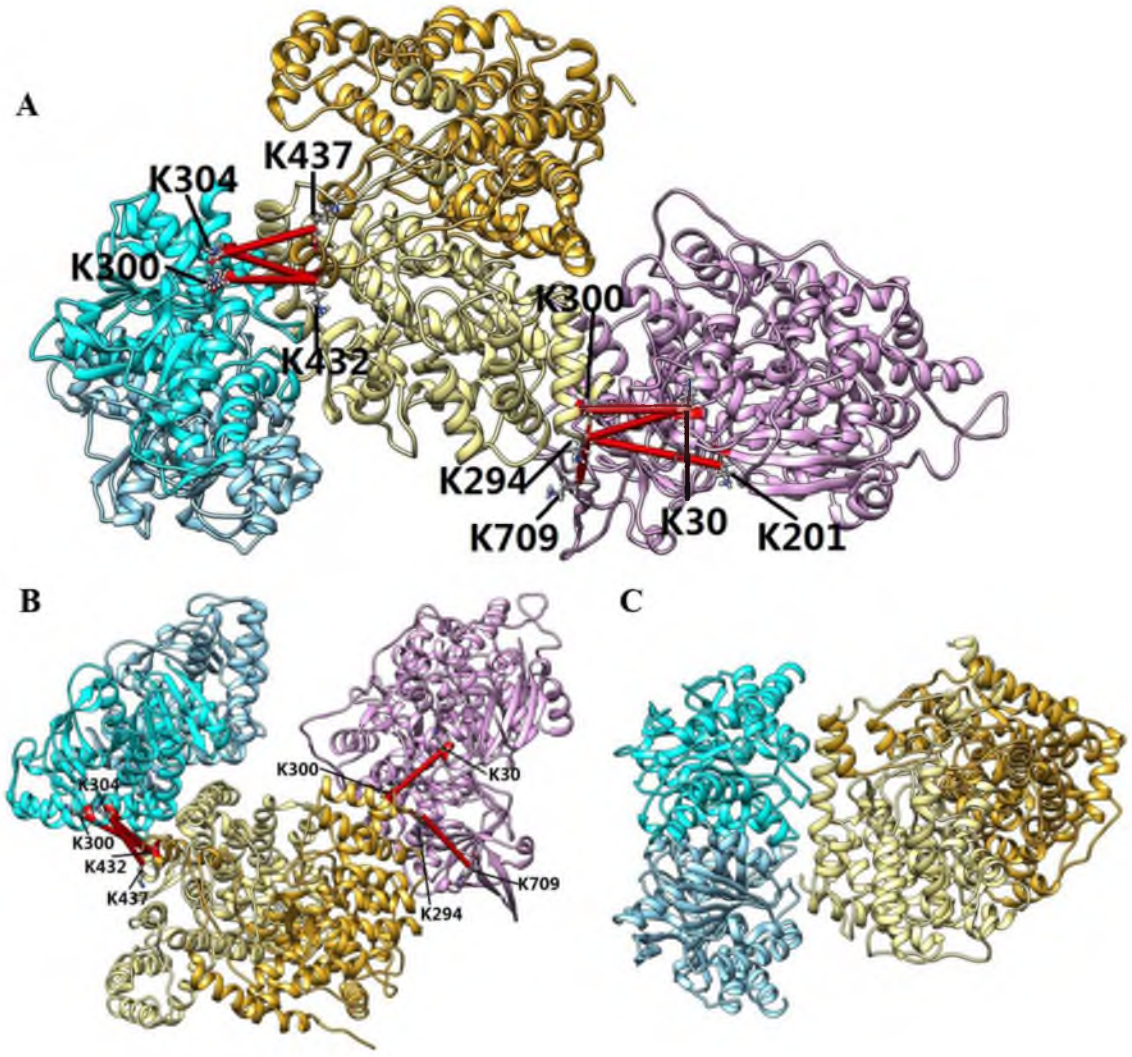

Figure 3.4 Two models, MCA1 (**A**) and MCA2 (**B**) of mMDH-CS-ACO complex and model of mMDH-CS complex in the absence of ACO (**C**). The two chains of CS are colored in goldenrod and khaki. The two chains of mMDH are colored in sky blue and cyan. Monomeric ACO is colored in plum. Identified cross-links are represented by red bars with linked lysine residues numbered.

stoichiometric ratio was 1:1:1, we proposed two models for the mMDH-CS-ACO complex. As illustrated in Figure 3.4A, ACO binds the same CS subunit as mMDH does and its C-terminal extends into the inter-subunit pocket of CS. Four cross-links were identified between ACO Lys30, Lys201, Lys709 and CS Lys294, Lys300. There is another possibility that ACO and mMDH are located on opposite sides (MCA2), as shown in Figure 3.4B. Change of position does not cause increased separation of mMDH and ACO. On the contrary, their distance is dramatically shortened and the closest amino acids are within only 15 Å. Enhanced association between mMDH and ACO, however, led to a slightly loosened connection between CS and ACO. Only two cross-links were identified between ACO Lys30, Lys709 and CS Lys294, Lys300. Nonetheless, in both models, the C-terminus as well as the following regions of ACO were found to interact with the same amino acids of CS: ACO Asp48-Glu54, Phe544-Asp551, Leu702-Ala706, Glu733-Lys754, and CS Arg195-Ser199, Gly218-Asp221, Thr286-Val296, Pro342-Pro345, Gly218-Asn391. However, no potential cross-links between mMDH and ACO were identified in either MCA1 or MCA2.

Forming complexes definitely brings enzyme active sites in close proximity, reducing diffusion lengths for substrates. As shown in Figure 3.5, the average distances between active sites are about 35 Å for mMDH-CS and 50 Å for ACO-CS in MCA1. Docking mMDH and ACO onto different subunits of CS resulted in increased active site separation to 65 Å for ACO-CS, and it seems less favorable for efficient substrate transport than MCA1 where mMDH and ACO are separated by only one active center. Comparing the binding surface areas (buried solvent accessible areas), MCA1, which has 10000 $Å^2$ for mMDH-CS and 13000 $Å^2$ for ACO-CS is more thermodynamically favorable than MCA2,

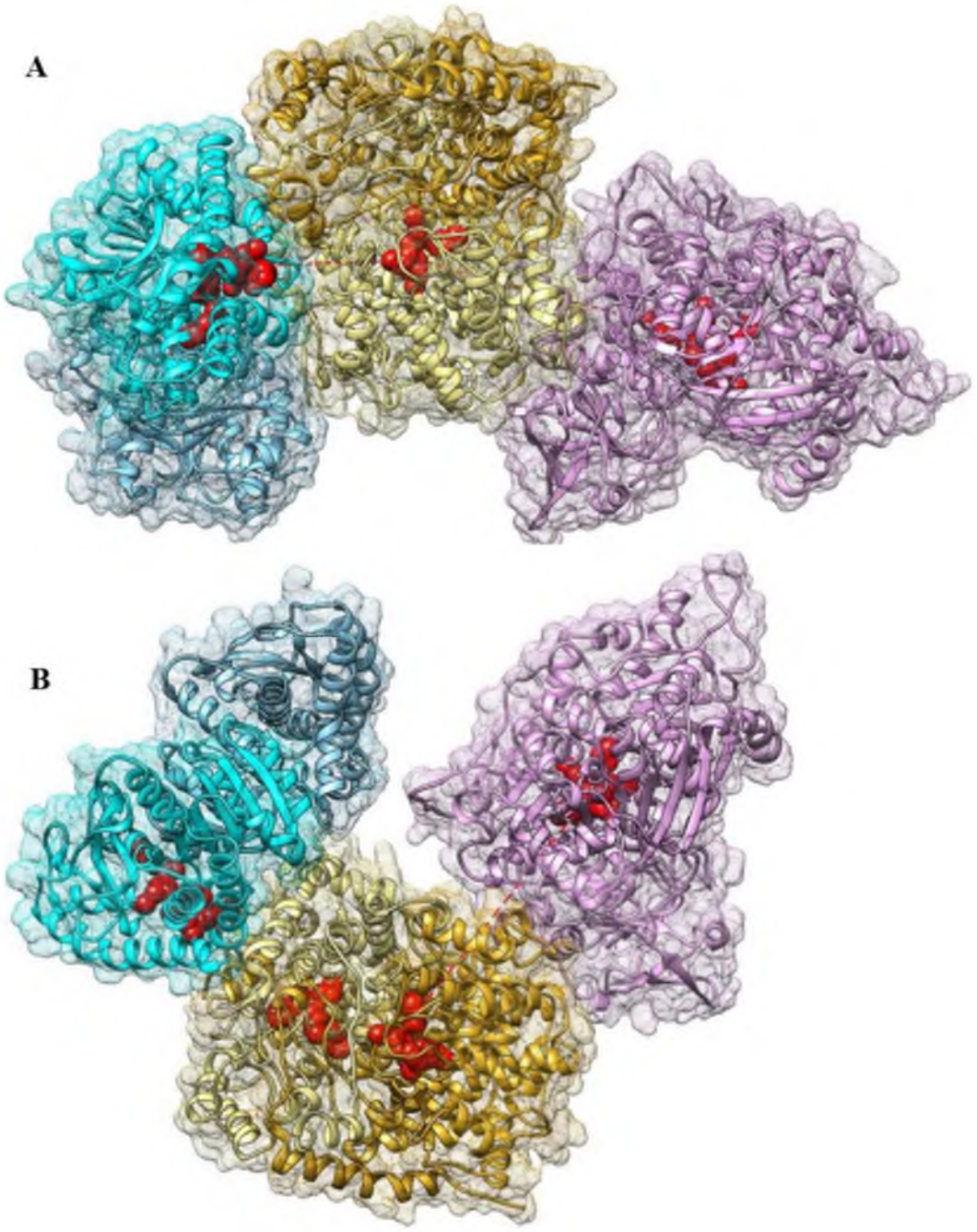

Figure 3.5 Active sites (red spheres) in MCA1 (**A**) and MCA2 (**B**): mMDH Ile12, Arg80, Arg86, Asn118, Arg152 and His 176;[37] CS His238, Asn242, His 274 and Arg401;[38] ACO His101, Asp165, Ser166, His167, Cys358, Arg447, Arg452, Ser642, Ser643 and Arg644.[39] which has 10000 $Å^2$ for mMDH-CS and 12000 $Å^2$ for ACO-CS.

red dashed line represents the Euclidean distance. Meshed surface of the complex was created in *Chimera*.

3.3.4 Electrostatic Channeling in the mMDH-CS-ACO Complex

A theoretical study done by Elcock and McCammon demonstrated that the presence of surface electrostatic forces resulted in one order of magnitude increase in substrate-transport efficiency, while less than 1% of molecules were directly transported without electrostatic forces.[40] In this work, simulation of the surface electrostatic potentials of the metabolon structures proved the charge rearrangement and electrostatic channeling formation upon protein-protein association. As illustrated in Figure 3.6, free CS is slightly negatively charged at pH 7.8, but an area of positive potential extends from the inside of the cleft where the active sites are located to the outer surface. Similar positively charged patterns are found at active site regions in free mMDH and ACO. This will definitely help accommodate carboxylate substrates (L-malate, OAA and citrate) into the right place. In the unbound state, most of the enzyme surface stays nearly neutral. In the complex, these positively charged patterns get expanded across binding interfaces and interconnected to form a continuous band (channel) linking active sites. In the meantime, negatively charged patterns have also been rearranged to cover regions next to the "positive channel". This change seems to make the enzyme surface more "polarized" with electrostatic complementarities maintained. Under combined effects from electrostatic attraction and repulsion, charged intermediates would be microcompartmentalized, and their transport on enzyme surface might be restricted to the electrostatically favored path. It has been noticed that regions participating in the interface formation are mainly nonpolar and hydrophobic, which might also facilitate redistribution and connection of charged patterns. Thus, it can

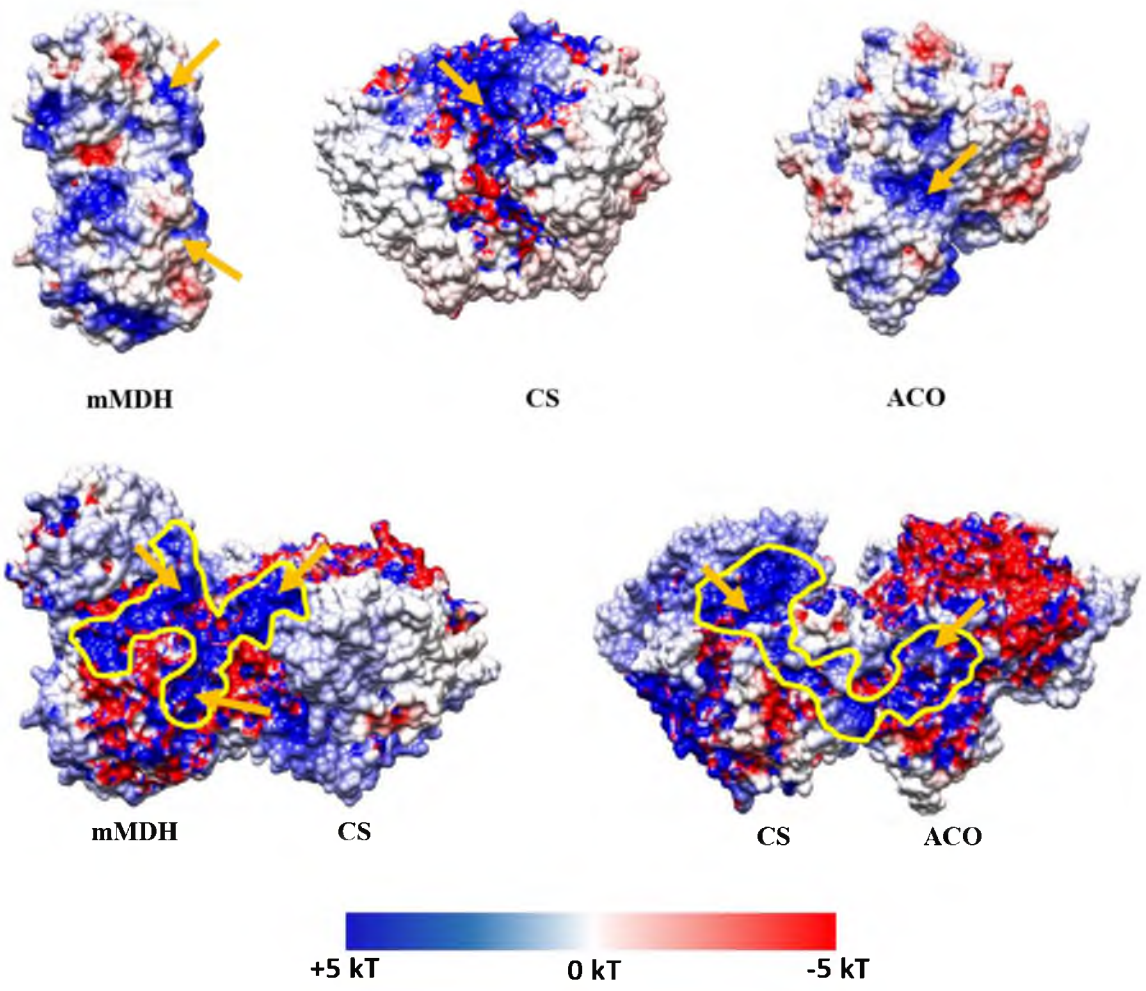

Figure 3.6 Illustration of surface ESP in MCA1 and free enzymes at pH7.8. Active sites are denoted by orange arrows and electrostatic channels are highlighted by yellow edges. Negatively charged, positively charged and neutral regions are colored in red, blue and white.

be seen that the formation of substrate channeling in metabolons may be an outcome of complex balancing of both electrostatic and hydrophobic interactions.

3.3.5 Symmetric Model of the mMDH-CS-ACO Complex

Finally, we constructed a higher-ordered model for the mMDH-CS-ACO complex based on MCA1. As shown in Figure 3.7, the central core, the CS dimer, is surrounded by two mMDH dimers and two ACO monomers. Each asymmetric subunit, composed of one CS subunit, one mMDH dimer and one ACO monomer, is symmetric to the other, making the octamer a two-fold symmetry.

3.4 Conclusions

In this chapter, the existence of the TCA cycle metabolon has been experimentally demonstrated by identifying all of the eight enzymes through *in vivo* cross-linking and mass spectrometry. Using distance constraints derived from cross-links, two models for the wild-type mMDH-CS-ACO complex were proposed, and a two-fold symmetric octamer has been constructed by two mMDH dimers, one CS dimer, and two ACO monomers. Analysis of surface electrostatic potential of the model shows that rearrangement of surface charge patterns upon protein-protein association leads to forming a continuous positively charged zone across their interface. This would consequently facilitate directed transport of carboxylate substrates from one active site to the next. Until this work, direct observation of substrate channeling remained a big hurdle in metabolon research, even though simulation work has built a theoretical foundation for its metabolic implications. This investigation of natural TCA cycle metabolons gains structural insight into the organization of wild-type enzymes within the mitochondrial matrix, and provides an orientation option (MCA1) for engineered TCA cycle metabolon to achieve substrate channeling *in vitro*.

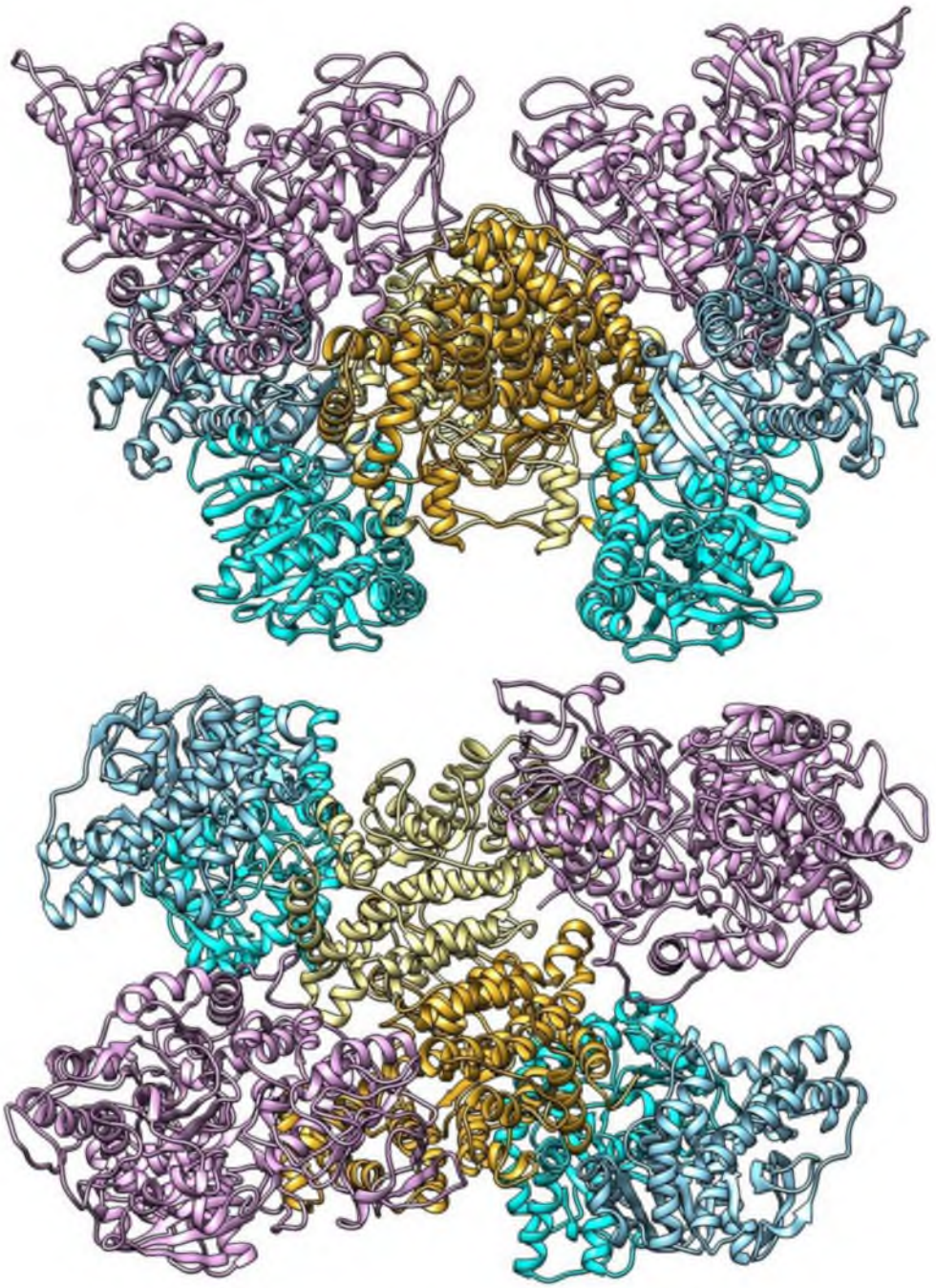

Figure 3.7 Two views of the octamer of the mMDH-CS-ACO complex. Top: 2-fold symmetry axis is parallel to the plane and passes through the center of CS dimer. Bottom: 2-fold symmetry axis is perpendicular to the plane and points from the center of CS dimer.

3.5 References

(1) Schreiber, G. *Curr. Opin. Struct. Biol.* **2002**, *12*, 41.

(2) Kozer, N.; Kuttner, Y. Y.; Haran, G.; Schreiber, G. *Biophys. J.* **2007**, *92*, 2139.

(3) Moreira, I. S.; Fernandes, P. A.; Ramos, M. J. *Proteins* **2007**, *68*, 803.

(4) Keskin, O.; Gursoy, A.; Ma, B.; Nussinov, R. *Chem. Rev.* **2008**, *108*, 1225.

(5) Conte, L. L.; Chothia, C.; Janin, J. *J. Mol. Biol.* **1999**, *285*, 2177.

(6) Young, L.; Jernigan, R. L.; Covell, D. G. *Protein Sci.* **1994**, *3*, 717.

(7) Dill, K. A. *Biochemistry* **1990**, *29*, 7133.

(8) Sheinerman, F. B.; Norel, R.; Honig, B. *Curr. Opin. Struct. Biol.* **2000**, *10*, 153.

(9) Leitner, A.; Walzthoeni, T.; Kahraman, A.; Herzog, F.; Rinner, O.; Beck, M.; Aebersold, R. *Mol. Cell. Proteomics* **2010**, *9*, 1634.

(10) Rabilloud, T. *Method. Mol. Biol.* **2008**, *432*, 83.

(11) Lovric, J. In *Introducing Proteomics: from Concepts to Sample Separation, Mass Spectrometry and Data Analysis*; John Wiley & Sons Ltd: Chichester, **2011**, p 21.

(12) Sinz, A. *Mass. Spectrom. Rev.* **2006**, *25*, 663.

(13) Crews, P.; Rodriguez, J.; Jaspars, M. In *Organic Structure Analysis*; Oxford University Press, Inc.: New York, **2010**, p 273.

(14) Lovric, J. In *Introducing Proteomics: from Concepts to Sample Separation, Mass Spectrometry and Data Analysis*; John Wiley & Sons Ltd: Chichester, **2011**, p 83.

(15) Schoffelen, S.; van Hest, J. C. M. *Soft Matter* **2012**, *8*, 1736.

(16) Shatalin, K.; Lebreton, S.; Rault-Leonardon, M.; Velot, C.; Srere, P. A. *Biochemistry* **1999**, *38*, 881.

(17) Velot, C.; Mixon, M. B.; Teige, M.; Srere, P. A. *Biochemistry* **1997**, *36*, 12471.

(18) Paul, F. E.; Hosp, F.; Selbach, M. *Methods* **2011**, *54*, 387.

(19) Vasilescu, J.; Figeys, D. *Curr. Opin. Biotechnol.* **2006**, *17*, 394.

(20) Pallotti, F.; Lenaz, G. *Method. Cell Biol.* **2007**, *80*, 3.

(21) Comeau, S. R.; Gatchell, D. W.; Vajda, S.; Camacho, C. J. *Nucleic Acids Res.* **2004**, *32*, W96.

(22) Comeau, S. R.; Gatchell, D. W.; Vajda, S.; Camacho, C. J. *Bioinformatics* **2003**, *20*, 45.

(23) Kozakov, D.; Beglov, D.; Bohnuud, T.; Mottarella, S. E.; Xia, B.; Hall, D. R.; Vajda, S. *Proteins* **2013**, *81*, 2159.

(24) Kozakov, D.; Brenke, R.; Comeau, S. R.; Vajda, S. *Proteins* **2006**, *65*, 392.

(25) Kahraman, A.; Malmstrom, L.; Aebersold, R. *Bioinformatics* **2011**, *27*, 2163.

(26) Herzog, F.; Kahraman, A.; Boehringer, D.; Mak, R.; Bracher, A.; Walzthoeni, T.; Leitner, A.; Beck, M.; Hartl, F. U.; Ban, N.; Malmstrom, L.; Aebersold, R. *Science* **2012**, *337*, 1348.

(27) Chaudhury, S.; Berrondo, M.; Weitzner, B. D.; Muthu, P.; Bergman, H.; Gray, J. J. *PLoS One* **2011**, *6*, e22477.

(28) Lyskov, S.; Chou, F. C.; Conchuir, S. O.; Der, B. S.; Drew, K.; Kuroda, D.; Xu, J.; Weitzner, B. D.; Renfrew, P. D.; Sripakdeevong, P.; Borgo, B.; Havranek, J. J.; Kuhlman, B.; Kortemme, T.; Bonneau, R.; Gray, J. J.; Das, R. *PLoS One* **2013**, *8*, e63906.

(29) Lyskov, S.; Gray, J. J. *Nucleic Acids Res.* **2008**, *36*, W233.

(30) Dolinsky, T. J.; Czodrowski, P.; Li, H.; Nielsen, J. E.; Jensen, J. H.; Klebe, G.; Baker, N. A. *Nucleic Acids Res* **2007**, *35*, W522.

(31) Dolinsky, T. J.; Nielsen, J. E.; McCammon, J. A.; Baker, N. A. *Nucleic Acids Res* **2004**, *32*, W665.

(32) Søndergaard, C. R.; Olsson, M. H. M.; Rostkowski, M.; Jensen, J. H. *J. Chem. Theory Comput.* **2011**, *7*, 2284.

(33) Olsson, M. H. M.; Søndergaard, C. R.; Rostkowski, M.; Jensen, J. H. *J. Chem. Theory Comput.* **2011**, *7*, 525.

(34) Baker, N. A.; Sept, D.; Joseph, S.; Holst, M. J.; McCammon, J. A. *Proc. Natl. Acad. Sci. U. S. A.* **2001**, *98*, 10037.

(35) D'Souza, S. F.; Srere, P. A. *Biochim. Biophys. Acta* **1983**, *724*, 40.

(36) Lyubarev, A. E.; Kurganov, B. I. *BioSystems* **1989**, *22*, 91.

(37) Gleason, W. B.; Fu, Z.; Birktoft, J.; Banaszak, L. *Biochemistry* **1994**, *33*, 2078.

(38) Remington, S.; Wiegand, G.; Huber, R. *J. Mol. Biol.* **1982**, *158*, 111.

(39) Lauble, H.; Kennedy, M. C.; Beinert, H. *Biochemistry* **1992**, *31*, 2735.

(40) Elcock, A. H.; Huber, G.; McCammon, J. A. *Biochemistry* **1997**, *36*, 16049.

CHAPTER 4

CHARACTERIZATION OF POLYMERIRC CO-IMMOBILIZATION OF THE TCA CYCLE ENZYMES USING FÖRSTER RESONANCE ENERGY TRANSFER

4.1 Background Introduction

4.1.1 Föster Resonance Energy Transfer

Förster resonance energy transfer (FRET) is a nonradiative energy transfer between a donor fluorophore and a nearby acceptor, a part of whose absorption spectrum overlaps with the donor emission spectrum. As illustrated by the Jablonski diagram (Figure 4.1), electronically excited donor molecules tend to return to the ground states by releasing extra energies through fluorescent emission or non-radiative decay. Long range dipole-dipole interactions can cause the intermolecular energy transfer from the excited donor to the acceptor at the ground state without emitting photons. As a result, the fluorescence of the donor fluorophore is quenched and its emission intensity decreases. In the meantime the excited acceptor may release photons of lower energies in terms of another emission peak at longer wavelengths. FRET efficiency (E) is defined as the extent of donor excitation energy transferred to the acceptor, and dependent on (1) spectrum overlap integral between donor emission and acceptor absorption spectra ($J(\lambda)$), (2) donor-acceptor distance (r), (3) relative orientation factor of donor and acceptor transition moments (κ^2), (4) donor quantum yield (Q_D), and (5) lifetime of donor (τ_D). Given donor emissive rate

Reprinted from "Wu, F., Minteer, S. D. *Biomacromolecules* **2013**, *14*, 2739" with permission from the American Chemical Society

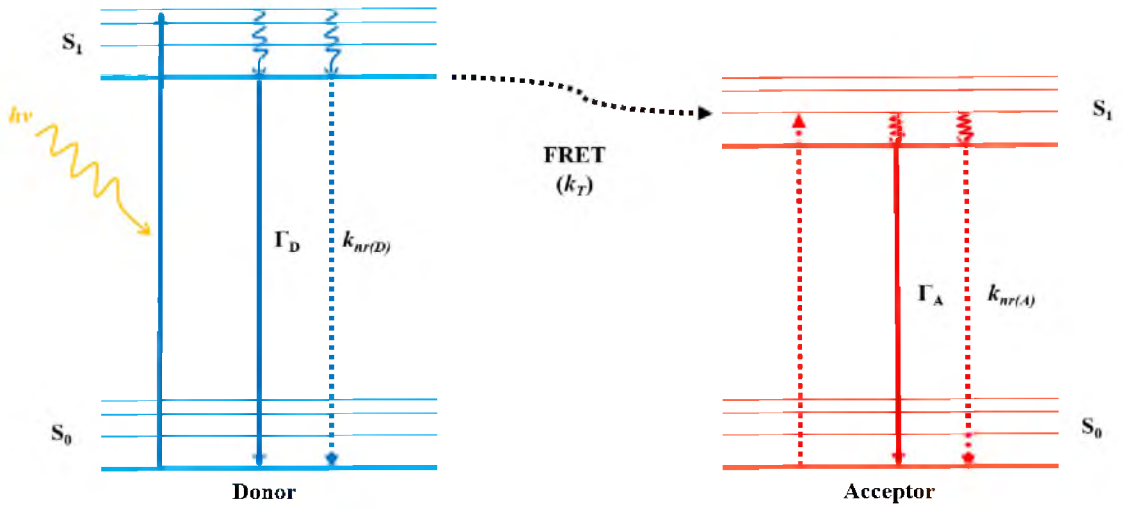

Figure 4.1 Jablonski diagram of fluorescence emission (Γ_D and Γ_A), non-radiative decay ($k_{nr(D)}$ and $k_{nr(A)}$) and FRET (k_T).

(Γ_D), donor non-radiative decay rate ($k_{nr(D)}$) and energy transfer rate (k_T), E is calculated by

$$E=\frac{k_T}{\Gamma_D+k_{nr(D)}+k_T}$$

Taking into account that

$$k_T=\frac{Q_D\kappa^2}{\tau_D r^6}\left(\frac{9000\ln 10}{128\pi N_{Avo} n^4}\right)J(\lambda)\int_0^\infty F_D(\lambda)d\lambda$$

and defining the Förster distance, which is a characteristic distance of a specific donor-acceptor pair

$$R_0=8790\sqrt[6]{Q_D\kappa^2 n^{-4} J(\lambda)}$$

where n is the refractive index of the medium, then

$$k_T=\frac{1}{\tau_D}\left(\frac{R_0}{r}\right)$$

and energy transfer efficiency can be calculated by

$$E=\frac{1}{1+(r/R_0)^6}$$

It can be seen that the extent of energy transfer is directly linked to the spatial separation between donor and acceptor. Because the FRET efficiency can be obtained from measured fluorescence intensity in steady-state experiment or fluorescence lifetime in time-resolved experiment, one can determine the distance between donor and acceptor, which is of great significance to studying interactions or spatial organization of biomacromolecules.[1]

4.1.2 Photobleaching FRET Imaging

Photobleaching refers to destroying fluorophores by repeated excitation. This process is irreversible and results in partial or complete loss of fluorescence. In a FRET system, photobleaching of the donor or acceptor quenches energy transfer and reduces

FRET efficiency. When the donor is photobleached, sensitized acceptor fluorescence intensity will decrease or be eliminated. When the acceptor is photobleached then quenched donor fluorescence will get recovered. In studying biomacromolecules in cells or immobilized onto a substrate or scaffold by FRET imaging, it is always difficult to calculate FRET efficiency from averaged fluorescence intensities when fluorophores are not uniformly distributed. Self-quenching also interferes with the accurate measurement of FRET efficiency. Therefore, photobleaching FRET imaging is exploited to rule out the effect of self-quenching and enable an *in situ* analysis of emission intensities of the fluorophore before and after its FRET partner being destructed, usually by a high-power laser beam or long exposure to laser scanning.[2]

4.1.3 Polymeric Co-Immobilization of Enzyme Cascade

Studies have shown that cytoskeleton in cytoplasm and organelles provides metabolic organization with a favorable microenvironment enhancing both protein-protein and protein-scaffold interactions.[3] As a matter of fact, diffusivity of metabolic enzymes is remarkably reduced in such "polymeric" medium[4], and metabolons are associated to structural elements *in vivo*, such as lipid membrane, actin and microtubule.[3] *In vitro*, researchers have also demonstrated immobilization-enhanced protein-protein interactions and coupled activities in polymer matrices.[5] Early in 1970s, Mattiasson *et al.* observed an increase in coupled catalytic rate of a two-enzyme cascade in PEG solution.[6] Srere *et al.* reported an activity and kinetic promotion of a three-enzyme system entrapped in cross-linked polyacrylamide gels.[7] Up to now, a variety of polymer families and immobilization techniques have been developed for assembling enzyme cascades. Generally, multiple enzymes may be attached to polymer matrices through absorption, covalent conjugation,

electrostatic attraction, or hydrophobic interaction, or by encapsulation in micelles or polymersomes. Hence, polymers are modified to meet different immobilization goals. Functional groups are added to achieve covalent polymer-enzyme linkages. Side chains are made polar or charged to enhance hydrophilic or ionic interactions. Hydrophilic polymer backbones can be tailored by alkyl chains as to introduce the amphiphilicity, which is believed to be a nontrivial environmental factor in stabilizing metabolons. Then it is not surprising to see the improvement of multienzyme association in hydrophobically modified polymer matrices.[8,9]

4.1.4 Hydrophobic Modification for Co-Immobilization of the TCA Cycle Cascade

In this work three types of polymers are investigated for co-immobilization of a three-enzyme system: polyethyleneimine (PEI), Nafion (NF) and chitosan (CHIT). All of them are commonly used for BFC fabrication due to their open accessibility for chemical modification and good compatibility with enzymes and electrodes.

4.1.4.1 Polyethyleneimine. PEI is a water-soluble polyamine that can associate tightly to negatively charged residues and form PEI-protein complexes. Secondary amines in linear PEI (LPEI) are very reactive, enabling modifications by various reagents. Ethylene glycol diglycidyl ether (EGDGE) has been frequently used in creating a cross-linked, robust LPEI hydrogel. LPEI can also be alkylated by halogenoalkane through nucleophilic substitution. For instance, reaction with 1-bromooctane attaches an octyl alkyl chain to the backbone secondary amine and yields C8-LPEI.[10,11]

4.1.4.2 Nafion. Nafion is a perfluorinated cation-exchange polymer which is widely used for electrochemical applications.[12] Once cast, Nafion membrane is constructed by the hydrophobic fluorocarbon backbone, the hydrophilic ionic clusters of sulfonic acid groups

and the interfacial space.[13] When treated with alkylated phosphonium or quaternary ammonium salts, Nafion will exchange protons at the sulfonic acid sites for the alkylated phosphonium or ammonium ions, which then changes the size of its micellar structures. Moreover, neutralization by alkylation makes the polymer more compatible to enzymes.[12,14]

4.1.4.3 Chitosan. Chitosan is a polysaccharide derived from chitin which is found abundant in nature.[15] Similar to PEI, chitosan also interact with negatively charged species when its primary amines in the backbone are protonated, which makes the polymer a good protein-precipitating reagent. On the electrode, it can form a macroporous 3D scaffold that allows much faster mass transport from bulk solution to the electrode. By attacking the primary amine with aldehydes, alkyl chains of different lengths can be tailored to the hydrophilic backbone of chitosan. This will not only prevent extensive conjugation or precipitation during immobilization, but also introduce an amphiphilic microenvironment for enzymes.[16,17]

4.1.5 Aims

Martin *et al.* demonstrated that immobilization can induce homo-aggregation of mMDH and hydrophobic modification would increase the degree of enzyme aggregation in polymers.[9] This then led to the question that whether hetero-aggregation of multiple enzymes can also be enhanced by hydrophobic modification. In order to explore the relationship between spatial organization of enzymes and the microstructure of polymers, the acceptor photobleaching FRET imaging technique was applied in assessing the separation of mMDH, CS and ACO, which were co-immobilized in LPEI, NF, and CHIT as well as their hydrophobically modified derivatives (structures shown in Figure 4.2).

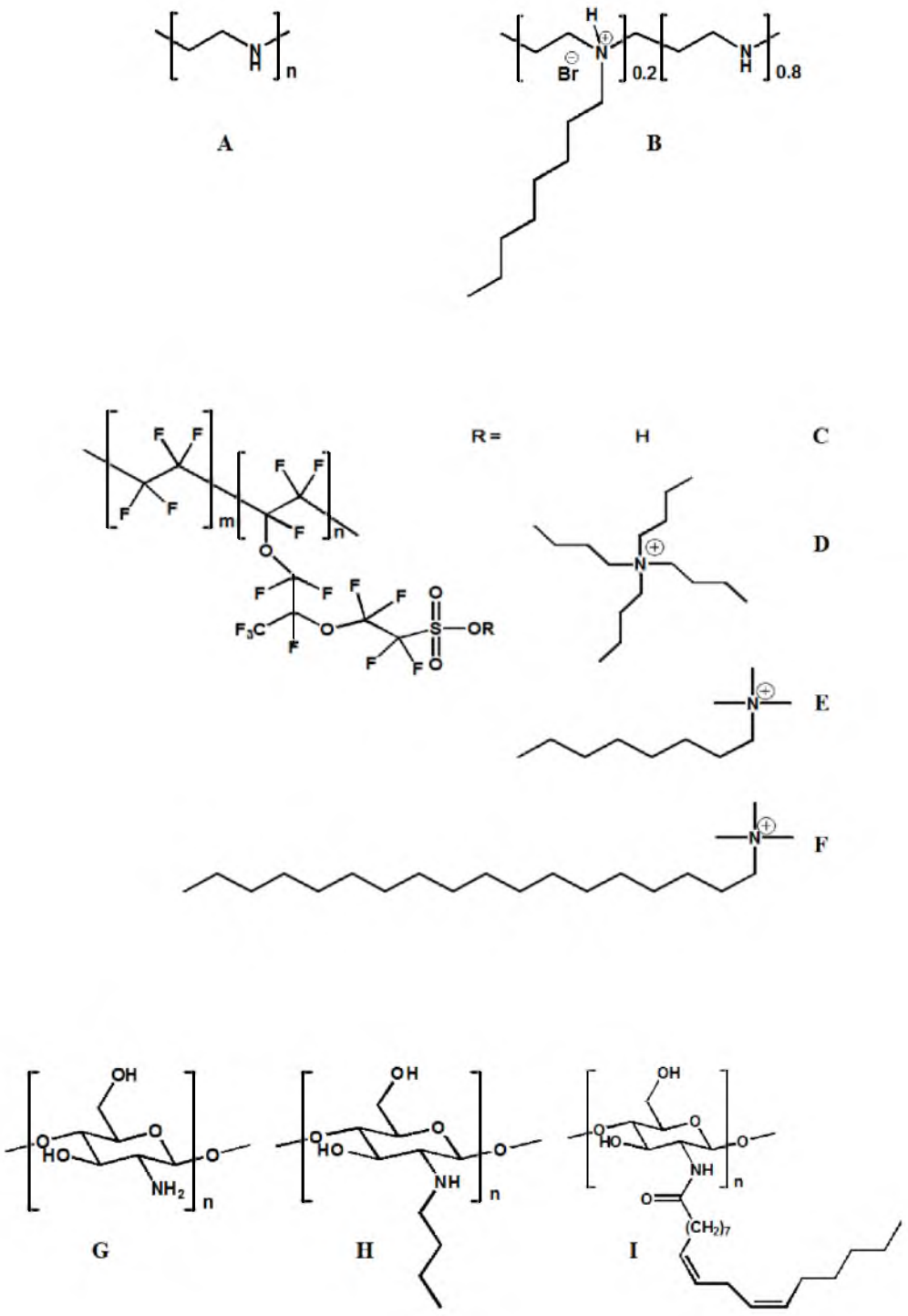

Figure 4.2 Polymer structures: (A) LPEI, (B) C8-LPEI, (C) NF, (D) tetrabutylammonium (TBAB) NF, (E) trimethyloctylammonium (TMOA) NF, (F) trimethyloctadecylammonium (TMODA) NF, (G) CHIT, (H) butyl-modified CHIT (BU-CHIT), (I) α-linoleic acid modified CHIT (ALA-CHIT).

4.2 Experimental

4.2.1 Materials

AlexaFluor® 488 and AlexaFluor® 555 labeling kits were purchased from Invitrogen (Life Technologies). Potassium phosphate was purchased from EMD Chemicals. Sodium phosphate was purchased from Mallinckrodt Baker. Sodium hydroxide and potassium hydroxide were purchased from Macron Chemicals. NAD^+ was purchased from Research Products International. Mitochondrial MDH, CS, ACON and all other chemicals were purchased from Sigma-Aldrich unless otherwise stated.

4.2.2 Preparation of Polymers

Octyl-modified linear polyethyleneimine polymer was synthesized from stock linear polyethyleneimine in the lab using the procedure reported by Moehlenbrock *et al.*[10] (yield: 95%). The chitosan polymers were deacetylated before further modification through the autoclaving method developed by Sjoholm *et al.*[18] (yield: 85%). The butyl-modified chitosan was prepared according to the procedure described by Klotzbach *et al.*[17] (yield: 94%). The α-linoleic acid-modified chitosan was prepared according to the procedure described by Martin *et al.*[19] (yield: 60%). Nafion polymers were modified according to the procedure from Watt *et al.*[20] (yield: 80%).

4.2.2 Fluorescent Labeling of Enzymes

Enzymes were fluorescently labeled as described in Chapter 2 with some modifications. Two milligrams of CS (or mMDH) was dissolved in 1 mL of 100 mM potassium phosphate (pH 7.5) buffer and mixed with one vial of AlexaFluor® 488 (or AlexaFluor® 555). A 100 μL aliquot of 1 M sodium bicarbonate (pH 9.0) was added to increase the reaction pH to ~8.3. Two milligrams of ACON powder was suspended in 1

mL of 50 mM sodium phosphate buffer (pH 8.3) and mixed with one vial of AlexaFluor® 488. All of the mixtures were incubated in the dark at room temperature for 1 h and then at 4 °C for 24 h to allow the conjugation between dyes and primary amines of lysine residues. Unreacted dyes were removed from labeled enzymes through overnight dialysis against 1 L of 50 mM Tris buffer (pH 7.4) at 4 °C, followed by a series of dialysis in 500 mL volumes for 2 to 3 h until their steady-state polarization measured with a fluorescence spectrophotometer (F-7000, Hitachi) remained unchanged (0.20 ~ 0.30). Then, the concentrations of dyes were determined by measuring the UV absorbance of AlexaFluor® 488 at 494 nm (extinction coefficient is 71000 $cm^{-1}M^{-1}$) and of AlexaFluor® 555 at 555 nm (extinction coefficient is 150000 $cm^{-1}M^{-1}$) in a UV-vis spectrophotometer (Evolution 260 Bio, Thermo Scientific). Assuming that no significant amount of enzymes was lost during dialysis, the final dye to enzyme molar ratio was about 1:1. This ratio was controlled to be low to avoid possible interference from attached dyes to enzyme-enzyme interactions. All labeled enzymes were stored in 100 mM potassium phosphate buffer (pH 7.5) in the dark at -20 °C before use.

4.2.3 Immobilization of Labeled Enzymes

Six different mMDH/CS/ACON solutions were prepared by mixing equal volume of enzyme stock solutions (5 mg/mL for each enzyme). The solutions were: AlexaFluor® 488-labeled mMDH mixed with nonlabeled CS and ACON (488-mMDH/CS/ACON, Solution **I**), AlexaFluor® 488-labeled ACON mixed with nonlabeled mMDH and CS (mMDH/CS/488-ACON, Solution **II**), AlexaFluor® 555-labeled CS mixed with nonlabeled mMDH and ACON (mMDH/555-CS/ACON, Solution **III**), AlexaFluor® 488-labeled mMDH and AlexaFluor® 555-labeled CS mixed with nonlabeled ACON (488-

mMDH/555-CS/ACON, Solution **IV**), AlexaFluor® 488-labeled ACON and AlexaFluor® 555-labeled CS mixed with nonlabeled mMDH (mMDH/555-CS/488-ACON, Solution **V**), and mixture of nonlabeled mMDH, CS and ACON (mMDH/CS/ACON, Solution **VI**). Thirty microliters of each mMDH/CS/ACON solution was mixed with each polymer solution (20 μL of 1% CHIT or BU-CHIT or ALA-CHIT solution, 7.5 μL of 10 mg/mL NF or TBAB-modified NF or TMOA-modified NF or TMODA-modified NF suspension, or 7.5 μL of 10 mg/mL LPEI or C8-LPEI suspension) at an enzyme/polymer molar ratio of about 2:1 to a final volume of 50 L, separately. Ten microliters of each enzyme/polymer suspension was drop-cast onto a microscopic cover glass slide (VWR) and dried at room temperature overnight. All fluorescent slides were stored in dark at 4 °C before use.

4.2.4 Fluorescent Imaging of Labeled Enzymes in Polymer Films

The fluorescent slides were imaged using a Nikon AIR laser scanning confocal microscope with a 20X objective. For regular images, samples were excited at 488 and 561 nm. For FRET images, samples were excited only at 488 nm. Two emission band filters (515/30 and 595/50) were used to detect the location of donors and acceptors in the polymers, respectively.

4.2.5 Steady-State FRET Spectroscopy

The emission spectra of labeled enzymes immobilized in polymers were collected by the fluorescence spectrophotometer. All slides were excited at 488 nm and fixed in a surface sample holder at an angel of 30° to minimize excitation light scattering. Each spectrum was collected from three scans on the same slide. Triplicate measurements on different slides were performed to generate the average emission spectrum. Nonlabeled slides (made from Solution **VI**) were scanned for background correction.

4.2.6 Acceptor Photobleaching FRET Imaging

The acceptor photobleaching was performed with the Nikon AIR laser scanning confocal microscopy by exposing the sample slides to a repeated excitation at 561 nm at its maximum power for 3 min. The time required for photobleaching was previously determined so that over 60% of acceptors were destroyed while unwanted bleaching of donors was minimized. Regular images and FRET images were collected before and after the photobleaching. Donor-only-labeled slides (**I** and **II**) were imaged for donor photobleaching correction. Acceptor-only-labeled slides (**III**) were imaged for acceptor cross-talk and bleaching photoproduct correction. Nonlabeled slides (**VI**) were imaged for background subtraction. FRET data were collected from three different photobleached regions on the slides.

4.2.7 FRET Calculations

Steady-state FRET efficiency, E_{ss}, was given by[1]

$$E_{ss}=\frac{F_D-F_{DA}}{F_D}=1-\frac{F_{DA}}{F_D}$$

where F_D and F_{DA} are the fluorescence intensities of the donors in the donor-only-labeled slides and double-acceptor-labeled slides, respectively. The average donor-acceptor separation, r_{ss}, was given by[1]

$$r_{ss}=R_0\left(\frac{1}{E_{ss}}-1\right)^{1/6}$$

For AlexaFluor®488- AlexaFluor®555, R_0 is 7.0 nm.

For the acceptor photobleaching results, all images for FRET data analysis were processed using the program *ImagJ* with a Java-built *AccPbFRET* plugin developed by

Roszik *et al.*[21], including image registration, background subtraction, image calculation and measurement. The pixel-by-pixel FRET efficiency, $E_{pb(i,j)}$, was determined by

$$E_{pb(i,j)}=1-\frac{(1-\alpha)\left(F^{0}_{D1(i,j)}-\delta F^{0}_{A1(i,j)}\right)}{\gamma\left(F^{0}_{D2(i,j)}-(\alpha\delta+(1-\alpha)\varepsilon)F^{0}_{A1(i,j)}\right)-\alpha\left(F^{0}_{D1(i,j)}-\delta F^{0}_{A1(i,j)}\right)}$$

where $F^{0}_{D1(i,j)}$ and $F^{0}_{D2(i,j)}$ are the uncorrected donor fluorescent intensities of the pixel (i, j) before and after photobleaching while $F^{0}_{A1(i,j)}$ is the uncorrected acceptor fluorescent intensity of the same pixel before photobleaching. α, γ, δ and ε are the acceptor partial photobleaching, donor photobleaching, acceptor crosstalk and acceptor bleaching photoproduct correction factors, respectively. The detailed procedure for determining all correction factors was already described in Roszik's paper[21]. The above equation can be further simplified to

$$E_{pb(i,j)}=\frac{F_{D2(i,j)}-F_{D1(i,j)}}{F_{D2(i,j)}-\alpha F_{D1(i,j)}}$$

by plugging in $F_{D1(i,j)}=F^{0}_{D1(i,j)}-\delta F^{0}_{A1(i,j)}$

and $F_{D2(i,j)}=\gamma\left(F^{0}_{D2(i,j)}-(\alpha\delta+(1-\alpha)\varepsilon)F^{0}_{A1(i,j)}\right)$

The pixel-by-pixel donor-acceptor separation, $r_{pb(i,j)}$, was given by

$$r_{pb(i,j)}=R_0\left(\frac{1}{E_{pb(i,j)}}-1\right)^{1/6}$$

4.2.8 Immobilized Enzyme Activity Assay

Diluted nonlabeled mMDH/CS/ACO solution was prepared by mixing equal volume of stock enzyme solutions (1 mg/mL). Sixty microliters of the enzyme solution was mixed with 40 μL of polymer suspension to an enzyme/polymer molar ratio of 1:2. After the sample was thoroughly mixed, a 90 μL aliquot was drop-cast onto the bottom of

the disposable cuvette and dried at 4ºC overnight. A 100 µL aliquot of the activation reagent (made by mixing 4 mL of 100 mM potassium phosphate buffer, 100 µL of 1 mM $Fe(NH_4)_2(SO_4)_2$ and 200 µL of 50 mM L-cysteine) was added to activate ACO at 0ºC for 1 h. Then a reaction cocktail composed of 50 µL of 0.5 mM acetyl-CoA, 250 µL of 50 mM β-NAD and 600 µL of 100 mM L-malate was added for the enzyme activity assays. All assay solutions were adjusted to pH 7.5. The UV absorbance at 340 nm, corresponding to the production of NADH, was recorded using a UV-Vis spectrometer every 1 min over a 5 min interval for calculating specific activities.

4.3 Results and Discussion

4.3.1 Co-Localization of mMDH, CS and ACO

Immobilized enzymes were once assumed to co-disperse throughout the polymer matrix uniformly. However, Konash *et al.* showed that enzyme distribution in solid-state polymer films was highly heterogeneous and reported discrete enzyme aggregates in polymer films[22]. The three enzymes might be co-localized to form metabolon or undergo homo-aggregation to form higher-ordered oligomers observed by Martin *et al.*[9]. Oligomerization may occur when transiently unfolded proteins precede self-assembly of polypeptide chains.[23] Hence, in different polymer media, the equilibrium between the unfolded and folded states of enzymes could shift, thereby resulting in different extent of oligomerization. By profiling the donor and acceptor fluorescence intensities along the diagonal line of each focal plane, we could qualitatively compare the degree of enzyme co-localization and self-aggregation.

As shown in Figure 4.3, most enzymes self-aggregated in both LPEI and C8-LPEI. This is indicated by peaks at 50 µm ~ 70 µm from 488-mMDH/555-CS in LPEI and peaks

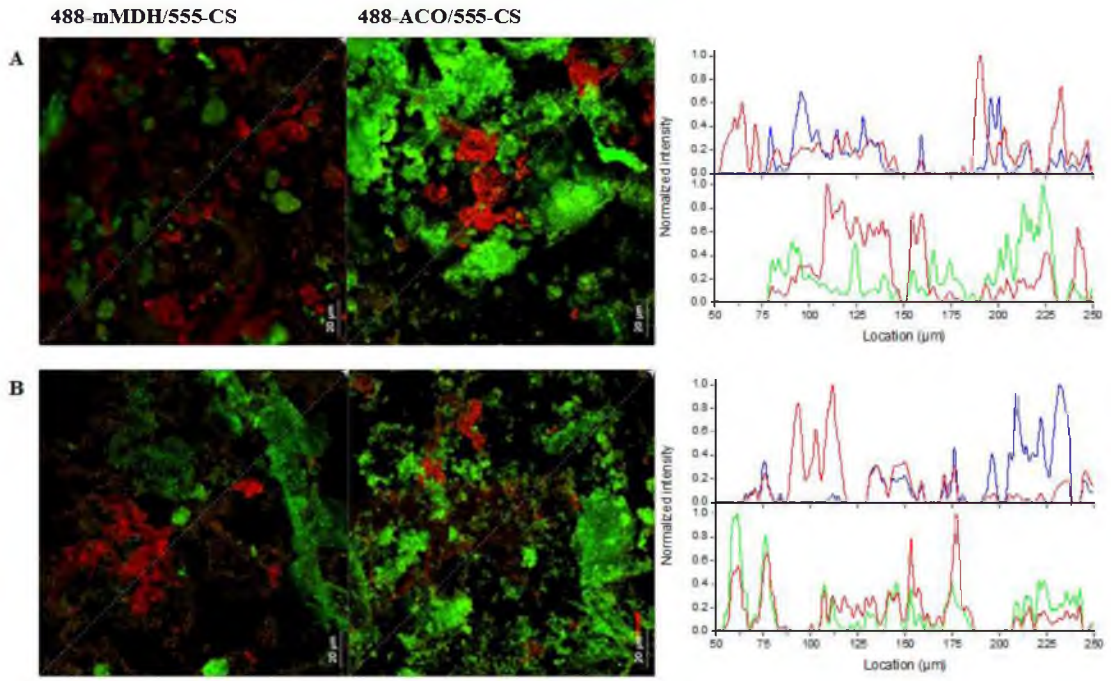

Figure 4.3 Merged fluorescence microscopic images of enzymes in LPEI (**A**) and C8-LPEI (**B**). 488 nm-excited donors (CS) are in **green pixels**) and 561 nm-excited acceptor (mMDH or ACO) are in **red pixels**. Intensity profiles on the right are achieved by plotting the grey values of 488-mMDH (**blue solid**), 488-ACO (**green solid**) and 555-CS (**red solid**) at each pixel along the diagonal line.

at 80 μm ~ 113 μm and 200 μm ~ 240 μm from 488-mMDH/555-CS in C8-LPEI. Large isolated clusters formed possibly due to enzyme-polymer backbone conjugation. On the other hand, Nafion polymers showed improved capability for enzyme immobilization. Highly overlapped emission spectra of donors and acceptors in all NF slides (Figure 4.4 and 4.5) implied the enzyme co-localization, although there was still some degree of self-aggregation in TMOA-NF. As good protein precipitating reagents, chitosan polymers can also conjugate tightly with enzymes, but unlike LPEI and C8-LPEI, we observed the co-immobilization of enzymes on a scaffold-like matrix (Figure 4.6) in either native chitosan polymer (CHIT) or modified chitosan polymer (BU-CHIT and ALA-CHIT). Compared to the other two, the network in ALA-CHIT was much denser and fewer intense clusters were seen in the images. According to intensity profiles, NF and CHIT polymers turned out to be a better immobilization platform for inducing enzyme co-localization than LPEI and C8-LPEI polymers, in which resulted enzymes were self-aggregated.

4.3.2 Multienzyme Aggregation State of mMDH/CS/ACO

Figure 4.7 illustrates the absence of FRET in single-type enzyme aggregates and occurrence of FRET caused by co-aggregation. Using steady state emission scan, we determined the multienzyme aggregation state in terms of average protein separations between donors and acceptors, which are summarized in Figure 4.8. Comparing LPEI and C8-LPEI slides, we did not find statistical differences in enzyme separations upon hydrophobic modification, which can be explained by extensive self-aggregation and polymer-enzyme conjugation in LPEI hydrogels. In Nafion polymers, it is significant that the separation decreased from plain NF to TMOA-NF. This is in agreement with why the encapsulation capability is improved greatly in TMOA modified Nafion, whose micelle

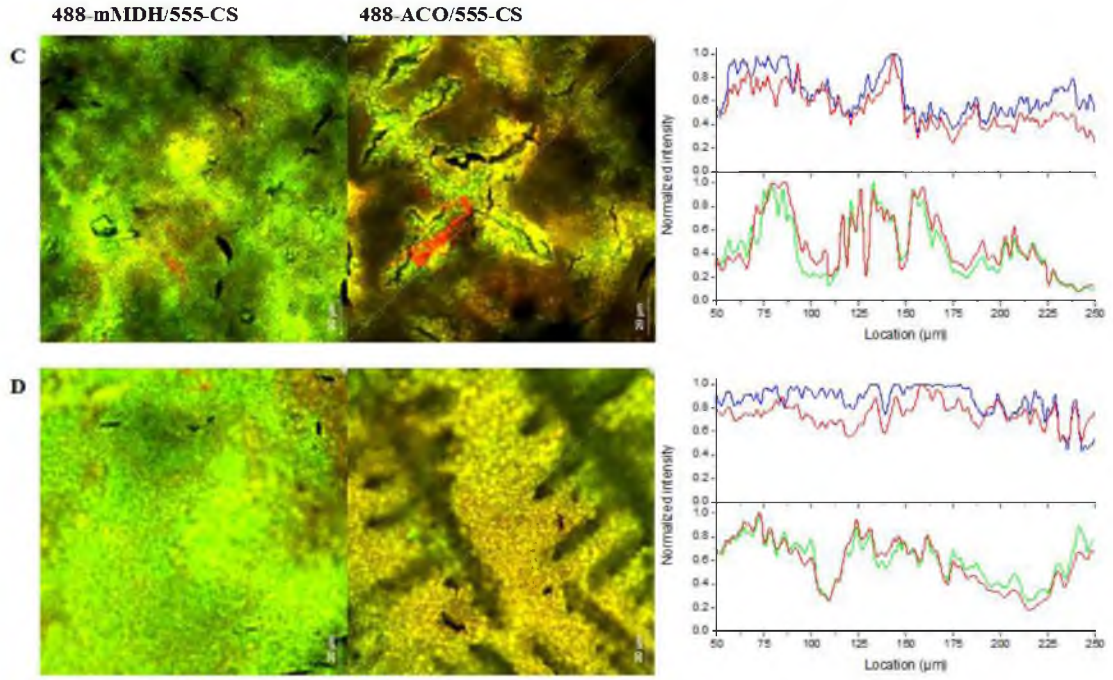

Figure 4.4 Merged fluorescence microscopic images of enzymes in plain NF (**C**) and TBAB-NF (**D**). 488 nm-excited donors (CS) are in **green pixels**) and 561 nm-excited acceptor (mMDH or ACO) are in **red pixels**. Intensity profiles on the right are achieved by plotting the grey values of 488-mMDH (**blue solid**), 488-ACO (**green solid**) and 555-CS (**red solid**) at each pixel along the diagonal line.

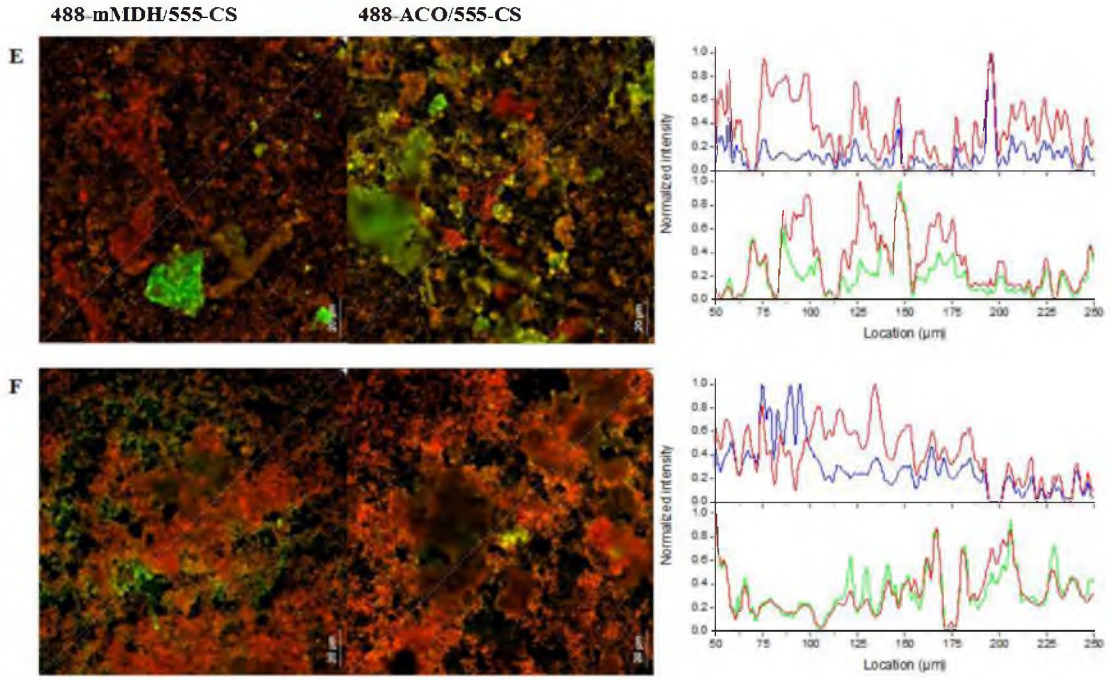

Figure 4.5 Merged fluorescence microscopic images of enzymes in TMOA-NF (**E**) and TMODA-NF (**F**). 488 nm-excited donors (CS) are in **green pixels**) and 561 nm-excited acceptor (mMDH or ACO) are in **red pixels**. Intensity profiles on the right are achieved by plotting the grey values of 488-mMDH (**blue solid**), 488-ACO (**green solid**) and 555-CS (**red solid**) at each pixel along the diagonal line.

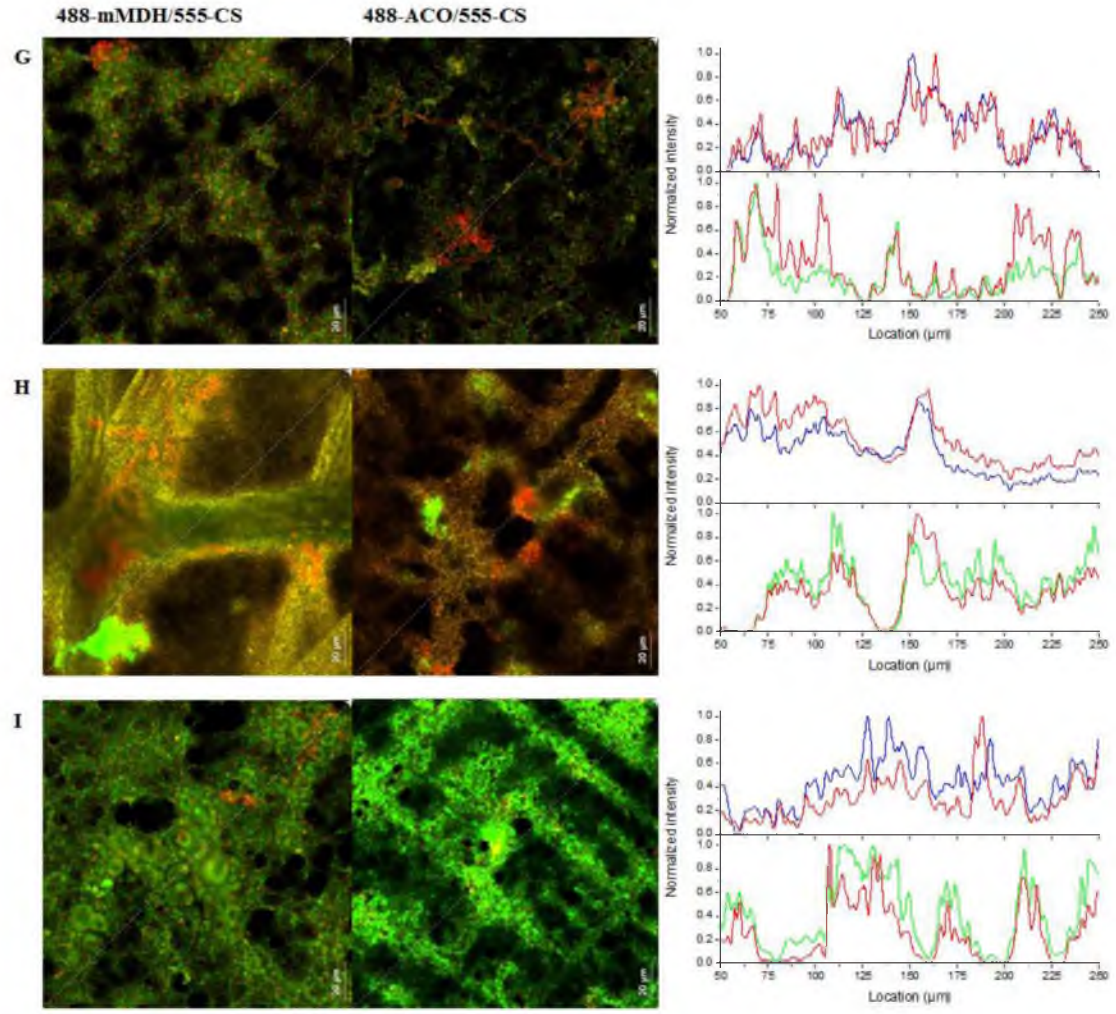

Figure 4.6 Merged fluorescence microscopic images of enzymes in native CHIT (**G**), BU-CHIT (**H**) and ALA-CHIT (**I**). 488 nm-excited donors (CS) are in **green pixels**) and 561 nm-excited acceptor (mMDH or ACO) are in **red pixels**. Intensity profiles on the right are achieved by plotting the grey values of 488-mMDH (**blue solid**), 488-ACO (**green solid**) and 555-CS (**red solid**) at each pixel along the diagonal line.

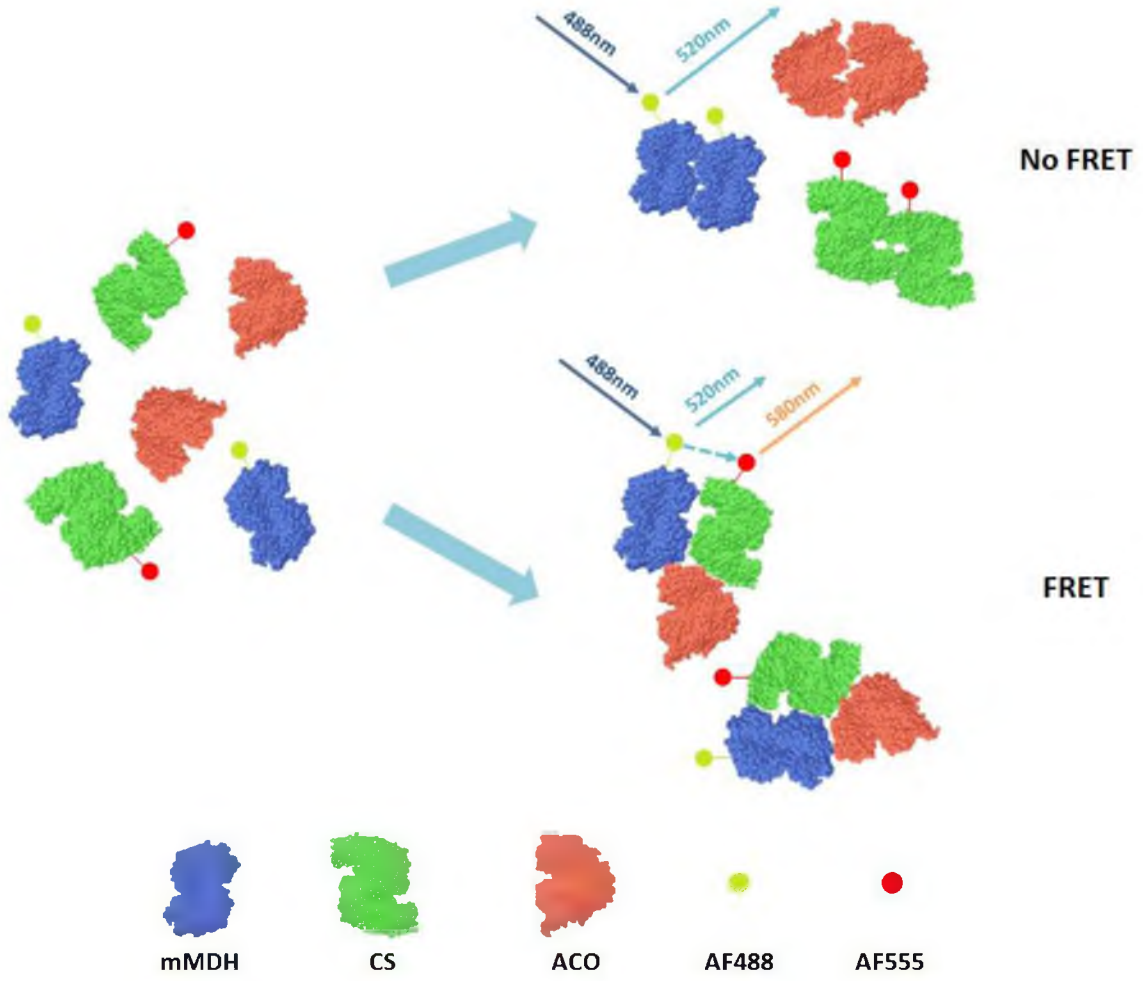

Figure 4.7 An illustration of self-enzyme aggregation and multi-enzyme aggregation induced by co-immobilization in polymers.

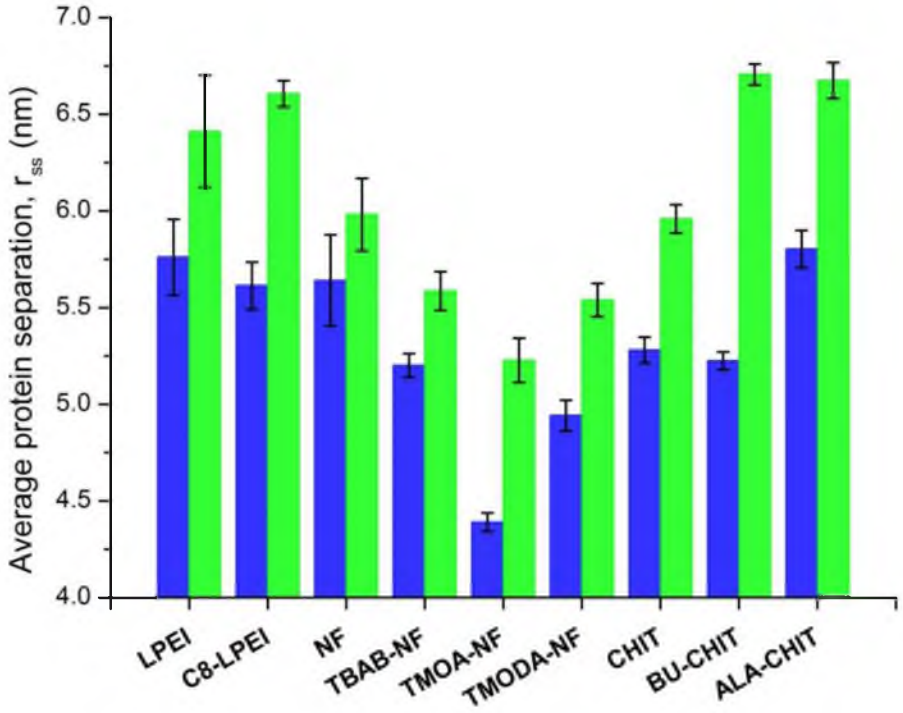

Figure 4.8 Calculated average enzyme separations from steady-state FRET efficiencies. mMDH-CS distances are represented by **blue columns** and CS-ACO distances are represented by **green columns** with standard deviations (**error bar**).

diameter was estimated to be more than 10 nm, compared to plain NF (~4 nm) and TBAB-NF (~6.5 nm).[24] Larger micelle size enables capture of larger enzymes, like ACO and CS, thereby facilitating the interaction between multiple partners. The situation is different in TMODA-NF, because no discernible micellar structures form as previously reported[24], so the encapsulation effect became trivial during immobilization and the separation increased slightly compared to TMOA-NF. In CHIT polymers, the trend was reversed, that is, the separations being larger in BU-CHIT and ALA-CHIT. As mentioned above, chitosan polymers can act as the polyconjugational 'cross-linkers', leading to formation of a stabilized multienzyme network. Hydrophobically modified chitosan polymers did not work as expected in increasing co-aggregation state, which is likely due to reduction of available ionic sites in the backbone of the polymer after alkylation.

4.3.3 Distribution of Distances in mMDH/CS/ACO Aggregates

Although we have obtained the average multi-aggregation state, detailed organization of enzymes was still unclear due to its heterogeneity throughout the polymer matrix. Enzymes might be in closer proximity in some regions than in others. The acceptor photobleaching method realized direct investigation of FRET at single sites in a region of interest (illustrated in Figure 4.9). By measuring the small increases in intensities from de-quenched donors, we determined the FRET efficiency at each site by pixel-by-pixel image calculations and finally the separation distribution throughout the imaged area. Typical image processing is shown in Figure 4.10.

As shown in Figure 4.11, enzyme separations in LPEI and C8-LPEI spanned a wide range, which is consistent with our intensity profiling results. Due to the tendency of enzymes to self-aggregation in a nonuniform manner, LPEI and C8-LPEI are not good

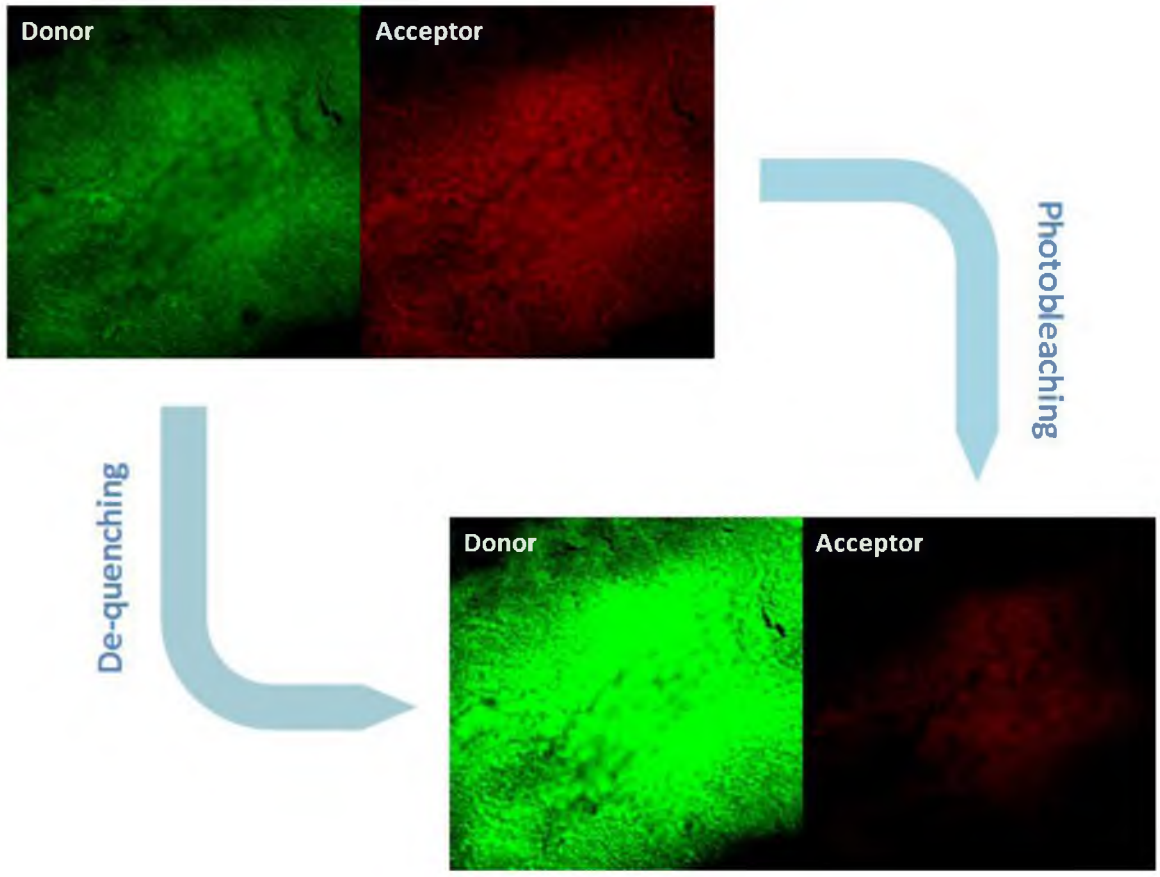

Figure 4.9 An illustration of partial acceptor photobleaching on TBAB-NF film with 488-mMDH/555-CS/ACO co-immobilized. Both donors and acceptors were excited at 488 nm.

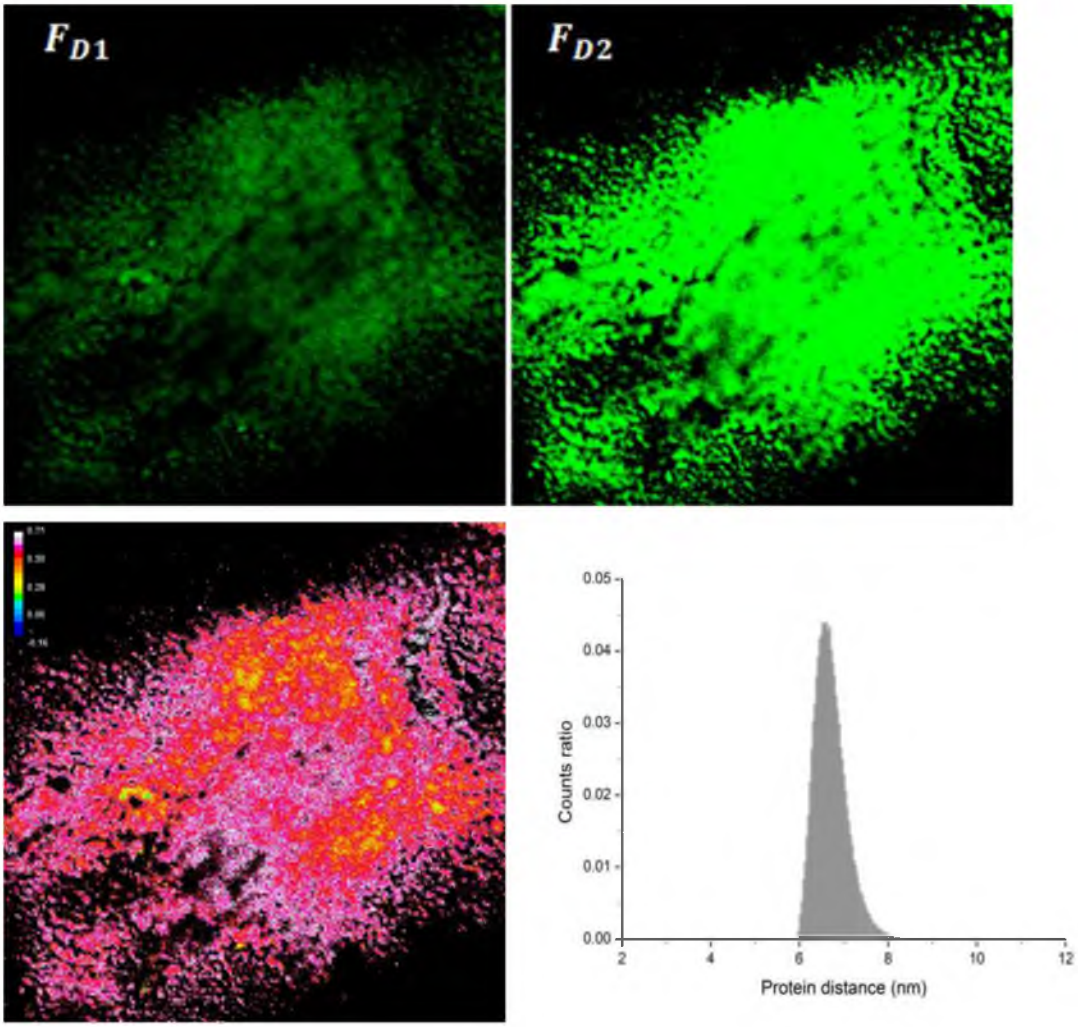

Figure 4.10 A set of acceptor photobleaching FRET images. $\boldsymbol{F_{D1}}$ and $\boldsymbol{F_{D2}}$ are corrected donor images (only excited at 488 nm) before and after bleaching. The FRET efficiency map (**bottom left**) was obtained using imaging calculation (the color bar on top left indicates the FRET efficiency) and then protein distance (**bottom right**) was counted pixel by pixel in the 512x512 efficiency image.

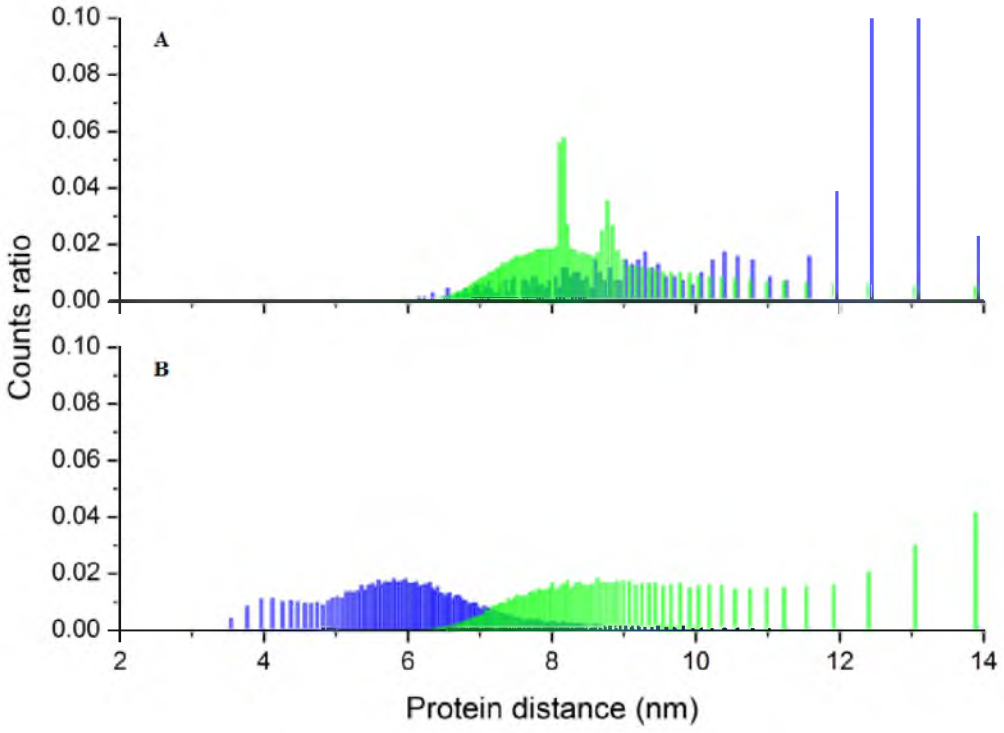

Figure 4.11 Distribution of protein distance between mMDH and CS (**blue column**) or ACO and CS (**green column**) in LPEI (**A**) and C8-LPEI (**B**).

candidates for building up a closely associated three-enzyme system. In NF polymers (Figure 4.12), r_{pb} distribution in mMDH/CS/ACO became narrower as the hydrophobicity increased. Plain NF has very uniform micellar structures with an average micelle pocket diameter of only 4 nm.[24] As a result, encapsulation would not be very efficient for all three enzymes and only a few mMDH were encapsulated. This might explain why the distribution band split (6.8 nm and 7.5 nm) for mMDH/CS and remained as one peak (6.6 nm) for ACO/CS. After modification with a hydrophobic ammonium cation, the confined micellar structure in native NF was altered. In TBAB-NF, the polymer micelles were expanded to an average of 6.5 nm.[24] The two r_{pb} distribution bands become significantly narrower and the split peak (7.5 nm for mMDH/CS in plain NF) disappeared, but their average values (6.7 nm for mMDH/CS and 6.4 nm for ACO/CS) did not differ much from those in plain NF. In this situation, probably most mMDH were encapsulated while the other two were still outside of the micelles. The r_{pb} bands become broader and split again in TMOA-NF. Unlike in plain NF, the two peaks for mMDH/CS were positioned at shorter distances, 5.5 nm and 6.8 nm. Separation of ACO/CS was distributed around 6.1 nm. As previously reported, micelles in TMOA-NF can be classified into three groups by sizes. Besides residual unmodified units that form micelles of 4 nm (like in plain NF), there are micelles of medium size (~10 nm) and large size (>20 nm).[24] Therefore encapsulation of one, two or even three enzymes could occur. Although no discernible micellar structure is evident in TMODA-NF, enzymes seemed to co-disperse in its matrix, which was supported by the fully overlapped narrow r distribution bands around 5.8 nm.

Results from chitosan polymers indicated the tradeoff between ionic binding and encapsulation again. ALA-CHIT exhibited a greater capacity for entrapping and stabilizing

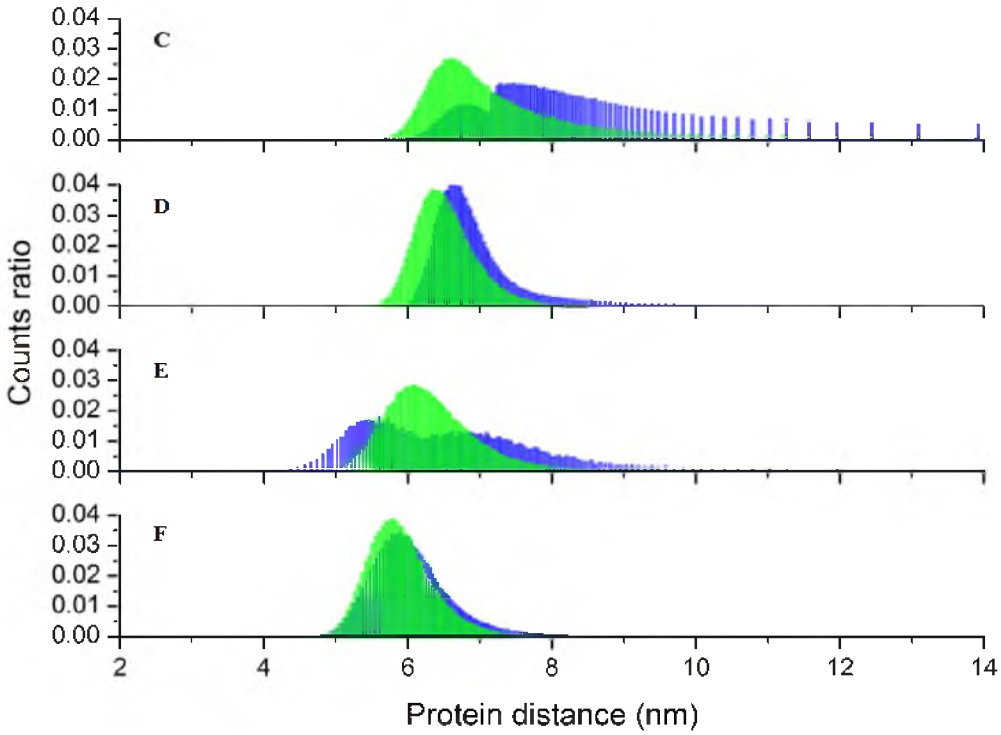

Figure 4.12 Distribution of protein distance between mMDH and CS (**blue column**) or ACO and CS (**green column**) in native NF (**C**), TBAB-NF (**D**), TMOA-NF (**E**) and TMODA-NF (**F**).

enzymes with long fatty acid side chains than butyl modified CHIT, even though BU-CHIT was found to be more hydrophobic.[19] As shown in Figure 4.13, enzyme distance distribution was the broadest in BU-CHIT, averaged around 6.7 nm (for mMDH/CS) and 7.9 nm (for ACO/CS). Comparing distribution bands in unmodified CHIT and ALA-CHIT, they looked very similar in shape but the average distances in native CHIT were a bit shorter. This was possibly due to the fact that only a very small fraction of backbone amines were substituted by ALA under exploited conditions so that the microenvironment in ALA-CHIT did not vary a lot from native CHIT, but the substitution still caused some loss of its 'cross-linking' effect.

It is worth mentioning here that the steady-state FRET and acceptor photobleaching FRET were inconsistent on the average protein separation in some polymers. For example, r in TMODA-NF is larger than in TMOA-NF using steady-state FRET but smaller using acceptor photobleaching FRET. The latter technique should be more reliable in this work, because extensive self-aggregation would also cause self-quenching of donors.

4.3.4 Immobilized Single Enzyme Activity

Catalytic performance of immobilized mMDH was evaluated as to compare the effect of immobilization on single enzyme activity. In Figure 4.14, there was a clear trend showing that enzyme activity increased upon hydrophobic modification of polymers, especially NF and CHIT polymers. In plain NF, the sulfonic acid side chain of the polymer was fully protonated, which deactivated the enzymes. By replacing the protons with alkylammonium, its acidic microenvironment was buffered and deactivation was reduced, proved by the drastic increase in activities of enzymes in modified NF. As alkyl chains expanded, activity reached a maximum in TMOA-NF and TMODA-NF. In chitosan

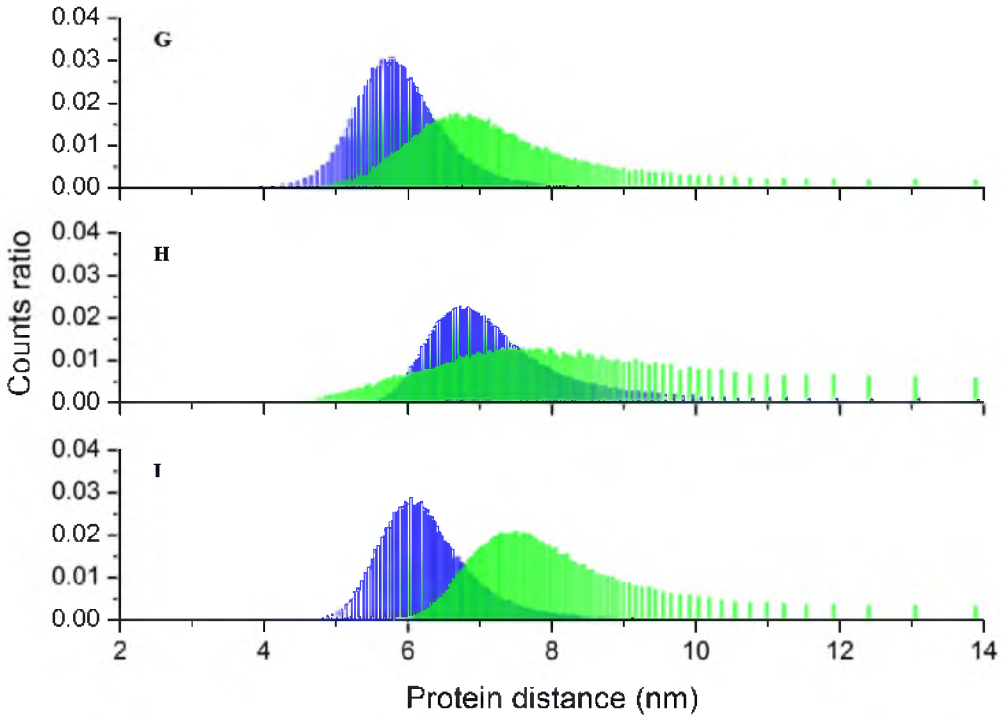

Figure 4.13 Distribution of protein distance between mMDH and CS (**blue column**) or ACO and CS (**green column**) in native CHIT (**G**), BU-CHIT (**H**) and ALA-CHIT (**I**).

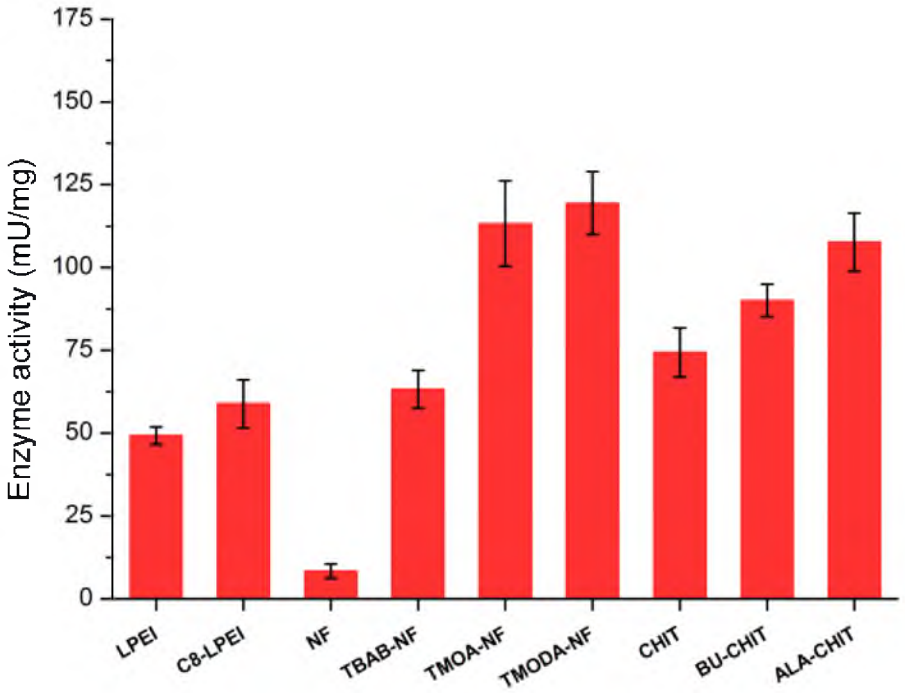

Figure 4.14 Specific activity of immobilized mMDH in different polymer films.

polymers, the enzyme activity increased consistently from native CHIT to ALA-CHIT. Extensive ionic 'cross-linking' may block the active sites of enzymes in plain CHIT. Alkyl substitution reduced such risk and introduced an amphiphilic microenvironment to improve enzyme performance.

4.4 Conclusions

In this chapter, aimed at selecting the suitable polymer materials for co-immobilization of enzyme cascades, FRET microscopy, especially acceptor photobleaching FRET technique, has been shown as a powerful tool in mapping the heterogeneous enzyme associations in solid-state matrices, and interactions between three TCA cycle enzymes in commonly used polymers for electrode fabrication have been quantitatively investigated. Through direct investigation of immobilized enzymes using fluorescent imaging, linear polyethylenimine and octyl modified linear polyethylenimine have been excluded from potential co-immobilization matrices due to single enzyme self-aggregation rather than multienzyme complex formation. By measuring the apparent energy transfer efficiency with FRET spectroscopy, the average enzyme distances have been determined to show that high multienzyme aggregation state (shortest distance) can be achieved in TMOA-NF and TMODA-NF. With acceptor photobleaching FRET microscopy, TMODA-NF has been demonstrated as the best potential platform for the TCA cycle metabolon biomimic with the most uniform enzyme separation among all the tested polymers. Although chitosan polymers did not induce much enhancement on multienzyme aggregation during FRET experiments, they are still good biocompatible templates for further functionalization. Moreover, efficient substrate/product transport

through the macroporous chitosan scaffolds is another significant advantage in promoting sequential catalysis.

4.5 References

(1) Gryczynski, Z.; Gryczynski, I.; Lakowicz, J. In *Molecular Imaging: FRET Microscopy and Spectroscopy*; Periasamy, A., Day, R. N., Eds.; Oxford Unversity Press, Inc: New York, **2005**, p 21.

(2) Kenworthy, A. K. In *Molecular Imaging: FRET Microscopy and Spectroscopy*; Periasamy, A., Day, R. N., Eds.; Oxford University Press, Inc.: New York, **2005**, p 146.

(3) Araiza-Olivera, D. In *Cell Metabolism: Cell Homestasis and Stress Response*; Bubulya, P., Ed.; InTech: Rijeka, **2012**, p 101.

(4) Haggie, P. M.; Verkman, A. S. *J. Biol. Chem.* **2002**, *277*, 40782.

(5) Kozer, N.; Kuttner, Y. Y.; Haran, G.; Schreiber, G. *Biophys. J.* **2007**, *92*, 2139.

(6) Mattiasson, B.; Johansson, A.-C.; Mosbach, K. *Eur. J. Biochem.* **1974**, *46*, 341.

(7) Srere, P. A.; Mattiasson, B.; Mosbach, K. *Proc. Nat. Acad. Sci. U. S. A.* **1973**, *70*, 2534.

(8) Schoffelen, S.; van Hest, J. C. M. *Soft Matter* **2012**, *8*, 1736.

(9) Martin, G. L.; Minteer, S. D.; Cooney, M. *Chem. Commun.* **2011**, *47*, 2083.

(10) Moehlenbrock, M. J.; Meredith, M. T.; Minteer, S. D. *MRS Commun.* **2011**, *1*, 37.

(11) Tauhardt, L.; Kempe, K.; Knop, K.; Altuntaş, E.; Jäger, M.; Schubert, S.; Fischer, D.; Schubert, U. S. *Macromol. Chem. Phys.* **2011**, *212*, 1918.

(12) Schrenk, M. J.; Villigram, R. E.; Torrence, N. J.; Brancato, S. J.; Minteer, S. D. *J. Memb. Sci.* **2005**, *205*, 3.

(13) Zook, L. A.; Leddy, J. *Anal. Chem.* **1996**, *68*, 3793.

(14) Moore, C.; Hackman, S.; Brennan, T.; Minteer, S. *J. Memb. Sci.* **2005**, *254*, 63.

(15) Peniche, C.; Argüelles-Monal, W.; Peniche, H.; Acosta, N. *Macromol. Biosci.* **2003**, *3*, 511.

(16) Martin, G. L.; Ross, J. A.; Minteer, S. D.; Jameson, D. M.; Cooney, M. J. *Carbohydr. Polym.* **2009**, *77*, 695.

(17) Klotzbach, T.; Watt, M.; Ansari, Y.; Minteer, S. *J. Memb. Sci.* **2006**, *282*, 276.

(18) Sjoholm, K. H.; Cooney, M.; Minteer, S. D. *Carbohydr. Polym.* **2009**, *77*, 420.

(19) Martin, G. L.; Minteer, S. D.; Cooney, M. J. *ACS Appl. Mater. Interfaces* **2009**, *1*, 367.

(20) Watt, M. M.; Minteer, S. D. *Polym. Mater. Sci. Eng.* **2006**, *94*, 601.

(21) Roszik, J.; Szollosi, J.; Vereb, G. *BMC Bioinformatics* **2008**, *9*, 346.

(22) Konash, A.; Cooney, M. J.; Liaw, B. Y.; Jameson, D. M. *J. Mater. Chem.* **2006**, *16*, 4107.

(23) Dima, R. I.; Thirumalai, D. *Protein Sci.* **2002**, *11*, 1036.

(24) Menius, C. E.; Arechederra, R. L.; Minteer, S. D. *Polym. Mater. Sci. Eng.* **2009**, *100*, 625.

CHAPTER 5

THE ARTIFICIAL TCA CYCLE METABOLON WITH ENHANCED SUBSTRATE CHANNELING

5.1 Background and Motivation

5.1.1 Protein Engineering in Artificial Metabolon Design

In designing metabolic compartmentation for *in vitro* applications, protein engineering is advantageous in manipulating the structure and function of enzymes. With a variety of engineering strategies reviewed in Chapter 1, different architectures can be achieved in artificially assembled enzyme cascades.[1-9] Generally, the approach is introducing an attachment, substitution, insertion or deletion to the sites of interest in wild-type (WT) enzymes through recombinant DNA technology or other sophisticated methods. Mutated enzymes are then scaffolded, fused or automatically associated into supramolecular structures through interactions between affinity domains and corresponding ligands.[3,10-13] From the study discussed in Chapter 4, we have realized that polymeric co-immobilization of multiple enzymes is quite limited in directing their spatial organization. On the other hand, protein engineering provides a wide range of options for creating a "smarter" system in which the enzyme association is guided with controllable order, stoichiometry or structure orientation and improved robustness.

Another longstanding goal of engineered multienzyme assembly goes to facilitated mass transport, which makes the artificial system a real metabolon. For this purpose,

considerable efforts have been devoted to realizing natural occurrence *in vitro* by mimicking the native metabolic organization. In other words, this requires the knowledge of protein-protein interactions in native states, including the three-dimensional complex structure, interfacial residues or domains and possible conformational changes upon association.

Among already mentioned methods, posttranslational, selective enzyme conjugation turns out to be the most appealing method.[14] In this case, modified enzymes can be separately expressed and undergo directed association *in vitro*. Site-specific incorporation of nonnatural amino acids functionalized with photoreactive moieties enables selective and orthogonal conjugation under light irradiation.[5] UV-irradiated cross-linking can be similarly carried out between a benzophenone-tagged protein and a transglutaminase recognition sequence-fused protein.[15] Due to uniqueness in chemical reactivity and sequence location, N- and C-terminus have stood out as extraordinary targets in single-site modification by either chemical reagents or genetic fusion, and many elegant multienzyme systems featuring substrate channeling have been achieved from terminal-directed association.[16-20]

5.1.2 Structure-Based Design of the mMDH-CS Metabolon

As part of the TCA cycle metabolon, mMDH and CS can associate dynamically in even dilute solution. However, this interaction might proceed in a random manner. To reconstruct the mMDH-CS metabolon *in vitro*, we would need to place some restrictions on protein-protein interactions, so that they can form desired products. Finally, we chose to introduce two different peptide tags to the N- and C-terminus of each enzyme. The FLAG-tag fused to N-terminus is a hydrophilic, eight-amino acid peptide (DYKDDDDK),

which selectively binds the monoclonal antibodies M1, M2 and M5. The hex His-tag fused to C-terminus is a short affinity tag consisting of six histidines (HHHHHH). Since the histidine imidazole ring can coordinate firmly to transition metal ions (Ni^{2+}, Co^{2+}, Cu^{2+}, and Zn^{2+}), polyhistidine-tagged proteins can be tethered to a transition metal-modified matrix.[10]

According to the three-dimensional structure of the natural TCA cycle metabolon derived from XL-MS and protein docking, N- and C-terminus of CS and C-terminus of mMDH are not buried in but positioned around the mMDH-CS interface. The other two N-terminus of mMDH point almost perpendicularly to the interface towards the opposite direction. Inspired by this conformation, we adopted the terminal-tagging strategy primarily based on the hypothesis that extended peptide tags on all terminus in this case would not interfere with intended interface formation but limit unwanted interactions at other surface regions, as surface complementarity is altered. Secondly, affinity tags on terminus would not deactivate enzymes as active sites are typically folded inside. The last but not the least, affinity peptide-tagged mMDH-CS complex can be used for oriented immobilization onto antibody- or transition metal-modified scaffolds or electrode surfaces in future development.

5.1.3 Stopped-Flow Method for Fast Enzyme Kinetics

Stopped-flow method refers to fast injection of a substrate solution and an enzyme solution into a small chamber or well, which is suddenly stopped after the desired volume is reached in a few miliseconds. Immediately upon stopping, detectors start to measure the product forming by UV-Vis absorbance or fluorescence emission change at very short time intervals. The stopping time may be varied to allow rate measurement at different reaction

phases. Compared to conventional mixing by hand, stopped-flow is much more consistent in mixing time and sensitive to reduced small-volume (up to hundreds of microliters) reactions. Therefore, in study of fast enzyme kinetics, stopped-flow method is a powerful technique in determining short transient time at millisecond scale.[21]

5.1.4 Aims

To our knowledge, little work has been done so far on an artificial TCA cycle metabolon, except the fusion mMDH-CS complex made by the Srere group nearly 20 years ago.[22,23] Besides hybridizing the two enzymes by fusing the termini together, now we may engineer a complex retaining the naturally occurring structure and featuring substrate channeling. In this work, we combined site-specific modification with XL-MS and protein docking again, and structurally evaluated the engineered mMDH-CS complex. Furthermore, substrate channeling in the artificial metabolon was characterized from a kinetic perspective.

5.2 Experimental

5.2.1 Materials

Potassium phosphate was purchased from EMD chemicals. NAD^+ was purchased from Research Products International. DSG was purchased from Life Technologies. All other chemicals were purchased from Sigma-Aldrich unless otherwise specified. WT heart mMDH, CS and aspartate aminotransferase (AAT) were purchased from Sigma-Aldrich in ammonium sulfate suspensions. WT heart ACO was purchased from Sigma-Aldrich as lyophilized powder. Recombinant heart mMDH, CS and ACO including site-directed mutated (nonterminal site) CS were synthesized and purified by Dr. Scott A. Banta and his colleagues. Ala-chitosan was prepared as already described in Section 4.2.2.

5.2.2 *In Vitro* Chemical Cross-Linking of mMDH and CS

WT and recombinant enzymes were cleaned up by a prepacked Sephadex^{TM,} G-25M column (GE Healthcare) to remove ammonium sulfate and other salts containing primary amine. Then mMDH, CS and ACO were mixed equally to a total protein concentration at 2 mg/mL in 10 mM PBS (pH 7.4). DSG (Life Technologies) dissolved in 50 μL of DMF was added to enzyme mixture to a final concentration of 1 mM. The approximate DSG/protein molar ratio was 50:1. As non-cross-linked control, 50 μL of DMF containing no DSG was added. Cross-linking was incubated at room temperature for 30 min under gentle shaking and quenched by adding 2 M Tris buffer (pH 8.3) to a final concentration of 20 mM.

5.2.3 Separation of the mMDH-CS Complex

Enzyme mixtures were washed with 50 mM Tris buffer (pH 7.4) in filter-incorporated Amicon tubes with a mass cutoff at 10 kDa (Millipore) at 5000 × g for 15 min to remove phosphates and extra DSG. Then cross-linked and non-cross-linked samples were directly separated by reducing SDS PAGE, which was performed on a 4-20% gradient gel (Thermo Scientific) according to the protocol provided by manufacturer.

5.2.4 Structural Determination of the mMDH-CS Complex and Simulation of Electrostatic Channeling

Identification of non-cross-linked and cross-linked peptides by in gel typsin digestion and mass spectrometry (including instrumentation and data analysis) was done as described in Section 3.2.5-3.2.8. Structure solving by hybrid protein docking was done as described in Section 3.2.9. Calculation of surface ESP was done as described in Section 3.2.10 with pH set to 7.4.

5.2.5 Competing Experiment with Aspartate Aminotransferase (AAT)

Equal amounts of WT/recombinant mMDH and CS were mixed in 10 mM PBS (pH 7.4) to a final total protein concentration of 20 μM, and incubated under gentle shaking at room temperature for 30 min, followed by dilution to 4 μM in same PBS buffer. Then 100 μL of the enzyme mixtures were mixed with 50 μL of ala-chitosan (10 mg/mL), and incubated on vortex at 800 rpm for 15 min. To the bottom of each polystyrene cuvette, 25 μL of the enzyme-polymer suspension was drop-cast and let dry in a vacuum at room temperature for 2 h. Once dried, immobilized enzymes were assayed in a cocktail in 100 mM potassium phosphate buffer (pH 7.4): 1 mM L-malate, 2 mM NAD^+, 0.1 mM acetyl-CoA, 0.2 mM DTNB, 10 mM L-glutamate and 1 U/mL AAT. Absorbance at 412 nm was monitored every 1 s over 5 min.

5.2.6 Transient Time Measurement by Stopped-Flow Method

Stopped-flow experiment was carried out in a 96-well plate measured by a Synergy™ HTX multimode microplate reader (BioTek) equipped with a dual injection module. Before assays, 10 μL of WT/recombinant mMDH (20 μM) and 10 μL of WT/recombinant CS (20 μM) were mixed in 10 mM PBS (pH 7.4) and incubated under gentle shaking at room temperature for 30 min, followed by dilution to 2 mL in 100 mM potassium phosphate buffer (pH 7.4). In total three mixtures were prepared: WT mMDH-CS, recombinant mMDH-CS and recombinant mMDH-CS (Arg65 mutated to Ala65). No cross-linker was added during this step as to avoid any potential deactivation. Substrate solution was prepared in 2 mL of potassium phosphate buffer containing 2 mM L-malate, 4 mM NAD^+, 0.2 mM acetyl-CoA and 0.4 mM DTNB. To setup the assay condition, enzyme and substrate solutions were respectively injected by two separate syringes at a

flow rate of 250 μL/s. Total assay volume was 200 μL/s per well (light path length was 0.56 cm). Absorbance at 412 nm was read every 90 ms over 1 min.

5.3 Results and Discussion

5.3.1 Formation of the mMDH-CS Complex *In Vitro*

In vitro cross-linking of mMDH-CS interactions was done together with ACO as to simulate the situation in the natural metabolon. As shown in Figure 5.1, intense protein bands appeared near the starting wells after cross-linking, indicating the formation of large aggregates, in which mMDH, CS and ACO were all identified by mass spectrometry. In mitochondria, cross-linking of all the TCA cycle enzymes *in situ* generated a huge complex. Being different in solution, the three enzymes would have more freedom to assemble into higher-ordered complexes, which might be the association of enzyme oligomers, or the aggregation of mMDH-CS-ACO complexes.

5.3.2 Structural Comparison of WT/Recombinant mMDH-CS Complexes to the Natural Metabolon

As previously mentioned, interactions between WT mMDH and CS in dilute solution can occur at random regions, which are shown in Figure 5.2. A number of docked models were found to meet our selection criteria (detailed in Section 3.2.9). Each model exhibited quite distinct conformation orientation and interface from the others. Among them, one candidate (highlighted in the red square) showed up as the most promising structure. In the case of recombinant enzymes, protein-protein interactions appeared relatively simple. According to mass spectrometric identification and protein docking, only one structure was found and its conformation orientation looked very similar to that of the natural metabolon. A structural comparison is illustrated in Figure 5.3. In the WT complex,

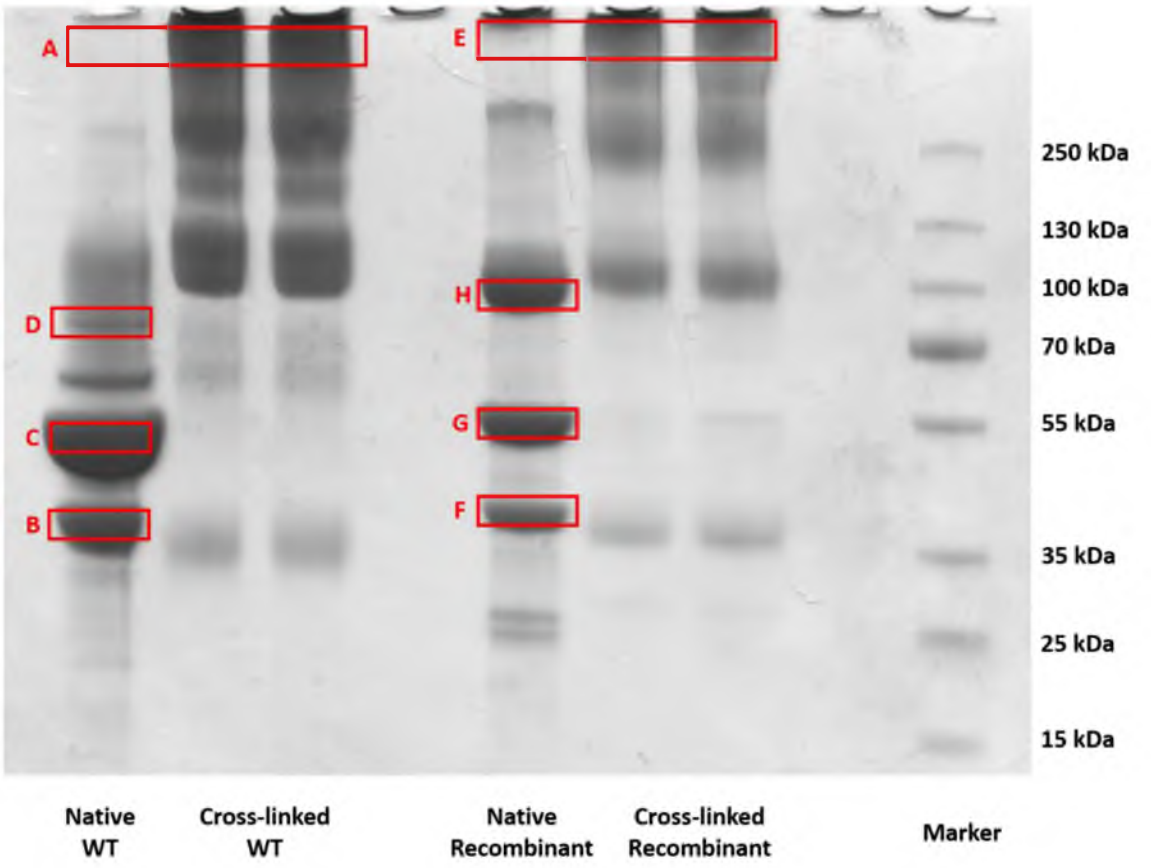

Figure 5.1 Reducing SDS-PAGE of cross-linked and native (non-cross-linked) mMDH-CS-ACO complex *in vitro*. Bands in red squares were cut for digestion and mass spectrometric analysis: (A) cross-linked large WT mMDH-CS-ACO complex, (B) native WT mMDH subunit, (C) native WT CS subunit, (D) native WT ACO, (E) cross-linked large recombinant mMDH-CS-ACO complex, (F) native recombinant mMDH subunit, (G) native recombinant CS subunit, (H) native recombinant ACO.

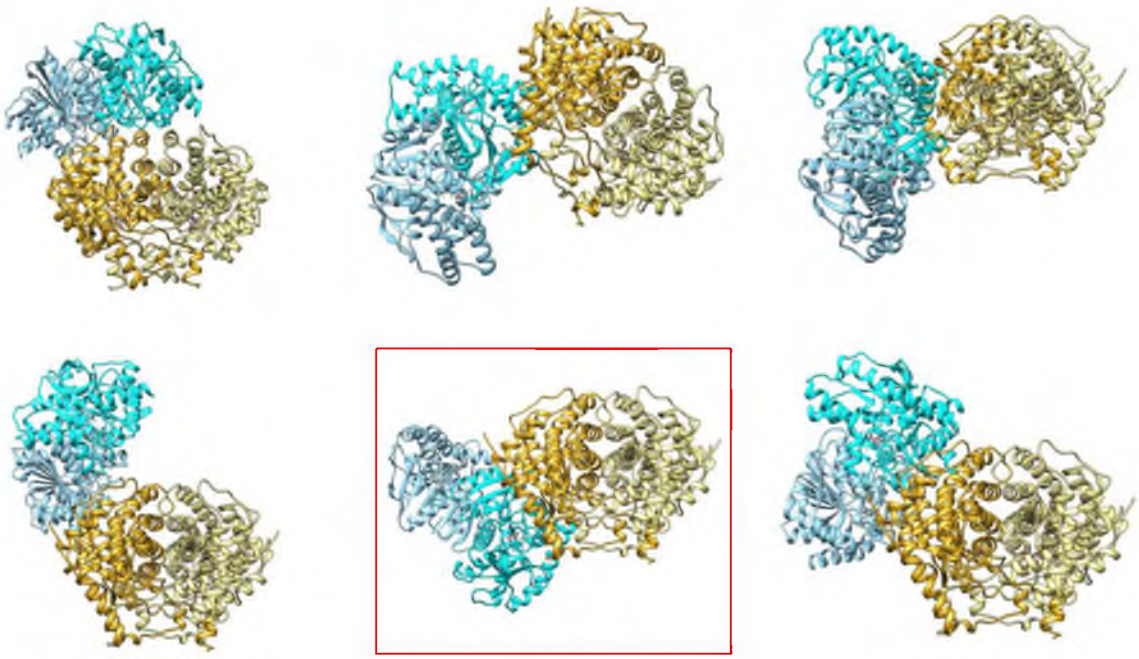

Figure 5.2 List of all possible docked structures for the WT mMDH-CS complex. The two chains of CS are colored in goldenrod and khaki. The two chains of mMDH are colored in sky blue and cyan. The most promising structure is highlighted by the red square.

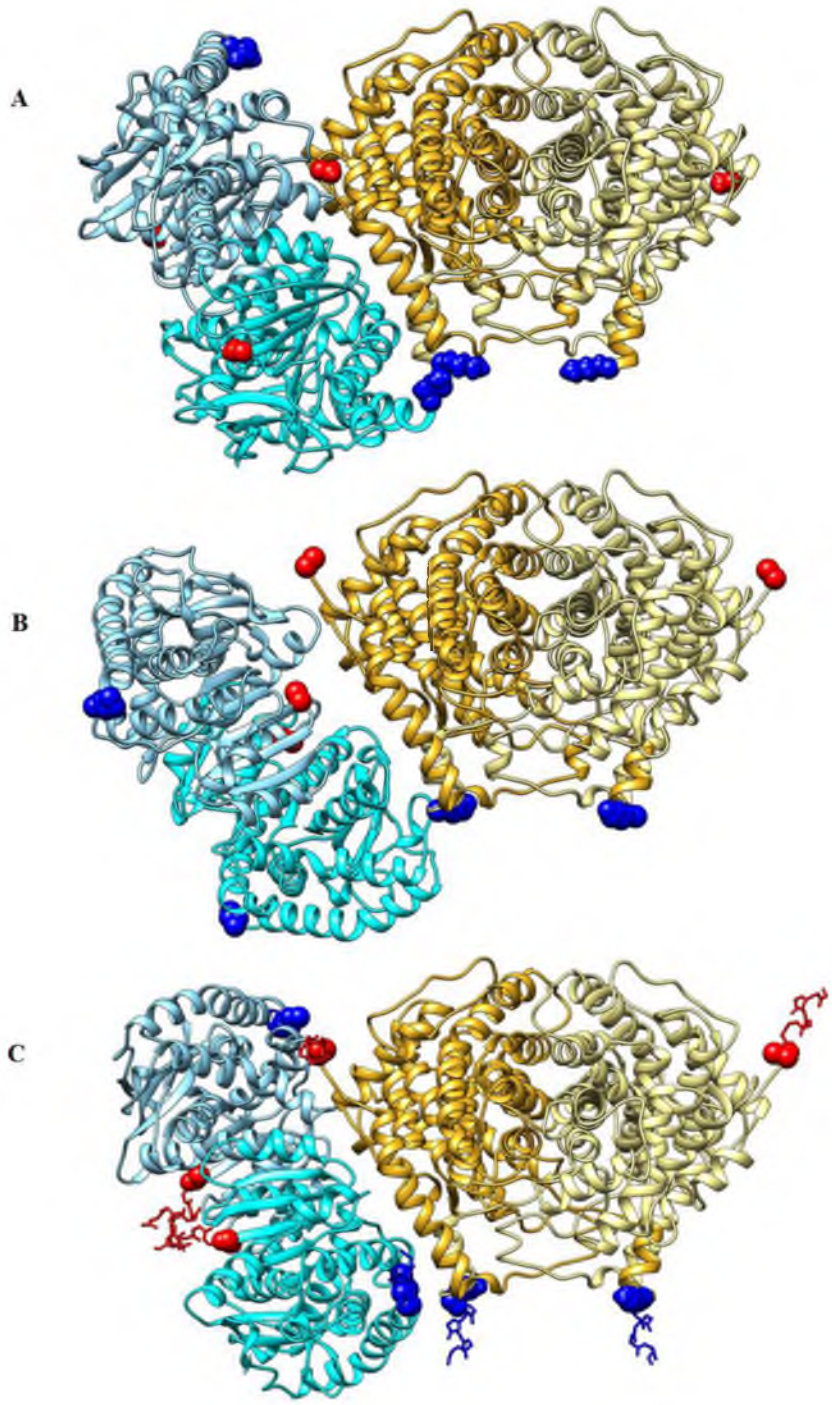

Figure 5.3 Docked structures of the natural TCA cycle metabolon (**A**), *in vitro* WT mMDH-CS complex (**B**) and recombinant mMDH-CS complex (**C**). N-terminus are represented by red spheres. C-terminus are represented by blue spheres. FLAG-tags are represented by red sticks. HexHis-tags are represented by blue sticks.

mMDH was flipped by approximately 180 degrees around the axis parallel to the original interface in natural metabolon, and consequently its two N-terminus were buried between enzymes. Meanwhile, all the other terminus went away from the interface. This flipping might be unfavorable for directed OAA transport, because the clefts between two subunits where L-malate and OAA are accommodated were now open to the bulk solution. The average distance between active sites was also increased from 35 Å in the natural metabolon to 73 Å.

In contrast to the WT complex, the recombinant complex exhibited some rational behavior in dilute solution. Although mMDH rotated around the axis perpendicular to the interface by approximately 30 degrees, the final structure maintained most of the natural features. First of all, no terminus were buried in the interface due to the spatial hindrance from additional tags at surface. Secondly, relative locations of terminus around the interface were not significantly altered. Thirdly, the two tagged N-terminus of mMDH were still extending into the open space. More importantly, the active site clefts in mMDH were facing towards CS not the bulk solution, and the average distance between active sites was only 40 Å. It is worth mentioning that the interface area in the recombinant mMDH-CS complex was 12100 $Å^2$, suggesting that it may be more thermodynamically stable than either the natural metabolon (10000 $Å^2$) or the WT complex (11300 $Å^2$).

5.3.3 Proof of Enhanced OAA Channeling in the Recombinant mMDH-CS Complex

Slightly different from the simulation for natural metabolon at pH 7.8, the pH value used for calculation of surface ESP of the mMDH-CS complex in solution was set at 7.4, which was the medium pH. As depicted in Figure 5.4, positively charged continuous bands

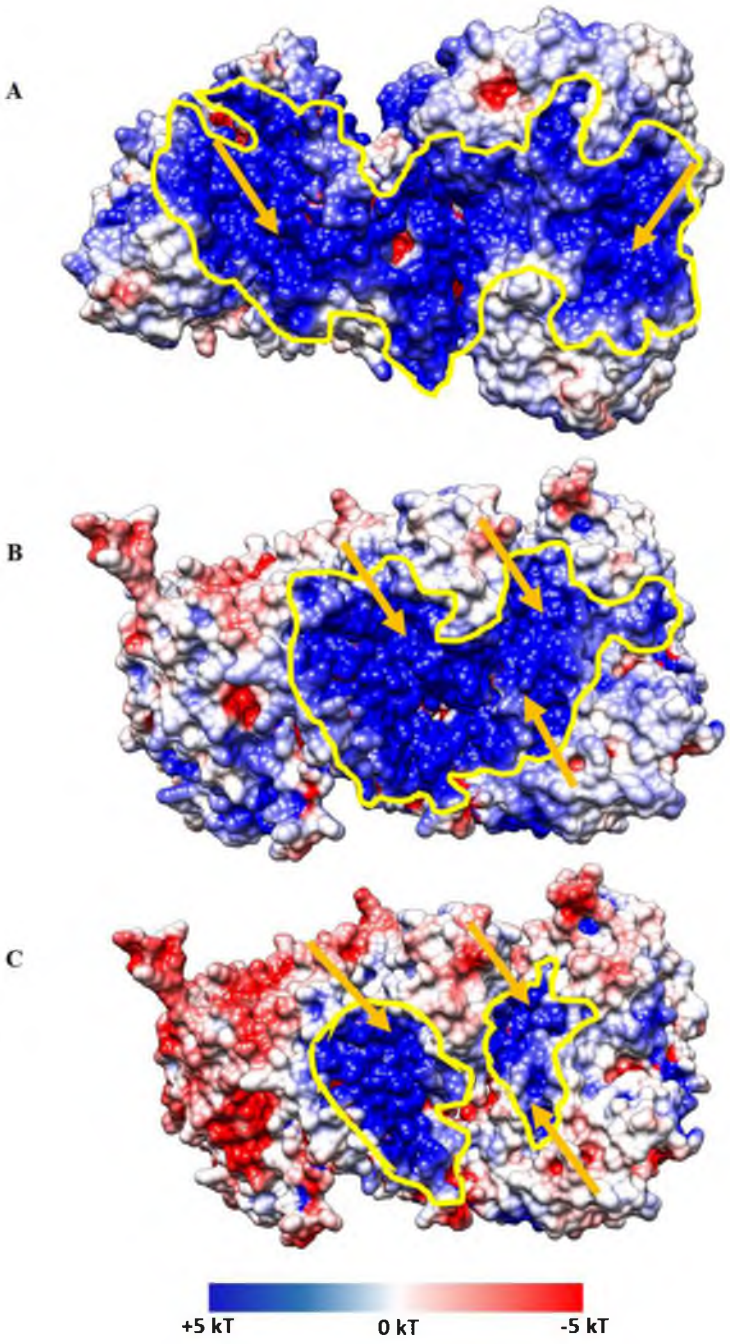

Figure 5.4 Simulated electrostatic channeling in the WT (**A**), recombinant (**B**) and arginine-mutated (**C**) mMDH-CS complex. Calculation of surface ESP was done at pH 7.4. Active sites are denoted by orange arrows and electrostatic channels are highlighted by yellow edges. Negatively charged, positively charged and neutral regions are colored in red, blue and white.

formed across the binding interfaces in both WT and recombinant complexes. In the WT complex, the band was quite long and broad with the majority of one side surface covered. Although flipping of mMDH increased the distance between active sites, OAA channeling may still happen within the positively charged pathway. In the recombinant complex, the band area was significantly smaller, only encompassing the active site clefts and binding interface. This is definitely favored by the restricted orientation of tagged enzymes. With a shorter channeling length, transport of OAA in the recombinant mMDH-CS complex would be faster than in the WT complex.

To prove the simulated kinetic advantage in the engineered metabolon, competing experiment was done in the presence of AAT, which catalyzes the reversible conversion of OAA and L-glutamate to aspartate and α-ketoglutarate. As illustrated in Figure 5.5, in a free-floating system, OAA diffusing into the bulk phase will be captured by AAT, thus resulting in reduced coupled mMDH-CS activity and production of citrate. If OAA is directly channeled, the coupled catalysis will not be influenced by the presence of AAT. In this work, ala-chitosan was utilized to localize the mMDH-CS complex and avoid the probable interactions between mMDH and AAT. For the WT complex, coupled activity decreased by about 30% after 1 U/mL of AAT was added, but for the recombinant complex, it only decreased by 15%, showing that the transport of OAA was less affected by the competitive enzyme (Figure 5.6). However, it should be noted that even in the engineered complex, substrate channeling was not perfect in preventing leaking of intermediates. This might be inevitable in dynamic metabolons, since the intermediate has to dissociate from enzymes. Potential interactions between mMDH and AAT could not be completely ruled out in this study, which might also cause the change of charge and intermediate distribution

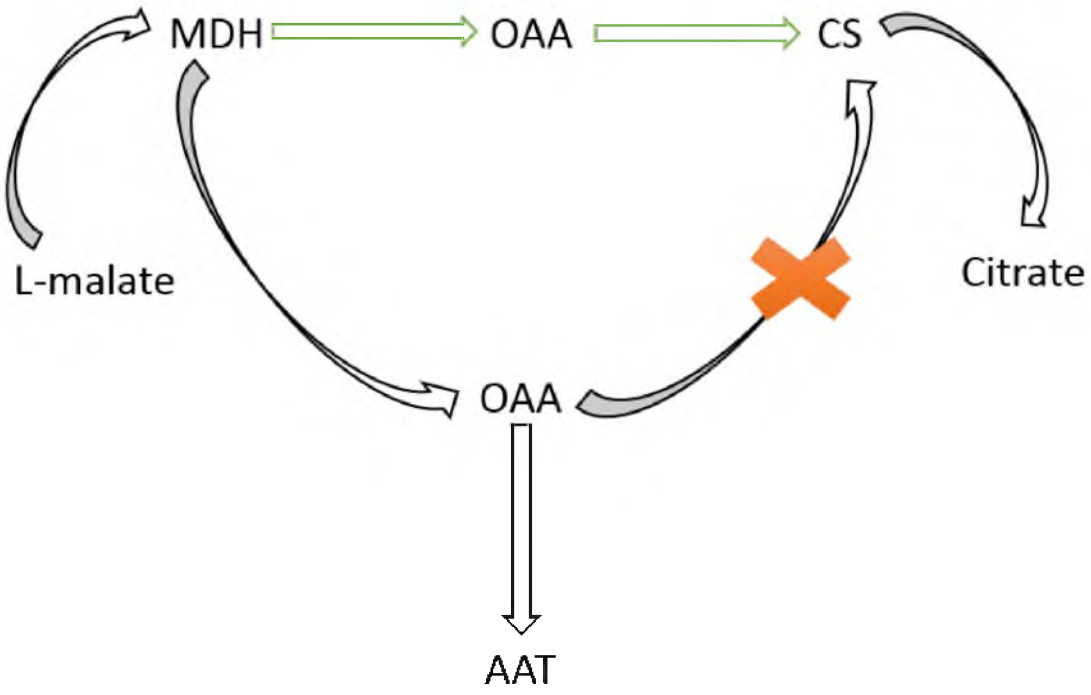

Figure 5.5 Illustration of the trapping of OAA by AAT.

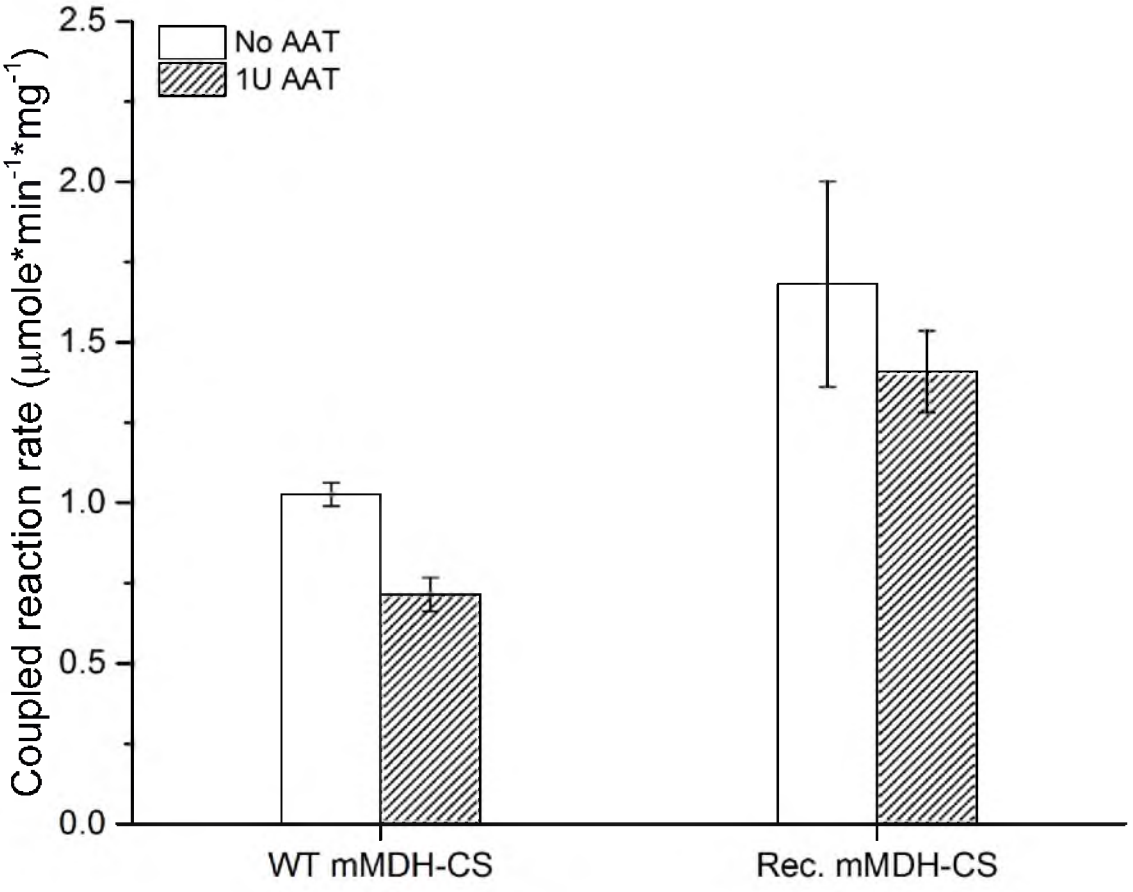

Figure 5.6 Coupled reaction rate of the immobilized mMDH-CS complex in the presence of AAT.

at metabolon surface.

Another experimental evidence of substrate channeling was achieved from the measurement of transient time of OAA in coupled reactions by stopped-flow method, and the absorbance change within the first five seconds upon mixing of substrates and enzymes is shown in Figure 5.7. As discussed in Chapter 1, the coupled activity is in direct proportion to the rate of the transient process between intermediate release and rebinding. One important factor in determining the rate of this transient process is the surface distance between two active sites, which increased by roughly 35% in the recombinant complex compared to the WT complex. Shortened traveling distance undoubtedly facilitated an efficient coupling of the two enzymes. If the process was similar to a surface random walk, the theoretical time needed for intermediate diffusion would reduce by 70% in the engineered complex. However, experimental results show that, τ of the WT complex was around 293 ± 35 ms, and after terminal modification, τ was drastically reduced by 90% to 30 ± 11 ms, implying that actual transport of OAA at complex surface was in a directed manner. It is also noteworthy that the relative orientation of active sites in the WT complex gives a higher chance of escaping of OAA into the bulk phase once released from mMDH.

As a negative control to the recombinant complex, disrupted channeling was achieved by replacing key residues contributing to rearrangement of electrostatic potentials. First we calculated the surface ESP after replacing the positively charged arginines on CS by neutral alanine. Simulation results (Figure 5.4) showed that the electrostatic connection of active sites was completely broken apart, and the surface ESP of the whole complex became more positive upon neutralization of the following CS arginines: 65, 67, 229, 324, 329 and 334. To experimentally demonstrate site-directed mutagenesis-induced channeling

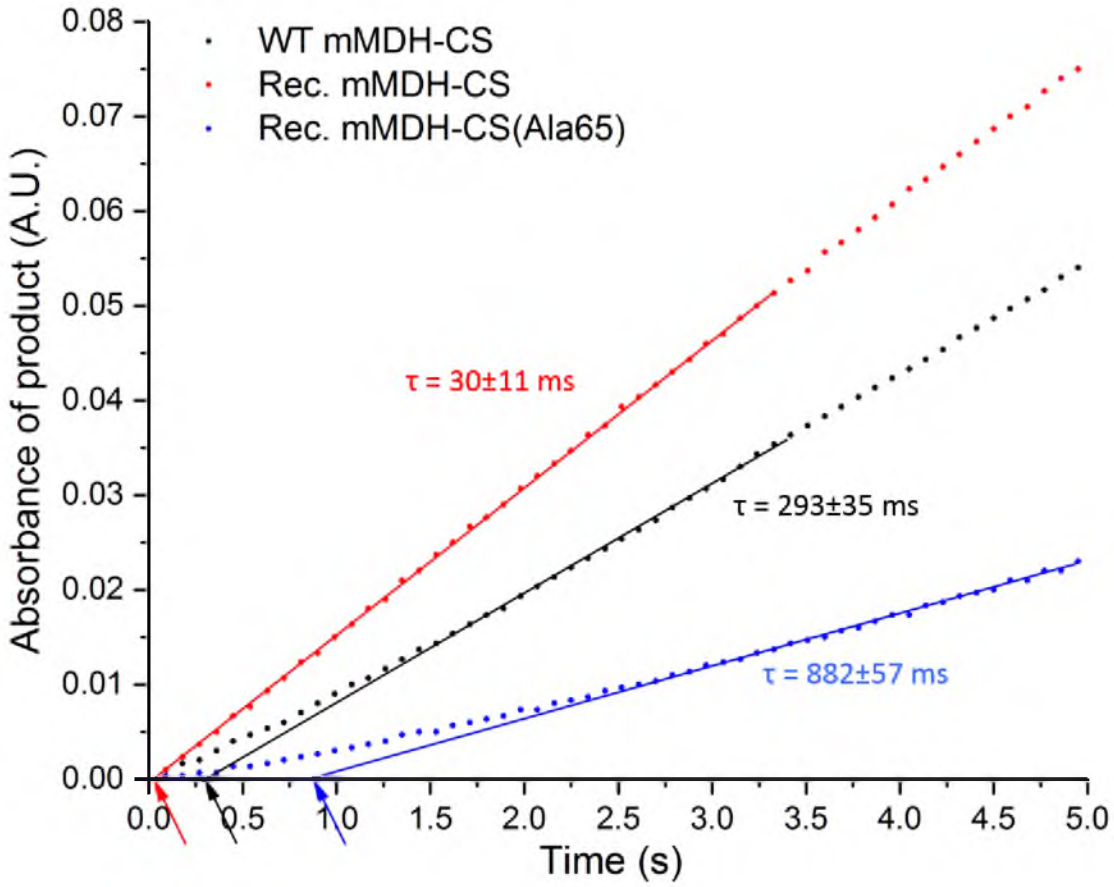

Figure 5.7 Change of product absorbance at 412 nm over time (dots) in coupled enzymatic reactions from L-malate to citrate. Straight solid lines were drawn at the steady state phase where maximum production rate was achieved, and extrapolated to the time axis. Intervals denoted by arrows were the transient time (τ) for each mMDH-CS complex.

disruption, we finally substituted CS Arg65 by Ala65. As shown in Figure 5.7, the coupled reaction rate drastically decreased with the transient time increased to nearly 1 s. The huge decline in catalytic performance of recombinant mMDH-CS complex indicated the crucial role of CS Arg65 in the metabolon formation, and also demonstrated that intermediate transport through channeling is enhanced by both the close proximity and a favorable conformation.

5.4 Conclusions

In this chapter, we have reconstituted an artificial TCA cycle metabolon in solution with recombinant mMDH and CS, and revealed that peptide-tagged N- and C-terminus in this specific situation can help orient protein-protein interactions in a more restricted manner. The resultant structure also shows its feasibility in oriented assembly. Simulation and kinetic study have demonstrated a significantly enhanced OAA channeling in the engineered metabolon compared to the WT mMDH-CS complex. In alanine scanning, CS Arg65 turns out to be a key residue in formation of metabolon and substrate channeling. Although the results we have obtained so far are preliminary, they at least point out a direction that we can follow in fabricating a metabolon mimic *in vitro*. This is the first attempt of making an extracellular TCA cycle metabolon based on naturally formed structure in combination of mass spectrometry, computer simulation and protein engineering. Ongoing efforts in the near future will be devoted to mapping of dominant residues in channeling construction by site-directed mutagenesis, which will also give us some deeper insight into the nature of the TCA cycle metabolon.

5.5 References

(1) Basle, E.; Joubert, N.; Pucheault, M. *Chem. Biol.* **2010**, *17*, 213.

(2) Chen, A. H.; Silver, P. A. *Trends. Cell. Biol.* **2012**, *22*, 662.

(3) Conrado, R. J.; Varner, J. D.; DeLisa, M. P. *Curr. Opin. Biotechnol.* **2008**, *19*, 492.

(4) Dueber, J. E.; Wu, G. C.; Malmirchegini, G. R.; Moon, T. S.; Petzold, C. J.; Ullal, A. V.; Prather, K. L. J.; Keasling, J. D. *Nat. Biotechnol.* **2009**, *27*, 753.

(5) Foley, T.; Burkart, M. D. *Curr. Opin. Chem. Biol.* **2007**, *11*, 12.

(6) Lai, Y. T.; King, N. P.; Yeates, T. O. *Trends. Cell. Biol.* **2012**, *22*, 653.

(7) Lin, Y. A.; Chalker, J. M.; Davis, B. G. *ChemBioChem* **2009**, *10*, 959.

(8) Muller, J.; Niemeyer, C. M. *Biochem. Biophys. Res. Commun.* **2008**, *377*, 62.

(9) Singleton, C.; Howard, T. P.; Smirnoff, N. *J. Exp. Bot.* **2014**, *65*, 1947.

(10) Terpe, K. *Appl. Microbiol. Biotechnol.* **2003**, *60*, 523.

(11) Hirakawa, H.; Nagamune, T. *ChemBioChem* **2010**, *11*, 1517.

(12) Ljungcrantz, P.; Buelow, L.; Mosbach, K. *FEBS Lett.* **1990**, *275*, 91.

(13) Vong, T.; Schoffelen, S.; van Dongen, S. F. M.; van Beek, T. A.; Zuilhof, H.; van Hest, J. C. M. *Chem. Sci.* **2011**, *2*, 1278.

(14) Schoffelen, S.; van Hest, J. C. M. *Soft Matter* **2012**, *8*, 1736.

(15) Lin, C.-W.; Ting, A. Y. *J. Am. Chem. Soc.* **2006**, *128*, 4542.

(16) Gilmore, J. M.; Scheck, R. A.; Esser-Kahn, A. P.; Joshi, N. S.; Francis, M. B. *Angew. Chem. Int. Ed. Engl.* **2006**, *45*, 5307.

(17) Nuir, T. W.; Sondhi, D.; Cole, P. A. *Proc. Natl. Acad. Sci. U. S. A.* **1998**, *95*, 6705.

(18) Xiao, J.; Tolbert, T. J. *Org. Lett.* **2009**, *11*, 4144.

(19) Bundy, B. C.; Swatrtz, J. *Bioconjugate Chem.* **2010**, *21*, 255.

(20) Hirakawa, H.; Kamiya, N.; Tanaka, T.; Nagamune, T. *Protein Eng., Des. Sel.* **2007**, *20*, 453.

(21) Hartwell, S. K.; Grudpan, K. *J. Anal. Methods. Chem.* **2012**, *2012*, 450716.

(22) Elcock, A. H.; McCammon, J. A. *Biochemistry* **1996**, *35*, 12652.

(23) Shatalin, K.; Lebreton, S.; Rault-Leonardon, M.; Velot, C.; Srere, P. A. *Biochemistry* **1999**, *38*, 881.

CHAPTER 6

SUMMARY AND FUTURE WORK

6.1 Summary

6.1.1 Mechanism for the TCA Cycle Metabolon Formation

The TCA cycle, consisting of eight enzymatic reactions, plays an essential part in complete oxidation of metabolites and generation of reducing power for ATP production in the cell.[1] Sequential enzymes in the TCA cycle are weakly associated into a supramolecular complex which is the TCA cycle metabolon.[2] Metabolons are known for featuring efficient intermediate transport or substrate channeling, and compartmentalizing metabolites into small, discrete pools, generating concentration gradients throughout the mitochondrial matrix.[3] However, the driving force for metabolon formation is still unclear, and the potential role played by these intermediate pools in metabolic organization has not been systematically explored.

A Y-shaped microfluidic channel was fabricated to examine transport of mMDH and CS in response to different substrate concentrations. It shows that each enzyme diffused against the concentration gradient of its specific substrate, and the apparent diffusivity was increased at higher substrate concentration. A following study on double enzymes demonstrates an enhanced co-diffusion against the concentration gradient of L-malate in the presence of coupled catalysis, indicating an OAA-induced "attraction" between mMDH and CS. Possible mechanisms were explored by removing cofactors or

adding inhibitors, and significant decline in either apparent diffusivity of a single enzyme or co-diffusion of coupled enzymes was observed. Results suggest that directed enzyme transport stimulated by a substrate concentration gradient is mainly driven by the conformational alteration upon ligand binding and can be accelerated by transition cycles during complete catalysis. This work finally reveals the driving force on dynamic association in the TCA cycle metabolon exerted by intermediate gradients between sequential enzymes.

6.1.2 Structure of the Natural TCA Cycle Metabolon

It is believed that high metabolic flux through the TCA cycle is facilitated by electrostatic channeling in the metabolon.[2,4] To prove its existence and advantage, fusion protein of mMDH/CS was studied by Srere *et al.* and they were able to simulate the electrostatic channeling formed between active sites in the fusion protein. Despite their work, there is little knowledge of protein-protein interactions between the TCA cycle enzymes inside mitochondria. Structural insights are needed for better understanding of natural occurrence in the metabolon.

In vivo chemical cross-linking was performed in intact mitochondria and fixed metabolons were analyzed by mass spectrometry for constituent enzymes and conjugated peptide fragments. Using a hybrid protein docking method, we finally resolved the structure of the mMDH-CS-ACO complex as a part of the giant metabolon. In this structure, mMDH, CS and ACO are associated asymmetrically, and their active sites are separated by short distances. Another noteworthy fact is that no terminus participate directly in binding, but they may play nontrivial roles in determining the final structure. Simulation of surface ESP reveals a charge rearrangement upon protein-protein interactions that leads

to the formation of a continuous surface band of positive potential, which may facilitate direct channeling of anionic intermediates between active sites.

6.1.3 Fabrication of the Artificial TCA Cycle Metabolon

Diverse efforts have been made to fabricate multi-enzyme assemblies featuring ordered organization and substrate channeling.[5] In general, there are two goals to pursue in making a metabolon mimic. One is the close proximity between enzymes, and the other is oriented assembly favoring substrate channeling. When pursuing these goals, one needs to address two questions. What tools may be used to keep enzymes together? What structure should the biomimic achieve? Finding out the answers will undoubtedly lead to a satisfying system.

One strategy investigated in this dissertation is polymeric co-immobilization. Model enzymes, mMDH, CS and ACO, were co-immobilized into LPEI, Nafion and chitosan polymers. Their interactions affected by polymer properties were characterized by FRET microscopy in terms of interprotein distances. On one hand, the result proves that multienzyme aggregation can be enhanced upon hydrophobic modifications, especially in polymers bearing micellar structures. As it suggests, trimethyloctadecylammonium modified Nafion is the best platform, in which co-immobilized enzymes have the shortest separation, highest single enzyme activity and most uniform localization. On the other hand, this study reveals that polymeric co-immobilization is not a rational technique in making real metabolons. Even though enzymes can be confined within short distances, their relative orientation is not manageable and self-aggregation may occur.

As another advanced alternative to polymeric co-immobilization, protein engineering was exploited, and N- and C-terminus of mMDH and CS were modified by

FLAG-tag and hexHis-tag, respectively. According to our knowledge of mMDH-CS interaction in the natural TCA cycle metabolon, we assumed that extended peptide tags would restrict the random binding in solution and only facilitate the orientation observed *in vivo*. Mass spectrometric and protein docking results validate our hypothesis, showing that interactions between peptide-tagged enzymes were directed to form a unique structure mimicking natural complex. This structure-based design proves it as a success in making a real metabolon *in vitro*, not only because the naturally occurring structure was retained, but also because of highly efficient intermediate transport, which is demonstrated by surface ESP simulation and kinetic studies.

6.2 Future Work

6.2.1 Future Directions

This research is ultimately aimed at reconstituting a robust enzyme cascade to mimic the function of the TCA cycle metabolon, which can be applied on the bioanode in a high-performance enzymatic BFC. The bioelectrocatalyst is able to catalyze complete oxidation of biofuels at fast turnover rate and high mass transport efficiency. Basically two directions can be followed: naturally occurring metabolons and artificial metabolon mimics. Proteins have evolved to acquire most favorable shape complementarity and recognition sites to allow their efficient incorporation in metabolism.[6,7] Therefore, direct utilization of the natural TCA cycle metabolon is a straightforward way of taking advantage of this in bioelectrocatalysis, provided that it is isolatable and robust. Artificial TCA cycle metabolon mimic can be fabricated with purified, engineered enzymes and is more compatible with different immobilization techniques. Further attempts should be made to

grouping the TCA cycle with other upstream enzymes or metabolic pathways and broadening the range of usable fuels for BFCs.

6.2.2 Isolatable Natural TCA Cycle Metabolon

As an amelioration of the *in vivo* chemical cross-linking discussed in Chapter 3, the TCA cycle metabolon is fixed by photoreactive nonnatural amino acids, which are incorporated into the protein primary sequence by cellular synthesis machinery. Commonly employed photoreactive amino acids are diazirine analogs of leucine/methionine and benzoylphenylalanine. After incorporation, exposing cell lines or intact mitochondria to ultraviolet light activates cross-linking of interacting enzymes in native environment. Since photoreactive non-natural amino acids behave just as their natural counterparts and can be incorporated at specific sites, extensive or random cross-linking causing metabolon distortion or deactivation is avoided.[8] Using this strategy, we can obtain robust TCA cycle metabolon without affecting its structure and activity through routine protein purification procedures.

6.2.3 Self-Assembled TCA Cycle Metabolon *In Vitro*

Study of enzyme dynamics in metabolon formation stimulated by intermediate generation provides a possibility of self-assembly in solution driven by catalysis. As previously reported by Sengupta *et al.*, immobilized enzymes can function as self-powered micropumps which drive directed transport of nanoparticles.[9] In fact, we can extend it to coupled enzymes and start sequential assembly simply by orderly adding substrates and following enzymes. To achieve this, an anchoring enzyme needs to be tethered to a surface or scaffold. For the TCA cycle metabolon, αKGDH complex turns out to be the best anchoring enzyme due to its large size. Affinity tags such as His-tags may be used to form

a protein monolayer on a modified electrode surface, or coordinate the enzyme into a three-dimensional polymer, protein or DNA scaffold. Alternatively, SDH can also anchor the rest of the TCA cycle enzymes to a lipid bilayer on the electrode, which actually simulates the occurrence in mitochondria.[10,11] Once catalysis is started in the presence of cross-linkers, intermediate-linked enzyme association will be fixed *in situ*.

6.2.4 Rational Engineering of Artificial Metabolon Mimics

Investigation of the natural TCA cycle metabolon is continued to resolve subsequent protein-protein interactions. Using structural information, we can design recombinant enzymes modified by functional groups or affinity tags at specific sites. These sites could be interfacial residues or residues located around the interface to enable directed association of free enzymes *in vitro*. However, deriving the three-dimensional structure of the whole metabolon needs extensive work and numerous mutation sites may be tried until the desired complex is attained. Another strategy is DNA scaffold-mediated assembly, by which recombinant TCA cycle enzymes are tethered to a linear DNA strand or a closed circle in an ordered manner. In this situation, orientation and stoichiometry are controllable, and intermediates are channeled from one site to the next.

6.2.5 Combining the TCA Cycle and Other Metabolic Pathways

As previously summarized in Figure 1.1, the TCA cycle serves as the endpoint of the complete oxidation of a variety of carbohydrates, fatty acids and amino acids.[12] In principle, coupling the TCA cycle to other metabolic pathways, such as glycolysis, β-oxidation of fatty acids/lipids and transamination, expands the potential fuel sources of high energy densities and improves power output of a BFC. For example, complete oxidation of one glucose molecule by glycolysis pathway-the TCA cycle gives 24 electrons.

Combining β–oxidation and the TCA cycle, complete oxidation of one steric acid molecule generates 52 electrons.[12] Amino acids give fewer electrons per molecule via transamination-the TCA cycle, but their abundance in proteins makes them promising energy sources for BFCs powered by degraded proteins. Further efforts shall be made in simplifying the catalytic pathways with synthetic oxidoreductases to improve the stability and catalyst loading on the electrode.

6.3 End Remarks

This dissertation work has elucidated the protein-protein interactions in the TCA cycle metabolon from mechanistic and structural perspectives, which helps the understanding of its nature as an efficient biocatalyst. Continuation of fundamental work will be in-depth exploration of enzyme cooperativity in metabolon formation and substrate channeling with the aid of protein engineering. Before moving on to a practical bioelectrocatalyst, metabolic regulation of the TCA cycle and its effectors *in vitro* should also be thoroughly characterized on the electrode. All these efforts ultimately leads to a promising future in the realm of portable micro-power sources with improved energy, current and power densities.

6.4 References

(1) Nunes-Nesi, A.; Araujo, W. L.; Obata, T.; Fernie, A. R. *Curr. Opin. Plant. Biol.* **2013**, *16*, 335.

(2) Robinson, J. B. J.; Inman, L.; Sumegi, B.; Srere, P. A. *J. Biol. Chem.* **1986**, *262*, 1786.

(3) Oaks, A.; Bidwell, R. G. S. *Annue. Rev. Plant. Physiol.* **1970**, *21*, 43.

(4) Elcock, A. H.; Huber, G.; McCammon, J. A. *Biochemistry* **1997**, *36*, 16049.

(5) Schoffelen, S.; van Hest, J. C. M. *Soft Matter* **2012**, *8*, 1736.

(6) Lai, Y. T.; King, N. P.; Yeates, T. O. *Trends. Cell. Biol.* **2012**, *22*, 653.

(7) Moreira, I. S.; Fernandes, P. A.; Ramos, M. J. *Proteins* **2007**, *68*, 803.

(8) Gómez-Nuñez, M.; Haro, K. J.; Dao, T.; Chau, D.; Won, A.; Escobar-Alvarez, S.; Zakhaleva, V.; Korontsvit, T.; Gin, A. Y.; Scheinberg, D. A. *PLoS One* **2008**, *3*, e3938.

(9) Sengupta, S.; Patra, D.; Ortiz-Rivera, I.; Agrawal, A.; Shklyaev, S.; Dey, K. K.; Cordova-Figueroa, U.; Mallouk, T. E.; Sen, A. *Nat. Chem.* **2014**, *6*, 415.

(10) D'Souza, S. F.; Srere, P. A. *J. Biol. Chem.* **1983**, *258*, 4706.

(11) Lyubarev, A. E.; Kurganov, B. I. *BioSystems* **1989**, *22*, 91.

(12) Bohinski, R. C. In *Modern Concepts in Biochemistry*; 5th ed.; Allyn and Bacon, Inc.: Newton, **1987**, p 540.